Trinity College Dublin
Coláiste na Tríonóide, Baile Átha Cliath
The University of Dublin

Doctoral Thesis

Towards Excited Radiative Transitions in Charmonium

Author:

Cian O'Hara

Supervisor:

Prof. Sinéad Ryan

A thesis submitted in fulfilment of the requirements

for the degree of Doctor of Philosophy

in the

School of Mathematics

March 2019

Declaration of Authorship

I declare that this thesis has not been submitted as an excercise for a degree at this or any other university and is entirely my own work.

I agree to deposit this thesis in the University's open acess institutional repository or allow the Library to do so on my behalf, subject to Irish Copyright Legislation and Trinity College Library conditions of use and acknowledgement.

Signed:

_____

Date:

_____

Abstract

Towards Excited Radiative Transitions in Charmonium

by Cian O'Hara

In this thesis lattice QCD is utilised to investigate the spectrum of charmonium and charmed mesons with the aim of working towards investigating radiative transitions between excited states in the charmonium spectrum. Results are presented from a dynamical $N_f = 2 + 1$ lattice QCD study of the excited spectrum of D_s and D mesons at a single lattice spacing with pion mass $M_\pi = 236$ MeV, which has been published in reference [1]. A robust determination of the highly excited spectrum of states, up to spin $J = 4$, was achieved with the use of distillation and the variational method. A comparison with earlier studies of the spectra on lattices with heavier light quarks was performed and the spectrum was found to have little dependence on the light quark mass. Results from an investigation into radiative transitions in the charmonium spectrum are also presented. A number of transitions are investigated and compared to experiment where possible. Three point correlation functions with a vector current insertion are calculated for a range of source and sink momenta allowing for the extraction of radiative form-factors for a wide range of Q^2 values. In particular, the transition $J/\psi \to \eta_c\gamma$ was investigated and found to be consistent with previous lattice results.

Acknowledgements

Firstly, I would like to thank Prof. Sinéad Ryan for all of the advice and supervision over the years during the course of this project, as well as her many helpful comments on this thesis, without which it would have never been completed.

I would also like to especially thank Christopher Thomas, David Wilson and Graham Moir, who all gave up so much of their time over the past four years whenever help was needed.

I would like to thank Mike Peardon and the rest of the Hadron Spectrum Collaboration, for providing the resources and computational infrastructure which was necessary for this work to be completed.

My officemates David Tims and Argia Rubeo, are owed many thanks for making these four years all that more enjoyable and for all the interesting discussions, academic or otherwise.

I would like to thank my girlfriend Manya and my mother Linda whose support helped me get to where I am today.

Finally I would like to thank the school of maths and the Irish Research Council for providing the funding which allowed this work to be performed.

Contents

List of Figures

List of Tables

Chapter 1

Introduction

From as far back as the ancient Greeks, mankind has sought to understand the building blocks of the material world in which we live. The idea that all matter is made up of indivisible units dates back to the 5th century BC. Since then our understanding of the nature of these *atoms*, from the Greek, atomon, meaning indivisible, has gone through many paradigm shifts. Due to the work of many experimental physicists, primarily Ernest Rutherford, John Cockcroft and Ernest Walton, in the early 20th century, the modern idea of the atom comprised of other more fundamental constituents, the electron, the proton and the neutron, emerged. These physicists pioneered the idea of accelerating particles to very high energies and smashing them together to see what they are made of.

Our current understanding of the fundamental constituents of matter dates to the 1960s when Murray Gell-Mann and George Zweig proposed independently the idea of the quark. Motivated by the ideas of SU(3) flavour symmetry, or the *Eightfold Way*, six quarks were envisioned and subsequently discovered over the course of 30 years, with the top quark being the last to be experimentally confirmed in 1995 [2, 3]). To this day, particle physicists around the world are building accelerator experiments reaching higher and higher energies than ever before in an attempt to further probe these fundamental matter particles.

The idea of a force between these building blocks dates to Issac Newton in the sixteenth century. In the "Philosophiae Naturalis Principia Mathematica" [4], he introduced the gravitational force which acts between any pair of massive objects.

In the 19th century James Clerk Maxwell united the ideas of elctricity and magnetism into the electromagnetic force. Then in the 20th century Albert Einstein revolutionised our understanding of gravity yet again with his theory of general relativity [5]. We now know of two other fundamental forces that govern the way subatomic particles interact. The strong nuclear force, which binds quarks together in nucleons and the weak nuclear force which is responsible for radioactive beta decay. In 1968 Sheldon Glashow, Abdus Salam and Steven Weinberg unified this weak force with the electromagnetic force into the electro-weak force [6–8].

The Standard Model of particle physics is the name given to the current theory describing the known elementary particles and the three aformentioned fundamental forces, the strong, weak and electromagnetic forces. Gravity, described by Einstein's general relativity, is as of yet, not included. It is proposed that all four forces may unite into a single force at extremely high energies but such a theory of everything is currently unknown. This would require a quantum theory of gravity, which is well beyond the scope of this thesis.

Mathematically the Standard Model is described as a quantum field theory (QFT). QFT was developed in the mid 20th century to unify quantum mechanics with special relativity. In it the various fermionic matter particles are described as quanta of an underlying operator valued quantum field. The forces between elementary particles are transfered by gauge bosons, the quanta of a gauge field. The most well known QFT is quantum electrodynamics, or QED. Established by physicists such as Paul Dirac and Richard Feynman, QED describes how electrically charged fermions, such as electrons and protons, interact. The force between these particles is mediated by the photon, the gauge boson of the theory. Photons are massless particles with no charge which means they do not interact with each other.

The QFT of interest for the strong interaction is quantum chromodynamics, or QCD. Based on a non-abelian gauge symmetry, with symmetry group SU(3), it describes how the six known quarks, named up, down, charm, strange, top and bottom, bind together under the stong interaction, via exchange of gluons, to form the hadronic matter observed in nature. The main difference between QCD and QED is that, unlike the photon, the gluons are charged under the strong interaction with *colour charge*. This is due to the non-abelian nature of the gauge group and means the gluons interact amongst themselves, which gives rise to two related concepts; confinement and asymptotic freedom.

The fact that these gluons interact among themselves, leads to what is known as colour confinement. This is the statement that no lone quarks or composite hadronic particles with non-zero colour charge are observed in experiment; ie. the quarks are bound inside composite particles. The simplest colour singlet arrangements of quarks consistent with this notion can be grouped into two classes, known as *baryons* and *mesons*, or collectively as *hadrons*. Baryons consist of three quarks (qqq) while mesons are made of a quark and an anti-quark ($q\bar{q}$). It also allows for more exotic states such as tetraquarks ($qq\bar{q}\bar{q}$) or pentaquarks ($qqq\bar{q}\bar{q}$), in which there is much interest [9]. These states of matter may potentially explain some currently unexplained resonances seen in experiment. However, for the purposes of this thesis we are primarily concerned with mesons containing a charm (c) quark.

The relative strength of the theories of QCD and QED can be encapsulated by their gauge couplings. In the case of QED, the fine structure constant, α, describes how strongly charged matter interacts with photons. At energy scales of the order of a hadron mass this takes a value of approximately 1/137. Due to this relatively small coupling, the theory of QED can be accurately described via a perturbative expansion to all orders. Perturbative calculations have had enormous success in calculating QED phenomena, such as the anomolous magnetic moment of the electron, to extremely high precision [10].

On the other hand, the coupling involved in the strong interaction, α_S, "runs" inversely to the energy scale. This asymptotic freedom means that at high energies, the strong force becomes weaker and quarks become essentially free. However at the energy scale of hadrons, α_S is of the order one. This strong coupling is where the strong force derives its name. The fact that this is of the order one means that hadronic interactions via the strong force cannot be accurately described using perturbation theory. Because of this another method to investigate the hadronic bound states of QCD is needed.

A typical QFT calculation is mainly concerned with calculating correlation functions of observables. Feynman showed that these can be expressed as a path integral. However it was found that naive calculations in QFT led to many catastrophic infinities arising. It was not until the ideas of regularisation and renormalisation appeared that these infinities were dealt with. Regulators such as dimensional regularisation or Pauli-Villars regularisation have had much success in the perturbatitive regime.

The work presented in this thesis utilises *lattice regularisation*, introduced by Wilson [11]. The use of a lattice as a regulator to investigate the strong force is the basis of the discipline of *Lattice QCD*. By discretising the theory of QCD on a spacetime lattice the path integral can be estimated explicitly using computational methods, avoiding the need to use perturbation theory. This will allow us to investigate the theory of the strong interaction at the hadronic scale where the coupling is large and elucidate the spectrum of hadrons allowed by the theory. Lattice QCD calculations are systematically improvable calculations from first principles allowing for accurate comparison to experiment with well defined sources of error.

1.1 Charm Physics

Any theory of sub-atomic particles is only valid provided it can hold up when compared to the empirically observed spectrum of states seen in experiment. With decades of data from accelerator experiments measured, by the 1970s a large "zoo" of experimentally observed particles were known. However it took until the introduction of the idea of quarks that any pattern amongst this zoo was obvious. Simple models, describing the various observed particles as strongly bound combinations of valence quarks had great success in explaining the observed spectrum of states. The discovery of the J/ψ meson, and hence the charm (c) quark, simultaneously by two different groups in 1974 was the final experimental evidence needed to allow the quark model of hadrons to become widely accepted, [12, 13].

The charm quark is of particular interest as it is substantially heavier than the lighter up, down and strange quarks, allowing it to be described by simple non-relativistic potential models but also light enough that it lives long enough to form observable bound states. In this way it is in a rather unique position and its spectrum can be used to compare experiment to theory.

Since 1974, there have been as many as eighteen experimentally confirmed states in the charmonium spectrum. Charmonium is a meson containing a c quark and its anti particle ($\bar{c}$), with the aforementioned J/ψ being the first observed meson in the spectrum. There have also been many observed states in the spectrum of charmed-strange mesons ($c\bar{s}$) known as the D_s meson and the charmed-light ($c\bar{l}$) mesons known as the D meson.

L	S	J	J^{PC}
0	0	0	0^{-+}
	1	1	1^{--}
1	0	1	1^{+-}
	1	2,1,0	$2^{++}, 1^{++}, 0^{++}$
2	0	2	2^{-+}
	1	3,2,1	$3^{--}, 2^{--}, 1^{--}$
3	0	3	3^{+-}
	1	4,3,2	$4^{++}, 3^{++}, 2^{++}$

L	S	J	J^{P}
0	0	0	0^{-}
	1	1	1^{-}
1	0	1	1^{+}
	1	2,1,0	$2^{+}, 1^{+}, 0^{+}$
2	0	2	2^{-}
	1	3,2,1	$3^{-}, 2^{-}, 1^{-}$
3	0	3	3^{+}
	1	4,3,2	$4^{+}, 3^{+}, 2^{+}$

TABLE 1.1: Possible J^{PC} and J^{P} values allowed from simple quark models.

For a long time, a simple model of valence quarks bound together in hadrons was enough to explain the observed spectra. Simply, a meson is a hadronic bound state composed of a quark and anti-quark pair. As quarks are spin $\frac{1}{2}$ fermions, the allowed spin S for a meson in its ground state is either 0, when the quarks spins are anti-parallel or 1 when the spins are aligned.

When the the spins are aligned the meson is said to be in a spin triplet state as there are three S_z projections 1,0,-1. If the spins are opposite then there is only one S_z projection, namely $S_z = 0$ and the meson is said to be in a spin singlet state.

Along with this spin angular momentum, the meson can have an orbital angular momentum L. The total spin, J, of the meson is then given as

$$J = L + S \quad \text{with} \quad |L - S| \leq J \leq |L + S|. \tag{1.1.1}$$

In this way the mesons can be classified using the familiar spectroscopic notation of the Hydrogen atom, $n^{2S+1}L_J$. Along with spin, each meson is also labelled according to how it transforms under the operations of charge conjugation C and parity transformations P. The charge and parity quantum numbers are related to the spin of a meson via the following simple formulae.

$$P = (-1)^{L+1}, \qquad C = (-1)^{L+S}. \tag{1.1.2}$$

Using these charge and parity quantum numbers the mesons and their excited states can be classified according to their J^{PC}. For mesons made of up of a quark

and anti-quark of different flavour, such as the D_s and D mesons, C is not a good quantum number and so the states can be labelled by just their J^P numbers.

Using these formulae the allowed states in the spectrum of a meson can naively be predicted as shown in Table 1.1. It is noteworthy that in this model some J^{PC} combinations, such as 0^{+-} and 1^{-+} do not appear. These exotic quantum numbers give rise to what are termed *exotic states*, and the search for such states is ongoing.

Over the past decade many states that do not fit nicely into these naive classifications have been observed in experiment [14]. Specifically in the case of charmonium, the observation of so-called X, Y, Z states highlight the need for a more complete theoretical understanding of the hadronic spectrum, be they hybrid mesons, tetra-quarks or some other hitherto unknown form of matter, [15, 16]. Similarly, in the charm-light sector, states such as the $D_{s0}(2317)^{\pm}$ and $D_{s1}(2460)^{\pm}$ have been found to have much narrower widths than expected [17].

In order for QCD to be an accurate description of nature, it must account for these unexplained states seen in experiment. One way to test this is to perform a first principles lattice QCD calculation of the theory and attempt to reproduce the spectrum observed in experiment.

1.2 Lattice Basics

According to Feynman, a field theory with field Φ and relativistic action $S[\Phi]$ can be quantised by writing down a path integral. From this one can calculate expectation values of the theory's observables $\mathcal{O}(\Phi)$ from n-point correlation functions as

$$\langle 0|\mathcal{O}_1(\Phi), \mathcal{O}_2(\Phi)...\mathcal{O}_n(\Phi)|0\rangle = \frac{1}{Z}\int \mathcal{D}\Phi e^{-iS[\Phi]}\mathcal{O}_1(\Phi), \mathcal{O}_2(\Phi)...\mathcal{O}_n(\Phi). \tag{1.2.1}$$

Z is known as the partition function and is given by

$$Z = \int \mathcal{D}\Phi e^{-iS[\Phi]}. \tag{1.2.2}$$

These expressions involve integrals over all possible field configurations Φ weighted by the Boltzmann factor $e^{-iS[\Phi]}$. To make such calculations possible and mathematically well defined one must introduce a regulator, to avoid infrared and ultraviolet divergences. There are many possibilities such as dimensional regularisation or Pauli-Villars regularisation, however this work is performed using lattice regularisation [11].

To do this, spacetime is modelled no longer as a continuum but a four dimensional finite sized discrete box of length L, made of points with a finite spacing, a, between them. Matter fields can now only live on the lattice points and the gauge fields live on the links between them. In this way a natural ultraviolet cutoff, $1/a$, has been introduced which regulates any momentum integrals. The finite extent of the lattice also acts as an infrared cutoff. Spacetime integrals over the field configurations now become sums over a finite set of lattice field configurations.

This allows Eqn. 1.2.1 to be recast as a lattice path integral which is a sum over operators acting on this finite set of lattice field configurations. As it appears in Eqn. 1.2.1, the exponential weighting factor is highly oscillatory. However a Wick rotation may be performed on the Minkowski time coordinate, such that $t \to -i\tau$. This allows Eqn. 1.2.2 to be rewritten as a Euclidean path integral, where S_E is now the discretised Euclidean action.

$$Z = \int \mathcal{D}\Phi e^{-S_E[\Phi]}. \tag{1.2.3}$$

The lattice regularisation naturally lends itself to computational methods. Monte Carlo importance sampling techniques can be used in the evaluation of any observables computationally. One can generate a large ensemble of lattice configurations in a Markov chain weighted by e^{-S_E} which minimise the action and hence contribute meaningfully to the path integral. An approximate expectation value of an observable can then be computed by averaging its value over these configurations.

This is a systematically improvable procedure and is the only prudent way to investigate strongly interacting theories. In the case of the strong interaction, where the coupling is of the order one, perturbative methods fail and one must use these Monte Carlo methods on a computer to evaulate these integrals explicitly. This is important in investigating the question of confinement as it can only be

explored using non-perturbative methods. It also allows the use of many methods from the study of statistical mechanics which can be used to help understand QCD.

1.3 Sources of Error

Introducing a lattice as a regulator and using Monte Carlo estimation techniques to evaluate path integrals will necessarily result in the introduction of statistical and various systematic errors in any lattice calculation. Any result must then have these sources of error under control so as to be able to make contact with experimental results. These various errors can classified as follows:

- Statistical errors - Approximating the path integral shown in Eqn. 1.2.1 as a sum to be estimated via Monte Carlo integration introduces statistical errors. These can be reduced by increasing the number of field configurations, N, used and fall off as $\frac{1}{\sqrt{N}}$. Errors quoted in this work will be purely statistical. For more information see Appendix A.

- Discretisation errors - These arise due to discretising the action of the theory on the lattice with finite spacing a. These errors appear in powers of a and can be formally reduced via a procedure known as improvement which will be discussed in Chapter 2. Calculations at smaller a will also reduce these errors but increase the time needed to simulate on a computer.

- Finite volume errors - These arise due to the finite extent L of the lattice. However these errors are proportional to e^{-ML}, where M is the lattice pion mass, and so can be mitigated by taking L to be large compared to the mass scale of the system under investigation. Simulating at more than one value of L allows these errors to be quantified.

- Errors due to scale setting - Lattice results will be expressed in units of the lattice spacing, a, which is unknown. In order to convert the results to physical units and compare to experiment the scale must be set. This may be done by measuring the mass of one state, such as the Ω baryon, and taking the ratio of its lattice value to its physical value. This introduces a systematic uncertainty, which may vary depending on the chosen state.

- Chiral extrapolation - Due to computational constraints, lattice simulations are often performed using un-physically heavy light quark masses. Simulating at multiple quark masses allows for an extrapolation to the physical point, which introduces its own model dependent error. However more recently calculations at physical quark masses have started to be performed [18, 19].

- Heavy Quarks - The charm quark was traditionally difficult to simulate on the lattice due to its large mass m_c compared to the lighter quarks. While it is light enough to be treated relativistically, finite volume and discretisation effects can become large. Anisotropic lattices allow for a solution where only the temporal spacing is reduced such that $m_c a_t \ll 1$, without greatly increasing the computational cost of simulating at small a, however errors involving a_s will still exist.

Lattice calculations of hadronic spectra are now the definitive way of investigating the theory of QCD in the non-perturbative regime. The accurate description of the energies of low lying states in the QCD spectrum has been an important benchmark of lattice studies for many years. For a recent review see [20, 21]. Recently newer technologies and increased computational power have allowed for studies of higher-lying states and resonances. These studies allow for much more precise determinations than ever before, as well as providing valuable insight into previously unstudied regions such as hybrid or exotic states, [22–25].

In this thesis some topical questions in the charmonium spectrum will be investigated utilising the most up to date technologies and lattices available. Starting with a discussion of QCD in Chapter 2, the technology needed to perform a spectroscopic calculation on the lattice will be introduced in Chapter 3. This will be followed by an investigation of the D_s and D meson spectrum in Chapter 4, which was reported on in reference [1]. Chapter 5 will extend the previously introduced spectroscopic methods to investigate radiative transitions. Finally in Chapter 6, results for radiative transitions between states in the charmonium spectrum will be shown, making comparison with experiment where possible.

Chapter 2

Lattice Quantum Chromodynamics

The main aim of this study is to use the techniques of lattice field theory to investigate the spectrum of charmonium on the lattice. In order to do this one must look to discretising quantum chromodynamics (QCD), the theory of the the strong interaction. This is done by restricting the quark degrees of freedom to a discrete set of regular points constituting a spacetime lattice while assigning the gluonic gauge degrees of freedom to the links in between points. After a brief recap of continuum QCD it will be shown how this discretisation is possible and how some naive attempts will ultimately lead to failure. There will then be a brief discussion on the idea of improvement, which increases the accuracy of any predictions by reducing the effect of discretisation on the calculation of observables.

2.1 The Action of QCD

As was discussed in Chapter 1, nature contains six matter particles called quarks. These quarks come together under the strong interaction to form all of the hadrons that are observed in experiment. These quarks are described as spinor fields $\psi_f^{i\alpha}(x)$, where α is a Dirac index and f is a "flavour" index running from 1 to 6, for each flavour or type of quark. i is a colour index running from 1 to 3, as the quarks are charged under the fundamental representation of $SU(3)$. Under a local gauge transformation the fields transform as

$$\psi_i(x) \to \Lambda_{ij}(x)\psi_j(x), \qquad \bar{\psi}_i(x) \to \bar{\psi}_j(x)\Lambda^\dagger_{ij}, \tag{2.1.1}$$

where $\Lambda(x) \in SU(3)$. In the usual way one can introduce a gauge field G_μ and bare coupling constant g_0, and define a covariant derivative $D_\mu = \partial_\mu - ig_0 G_\mu$ that transforms as

$$D_\mu \longrightarrow \Lambda(x) D_\mu \Lambda^\dagger(x), \qquad G_\mu \longrightarrow \Lambda(x) G_\mu \Lambda^\dagger(x) + \frac{i}{g_0}\Lambda(x)\partial_\mu \Lambda^\dagger(x), \tag{2.1.2}$$

to ensure gauge covariance of the lagrangian. G_μ is a lie algebra valued matrix gauge field and can be written as a sum over the generators T_i of $SU(3)$ as $G_\mu(x) = \sum_{i=1}^{8} G^i_\mu(x) T_i$. In general $T_i = \frac{1}{2}\lambda_i$ where λ_i are the standard Gell-Mann matrices. This shows that the gauge field transforms in the adjoint representation of $SU(3)$ and that there are 8 individual gluon fields $G^i_\mu(x)$. A field strength tensor $G_{\mu\nu}$ which transforms in the same way as D_μ can be defined from the commutator of two derivatives such that

$$G_{\mu\nu} \equiv \frac{i}{g_0}[D_\mu, D_\nu] = \partial_\mu G_\nu - \partial_\nu G_\mu - ig_0[G_\mu, G_\nu]. \tag{2.1.3}$$

The commutator $[G_\mu, G_\nu]$ here is non zero due to the non-abelian nature of the gauge group. This allows a gauge invariant term for the lagrangian $\mathrm{tr}[G_{\mu\nu}G^{\mu\nu}]$ to be written down. The field strength tensor can be expanded as a sum over the individual gluon fields as

$$G_{\mu\nu} = \sum_{i=1}^{8} G^i_{\mu\nu} T_i, \quad \text{where} \quad G^i_{\mu\nu} = \partial_\mu G^i_\nu - \partial_\nu G^i_\mu + g_0 f_{ijk} G^j_\mu G^k_\nu. \tag{2.1.4}$$

Here the relation from $SU(3)$ that $[T_i, T_j] = i f_{ijk} T_k$ has been used. The f_{ijk} are known as the structure constants of the group. Using one final $SU(3)$ relation, $\mathrm{tr}[T_i, T_j] = \frac{1}{2}\delta_{ij}$, the full gauge covariant QCD action, suppressing most indices, can be written down as

$$\mathcal{S}_{QCD} = \int d^4x \left(\bar{\psi}[i\gamma_\mu D^\mu - m]\psi - \frac{1}{4}\sum_{i=1}^{8} \mathrm{tr}[G^i_{\mu\nu} G^{i\mu\nu}] \right), \tag{2.1.5}$$

where γ_u are the standard Dirac gamma matrices. This looks to be quite similar to the more well known lagrangian of QED. There is however one main difference, the last term in Eqn. 2.1.4. This term encapsulates the self-interactions of the gluon field and leads to the major differences between QED and QCD, namely confinement.

2.2 Discretisation of the Action

As discussed in Chapter 1, to compute any observables one must regularise the theory on a lattice. To this end, a hypercubic Euclidean lattice of size $L_x \times L_y \times L_z \times L_t$ is defined. Here the spatial extent $L_x = L_y = L_z = n_s a_s$ and the temporal $L_t = n_t a_t$ where a_s, a_t, n_s, and n_t are the spatial and temporal lattice spacings and number of points respectively. In this thesis all work is done on *anisotropic* lattices, where $a_t \neq a_s$, which will be discussed in more detail later.

The quark fields of the theory are assigned to the points of the lattice such that $\psi(x) \to \psi(n)$, where $n = (n_x, n_y, n_z, n_t)$ specifies a point of the lattice. The first term in Eqn. 2.1.5 involves a derivative and so necessarily links quark fields at different points on the lattice. Focusing on the simple partial derivative in D_μ, it can be approximated on the lattice symmetrically as

$$\partial_\mu \psi(x) \to \frac{1}{2a}(\psi(n+\hat{\mu}) - \psi(n-\hat{\mu})). \tag{2.2.1}$$

This will result in terms of the form $\bar{\psi}(n)\psi(n+\hat{\mu})$ in the discretised action, which are now no longer gauge invariant. This necessitates the introduction of a field $U_\mu(n)$. The "link variable" $U_\mu(n)$ is assigned to the link between the lattice site n and $n+\hat{\mu}$. The link variable going in the opposite direction, ie. from $n+\hat{\mu}$ to n, is given by $U^\dagger_\mu(n) = U_{-\mu}(n+\hat{\mu})$ as shown in Figure 2.1. The term $\bar{\psi}(n)U_\mu(n)\psi(n+\hat{\mu})$ is now gauge invariant provided $U_\mu(n)$ transforms as $U_\mu(n) \longrightarrow \Lambda(n)U_\mu(n)\Lambda^\dagger(n+\hat{\mu})$.

FIGURE 2.1: The link variables $U_\mu(n)$ and $U^\dagger_\mu(n)$.

A transformation such as this can be achieved by a lattice version of a gauge transporter. For a gauge field G_μ in the continuum, a gauge transporter from the point x to y, along the path C, is given by

$$U_C(x,y) = \mathrm{P}\ \exp\left(i\int_C dx_\mu G^\mu(x)\right), \tag{2.2.2}$$

where the P stands for path ordering of the exponential. It relates the points x and y in a similar way to how parallel transport relates points on a manifold, and transforms in the necessary way under a gauge transformation. To $\mathcal{O}(a)$ one can approximate the integral by the value of G_μ at the point n times the spacing a such that on the lattice,

$$U_\mu(n) = \exp(iaG_\mu(n)). \tag{2.2.3}$$

This shows that $U_\mu(n)$ are gauge group valued, as $G_\mu(n)$ lives in the lie algebra of $SU(3)$. Any path between two points on the lattice made by multiplication of individual link variables will transform in the same way as a single link, as all of the gauge rotations will cancel except at the end points. Due to the fact that the group is non-abelian, the order of the product of link variables is important.

Non-trivial paths that start and end on the same site of the lattice are of greater interest as they can be made into gauge invariant objects by taking a trace. The simplest such path, a square of side a, is known as a plaquette and is denoted by $U_{\mu\nu}(n)$. It is formed from the product of the four link variables around the square in the order they are encountered, shown in Figure 2.2,

$$U_{\mu\nu}(n) = U_\mu(n)U_\nu(n+\hat{\mu})U^\dagger_\mu(n+\hat{\nu})U_\nu(n)^\dagger. \tag{2.2.4}$$

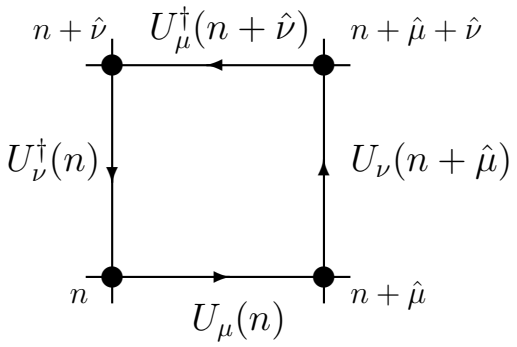

FIGURE 2.2: An elementary plaquette, $U_{\mu\nu}(n)$.

Using plaquettes, a gauge invariant action known as Wilson's action can be written down. It is a sum over all the individual plaquettes on the lattice and is given as

$$S_G[U] = \frac{2}{g_0^2} \sum_n \sum_{\mu<\nu} \text{Re tr}[1 - U_{\mu\nu}(n)]. \tag{2.2.5}$$

Expanding Eqn. 2.2.3 and using the Baker-Campbell-Hausdorff formula, it can be seen that $U_{\mu\nu}(n) = \exp(ia^2 G_{\mu\nu}(n) + O(a^3))$. $G_{\mu\nu}(n)$ here is the obvious discretised version of the continuum field strength tensor. The Wilson action then becomes

$$\frac{a^4}{2g_0^2} \sum_n \sum_{\mu<\nu} \text{tr}[G_{\mu\nu}(n)^2] + O(a^2). \tag{2.2.6}$$

So it is clear that in the continuum limit Eqn. 2.2.5 will reduce to the Yang Mills part of Eqn. 2.1.5 and so provides an appropriate lattice discretisation correct to $\mathcal{O}(a^2)$.

Returning now to the fermion derivative term one can write down a gauge invariant action, known as the naive fermion action

$$S_F[U, \psi.\bar{\psi}] = a^4 \sum_{n\in\Lambda} \bar{\psi}(n) \left(\sum_{\mu=1}^{4} \gamma_\mu \frac{U_\mu(n)\psi(n+\mu) - U_{-\mu}(n)\psi(n-\mu)}{2a} - m\psi(n) \right), \tag{2.2.7}$$

where γ_μ are the discretised versions of the Dirac gamma matrices. This term has errors in $\mathcal{O}(a)$. The total discretised action is now given by $S_F + S_G$. The

formula for the evaluation of observables which are functions of the lattice fields from Chapter 1 then becomes

$$\langle 0|\mathcal{O}(U,\psi,\bar{\psi})|0\rangle = \frac{1}{Z}\int \mathcal{D}[U,\psi,\bar{\psi}]e^{-S_F[U.\psi,\bar{\psi}]-S_G[U]}\mathcal{O}(U,\psi,\bar{\psi}). \tag{2.2.8}$$

with

$$Z = \int \mathcal{D}[U,\psi,\bar{\psi}]e^{-S_F[U.\psi,\bar{\psi}]-S_G[U]}. \tag{2.2.9}$$

It is important to note here that fermions are described by Grassmann numbers. Grassmann numbers anti-commute, ie. $\eta_i\eta_j = -\eta_j\eta_i$ and follow various different relations as explained in reference [26]. One important relation, which will be of use in the path integral is, for matrix M and Grassmann valued fields $\bar{\eta}, \eta$,

$$\int \mathcal{D}[\eta]\mathcal{D}[\bar{\eta}]e^{\bar{\eta}_i M_{ij}\eta_j} = \det(M). \tag{2.2.10}$$

This relation can be used to simplify the path integral. Eqn. 2.2.7 can be rewritten as

$$S_F[U,\psi,\bar{\psi}] = a^4 \sum_{n,m\in\Lambda}\sum_{a,b,\alpha,\beta} \bar{\psi}(n)^{\alpha}_{a}\, D(n|m)^{\alpha\beta}_{ab}\, \psi(m)^{\beta}_{b}, \tag{2.2.11}$$

where D is known as the Dirac fermion matrix,

$$D(n|m)^{\alpha\beta}_{ab} = \sum_{\mu=1}^{4}(\gamma_\mu)_{\alpha\beta}\frac{U_\mu(n)_{ab}\delta_{n+\hat{\mu},m} - U_{-\mu}(n)_{ab}\delta_{n-\hat{\mu}.m}}{2a} + m\delta_{\alpha\beta}\delta_{ab}\delta_{n,m}. \tag{2.2.12}$$

By doing the integral over the fermionic fields analytically, the partition function 2.2.9 becomes

$$Z = \int \mathcal{D}[U]e^{-S_G[U]}\det(D[U]). \tag{2.2.13}$$

Now the exponential weight needed to choose gauge configurations in the importance sampling is given by $e^{-S_G[U]}\det(D[U])$. This is a very useful result as it reduces the need to deal with anti-commuting numbers on the computer to simply calculating a determinant. That said, the fermion determinant is notoriously expensive to compute and for many years it was taken to be 1, in what was known as the quenched approximation. As the gauge configurations are basically snapshots of the vacuum, this amounts to taking the mass of any sea-quarks to infinity effectivly "quenching" or freezing them, which removes the effect of vacuum quark loops. However over the last decade or two, improvements in computational power and algorithms have made configurations with dynamical sea-quarks more feasible [27]. The work in this thesis uses $N_f = 2 + 1$ lattices containing two light quarks of equal mass and one heavier strange quark in the sea [28].

Gauge configurations are generated in a Markov chain Monte Carlo process, with a probability distribution proportional to the above Boltzmann factor. To start, a simple configuration, U_1 is chosen. For example all lattice links may take the value of unity, known as a cold start, or random link values, known as a hot start. Successive configurations are generated iteratively by making a small change or update to one or a small group of the lattice links in what is knwon as a Markov chain.

$$U_1 \rightarrow U_2 \rightarrow U_3 \rightarrow ...U_N \tag{2.2.14}$$

The simplest way of generating the Markov chain is by using the Metropolis algorithm [29]. For each successive update step a new trial configuration is proposed. This is then tested and accepted with a certain probability proportional to the Boltzmann factor. This ensures the ensemble of configurations tend towards those with lower energy and hence greater importance in the evaluation of path integrals. The two necessary conditions for an appropriate Markov process where all possible configurations are available to be sampled, ergodicity and detailed balance, can be ensured with the correct choice of acceptance probability. Once the trial configuration has been accepted or refused, the process restarts again from the most recently updated configuration. More advanced algorithms, such as the Rational Hybrid Monte Carlo (RHMC) algorithm [30, 31] used in the generation of the configurations used in this thesis, provide a better choice of trial configurations.

Depending on the starting choice, the first few configurations may be quite far from minimising the action. Usually a number of update steps are performed initially, to allow for *thermalisation*, so that the configurations obey the desired probability distribution. Once this has been achieved every n^{th} configuration is kept to account for auto-correlations between successive steps in the Markov chain. Once the ensemble of N configurations has been generated and accepted, an observable O on the lattice can be estimated by evaluating it on the individual configurations U_i and taking an average.

$$\langle O \rangle = \frac{1}{N} \sum_{i=1}^{N} O[U_i]. \tag{2.2.15}$$

Due to the importance sampling this sum will approximate the path integral as N gets large and the associated statistical error will fall as $\frac{1}{\sqrt{N}}$, provided the configurations are uncorrelated.

Ultimately these configurations generated using the discretised lattice action will be used to calculate fermionic observables. One can take advantage of a theorem known as Wick's theorem to rewrite correlation functions of fermionic operators as products of propagators [32] such that,

$$\langle \eta_{i_1} \bar{\eta}_{j_1} ... \eta_{i_n} \bar{\eta}_{j_n} \rangle_F = (-1)^n \sum_{P(1,2,...,n)} \text{sign}(P) (D^{-1})_{i_1 j_{P_1}} (D^{-1})_{i_2 j_{P_2}} .... (D^{-1})_{i_n j_{P_n}}. \tag{2.2.16}$$

This has reduced the problem to computing products of *quark propagators* which are given by the inverse of the Dirac matrix. These propagtors must be evaluated on each of the gauge configurations chosen with the correct weight as discussed above. The computation of D^{-1} is another highly non-trivial problem, and so the complete inverse is never fully computed.

There is one final subtlety with the lattice quark action that must be addressed. Eqn. 2.2.7 actually describes sixteen fermions due to what is known as the fermion doubling problem. These *doubler* fermions become apparent when looking at the inverse of the Dirac matrix in momentum space. Due to the lattice discretisation and hence discretised momenta, the inverse $D^{-1}(p)$ has multiple unphysical poles

at the edges of the Brillouin zone. Wilson proposed the addition of a term (shown below) in the Dirac operator proportional to a, such that in the continuum limit it disappears.

$$-a\sum_{\mu=1}^{4}\frac{U_{\mu}(n)_{ab}\delta_{n+\hat{\mu},m}-2\delta_{ab}\delta_{n,m}+U_{-\mu}(n)_{ab}\delta_{n-\hat{\mu},m}}{2a^{2}} \tag{2.2.17}$$

This new addition leads to a mass term for these unwanted doublers proportional to $\frac{1}{a}$, effectively removing the poles. Unfortunately this explicitly breaks chiral symmetry, even in the $m = 0$ limit. This is a consequence of the Nielsen-Ninomiya no-go theorem [33], which states it is impossible to have a lattice gauge theory that is simultaneously local and respects chiral symmetry while containing no doubler fermions.

The inclusion of the Wilson term results in what is called the Wilson fermion action. There are other discretisation procedures possible to describe quarks on the lattice. Staggered, or Kogut-Susskind [34], fermions reduce the sixteen doublers down to four by distributing them across the lattice via a field transformation. Twisted mass fermions improve on Wilson fermions by adding a twisted mass term which stops the occurance of *exceptional configurations*, where the eigenvalues of the Dirac matrix become small leading to elongated inversion times, however they break parity and flavour symmetries [35]. This thesis, however, is based on work done with Wilson fermions.

2.3 Improvements

As has been stated before, naive discretisations of the QCD action lead to errors proportional to powers of the lattice spacing, which should disappear when taking the continuum limit. Unfortunately, it is not possible to perform lattice calculations at $a = 0$. However there are systematic ways of removing these errors by exploiting the fact that any discretisation is not unique. It is possible to write down a discretised action that has the same continuum limit as before, hence describing the same physics, but that has reduced errors. The process of removing these errors systematically is known as Symanzik improvement.

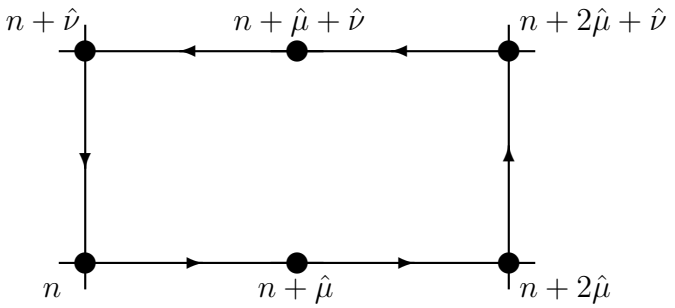

FIGURE 2.3: The dimension six 2×1 rectangular operator.

As described in reference [36], Symanzik showed that in general, it is possible to create an improved action which approaches the continuum limit more quickly by adding higher order terms to the original lattice lagrangain $\mathcal{L}_0$. These new terms must also respect the original symmetries of the lagrangian.

$$S_{imp} = \int d^4x(\mathcal{L}_0 + a\mathcal{L}_1 + a^2\mathcal{L}_2 + ...). \tag{2.3.1}$$

Eqn. 2.2.6 shows that the Wilson gauge action, which is made up of the dimension four plaquette operator, has errors in $\mathcal{O}(a^2)$. To remove these some higher order gauge invariant terms made up of the link variables U_μ must be added. There are no closed paths of gauge links possible containing an odd number of link variables. So $L_1 = 0$. At dimension six, there are three unique possible paths one can make out of gauge links,

$$\mathcal{L}_2 = c_1\mathcal{L}_2^{(1)} + c_2\mathcal{L}_2^{(2)} + c_3\mathcal{L}_2^{(3)}. \tag{2.3.2}$$

The improvement coefficients c_n must be tuned so as to accurately remove the $\mathcal{O}(a^2)$ errors. It is shown in reference [37], that the rectangular Wilson loop of 2×1 links, shown in Figure 2.3, is the only necessary term to improve to $\mathcal{O}(a^2)$ such that one can take $c_1 = -\frac{1}{12}$ and $c_2 = c_3 = 0$.

Once the improvement term has been added there is one final improvement that must be made before arriving at the complete gauge action, a rescaling of the link variables in what is known as *tadpole improvement* [38],

$$U_\mu(x) \to \frac{U_\mu}{u_0}, \quad \text{where} \quad u_0 = \langle \frac{1}{N} \mathrm{ReTr} U_{\mu\nu} \rangle^{\frac{1}{4}}. \tag{2.3.3}$$

This rescaling removes the effect of vacuum tadpole diagrams, induced from the definition of U_μ. If the exponential in Eqn. 2.2.3 is expanded, terms of a^2 and higher will have powers of the gauge field G_μ which are no longer supressed by the lattice spacing, only the coupling g. These lattice artefacts have no continuum analogue and can become large, destroying the connection between continuum and lattice operators. However in reference [38] it is shown that a simple mean field renomalisation as shown in Eqn. 2.3.3 is sufficient to remove the effect of the tadpole diagrams. The tadpole coefficient u_0 is taken as the fourth root of the average plaquette and is tuned non-perturbatively on the lattice.

Turning back to the fermionic sector, the Wilson quark action has $\mathcal{O}(a)$ errors due to discretisation. These errors can be systematically reduced using the Symanzik improvement procedure. In the continuum there are five possible dimension five operators that can be added to the lagrangian.

$$\begin{aligned}
\mathcal{L}_1^{(1)}(x) &= \bar{\psi}(x)\sigma_{\mu\nu}F_{\mu\nu}(x)\psi(x), \\
\mathcal{L}_1^{(2)}(x) &= \bar{\psi}(x)\overrightarrow{D}_\mu(x)\overrightarrow{D}_\mu(x)\psi(x) + \bar{\psi}(x)\overleftarrow{D}_\mu(x)\overleftarrow{D}_\mu(x)\psi(x), \\
\mathcal{L}_1^{(3)}(x) &= m\mathrm{tr}[G_{\mu\nu}(x)G^{\mu\nu}(x)], \\
\mathcal{L}_1^{(4)}(x) &= m(\bar{\psi}(x)\gamma_\mu\overrightarrow{D}_\mu(x)\psi(x) - \bar{\psi}(x)\gamma_\mu\overleftarrow{D}_\mu(x)\psi(x)), \\
\mathcal{L}_1^{(5)}(x) &= m^2\bar{\psi}\psi(x).
\end{aligned}$$

Using the field equations for the ψ fields results in the following relations,

$$\mathcal{L}_1^{(1)} - \mathcal{L}_1^{(2)} + 2\mathcal{L}_1^{(5)} = 0, \qquad \mathcal{L}_1^{(4)} + 2\mathcal{L}_1^{(5)} = 0. \tag{2.3.4}$$

It is therefore possible to eliminate $\mathcal{L}_1^{(2)}$ and $\mathcal{L}_1^{(4)}$. It is also simple to absorb $\mathcal{L}_1^{(3)}$ and $\mathcal{L}_1^{(5)}$ into terms which already appear in the action as redefinitions of the couplings, so all that is needed is the single term $\mathcal{L}_1^{(1)}$. This allows one to write down a single lattice operator known as the *Sheikholeslami-Wohlert* [39] or *clover* term, needed to improve the action to $\mathcal{O}(a)$,

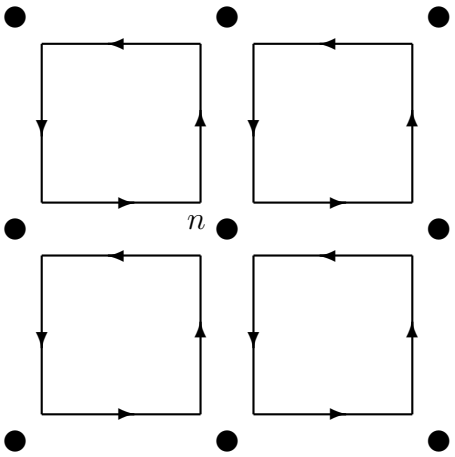

FIGURE 2.4: The clover operator $\widehat{G}_{\mu\nu}(n)$, showing the four plaquettes in $Q_{\mu,\nu}(n)$.

$$c_{SW} a^5 \sum_{n\in\Lambda} \sum_{\mu<\nu} \bar{\psi}(n) \frac{1}{2} \sigma_{\mu\nu} \widehat{G}_{\mu\nu}(n) \psi(n). \tag{2.3.5}$$

Here $\sigma_{\mu\nu} = [\gamma_\mu, \gamma_\nu]/2$. It is named the clover term due to the resemblence to a four leaved clover as shown in Figure 2.4. The coefficient c_{SW} must be tuned so as to cancel the $\mathcal{O}(a)$ errors. The operator $\widehat{G}_{\mu\nu}$ is given as a sum over the four plaquettes about the point n,

$$\widehat{G}_{\mu\nu} = -\frac{i}{8a^2}(Q_{\mu\nu} - Q_{\nu\mu}), \quad Q_{\mu\nu} \equiv U_{\mu,\nu}(n) + U_{\nu,-\mu}(n) + U_{-\mu,-\nu}(n) + U_{-\nu,\mu}(n). \tag{2.3.6}$$

In the generation of the gauge fields, there can often be large fluctuations between the individual links. This leads to short distance UV physics which is not of much interest to low energy spectroscopy. With this in mind, one final adjustment to the fermionic action is necessary. The gauge links appearing in the action are *smeared*. Simply, this refers to replacing a link variable with some average of the nearby links. This has been shown to greatly reduce the effect of the high frequency modes of the theory.

Simple methods such as APE [40] or HYP [41] smearing can be used where one takes a weighted average of the nearest *staples*, ie. the remaining links in the plaquettes containing the original link.

$$C_\mu(n) = \sum_{\nu \neq \mu} \rho_{\mu\nu} \left(U_\nu(n) U_\mu(n+\hat{\nu}) U_\nu^\dagger(n+\hat{\mu}) + U_\nu^\dagger(n-\hat{\nu}) U_\mu(n-\hat{\mu}) U_\nu(x-\hat{\nu}+\hat{\mu}) \right). \tag{2.3.7}$$

$\rho_{\mu\nu}$ is a tunable parameter which allows one to choose which links to include, for instance the smearing can be chosen to be only in the spatial or temporal directions. In these simple methods, the new link variable is generally not a member of $SU(3)$ and so must be projected back into the group. This projection step is not differentiable and can be problematic when generating these gauge configurations. However for this work a more refined analytic method known as *Stout smearing* is used, [42], making the replacement

$$U_\mu(n) \to U'_\mu(n) = e^{iQ_\mu(n)} U_\mu(n). \tag{2.3.8}$$

Q_μ is a traceless Hermitian matrix constructed from the perpendicular staples about $U_\mu(n)$ such that $e^{iQ_\mu(n)} \in SU(3)$. Hence the new link variable is automatically a member of $SU(3)$ and no projection back into the group is needed. Applying this smearing procedure iteratively many times results in what is known as a *stout* link. Due to the exponential structure of this smearing algorithm these stout links can be thought of as an incredibly large sum over different paths around the lattice, and operators formed from these link have been shown to have much greatly reduced exposure to the aforementioned UV divergences [42].

2.4 The Final Action

The discretised action used in the work described in this thesis can now be presented. A discussion on the tuning for many of the action parameters as well as the technicalities of generation of the configurations can be found in [28, 43]. As mentioned before, this work is performed anisotropic lattices where $a_s \neq a_t$, and so there is a further splitting of the action into spatial and temporal components. This gives a greater resolution in the temporal direction allowing for the more robust extraction of excited state energies, which will be discussed in more detail in Chapter 3.

In the gauge sector the action is given as

$$S_G^{\xi}[U] = \frac{\beta}{N_c\gamma_g}\left\{\sum_{x,s\neq s'}\left[\frac{5}{6u_s^4}\Omega_{P_{ss'}}(x) - \frac{1}{12u_s^6}\Omega_{R_{ss'}}(x)\right] + \sum_{x,s}\gamma_g^2\left[\frac{4}{3u_s^2u_t^2}\Omega_{P_{st}}(x) - \frac{1}{12u_s^4u_t^2}\Omega_{R_{st}}(x)\right]\right\}. \tag{2.4.1}$$

This is the Symanzik improved Wilson gauge action with tadpole improved coefficients as described in the previous sections. $\Omega_W = \mathrm{ReTr}(1-W)$ where $W = P$ is the standard plaquette and $W = R$ is the 2×1 rectangular Wilson loop. u_s and u_t are the spatial and temporal tadpole factors respectively. The term γ_g is the bare gauge anisotropy. N_c is the number of colours and $\beta = 2N_c/g^2$. The errors here are $\mathcal{O}(a_2^4, a_t^2, g^2a_s^2)$.

For the fermionic action, the anisotropic clover action with stout smearing of the link variables in the spatial directions is used.

$$S_F^{\xi}[U,\bar{\psi},\psi] = \sum_x \bar{\hat{\psi}}(x)\frac{1}{\tilde{u}_t}\left\{\tilde{u}_t\hat{m}_0 + \gamma_t\hat{W}_t + \frac{1}{\gamma_f}\sum_s\gamma_s\hat{W}_s - \frac{1}{2}\left[\frac{1}{2}(\frac{\gamma_g}{\gamma_f}+\frac{1}{\xi_R})\frac{1}{\tilde{u}_t\tilde{u}_s^2}\sum_s\sigma_{ts}\hat{F}_{ts} + \frac{1}{\gamma_f}\frac{1}{\tilde{u}_s^3}\sum_{s<s'}\sigma_{ss'}\hat{F}_{ss'}\right]\right\}\hat{\psi}(x). \tag{2.4.2}$$

Here, γ_f is the bare fermion anisotropy and $\xi = a_s/a_t$ is the renormalised anisotropy. As before $\sigma_{\mu\nu} = \frac{1}{2}[\gamma_\mu,\gamma_\nu]$. Hats denote dimensionless quantites and $W_\mu \equiv \nabla_\mu - \frac{1}{2}\gamma_\mu\Delta_\mu$ is the Wilson quark operator as discussed before. $\tilde{u}_s$ and $\tilde{u}_t$ are tadpole factors formed from the smeared links of the fermion action. The temporal and spatial clover coefficients are given by $c_t = \frac{1}{2}(\frac{\gamma_g}{\gamma_f}+\frac{1}{\xi_R})\frac{1}{\tilde{u}_t\tilde{u}_s^2}$ and $c_s = \frac{\nu}{\tilde{u}_s^3}$. Numerical values for the action parameters used are shown in Table 2.1.

	β	u_s	$\tilde{u}_s$	u_t	$\tilde{u}_t$	γ_g	γ_f	ν	c_s	c_t
light	1.5	0.7336	0.9267	1	1	4.3	3.4	1.265	1.589	0.902
charm	1.5	0.7336	0.9267	1	1	4.3	3.98	1.078	1.345	0.793

TABLE 2.1: Action parameters used in both the light and charm sectors.

To summarise what was discussed in this chapter:

1. To investigate the theory of QCD the action, S, is discretised by restricting the quark fields to the points of a lattice while assigining the gauge field to the links in between points, naturally regulating the theory.

2. Simple discretisations lead to large errors of the order of the lattice spacing as well as other non-trivial problems such as fermion doubling. Improved discretised actions can be created using the Symanzik improvement procedure, to mitigate these effects.

3. Using Monte Carlo estimation techniques, an ensemble of gauge configurations weighted by $e^{-S_G}\det(D[U])$ is generated according to the path integral Eqn. 2.2.13. The value of an observable can then be estimated as an average over its value on the individual configurations.

4. Quark propagators can be estimated by inverting the lattice Dirac matrix and used to calculate correlation functions involving fermionic operators, such as two-point meson correlation functions.

Chapter 3

Lattice Hadron Spectroscopy

Our main aim is to use the technology of lattice QCD discussed in the previous chapter to investigate the spectrum of charmed mesons. In doing this we have a way to test the theory of QCD, by comparing results to experiment. The simplest quantities one can investigate on the lattice are the ground state energies of the lower lying hadrons. These are relatively well understood and have long been used in benchmark calculations for lattice QCD which in recent years have achieved unprecedented precision [20, 21, 44–46]. More recently many investigations of the spectrum of higher lying excitations of these hadrons have been performed [22, 24, 47–49].

This chapter begins with a discussion on lattice correlation functions from which the necessary spectroscopic information can be extracted. This is followed by an introduction to the technology pioneered by the Hadron Spectrum Collaboration used to analyse these spectra. It will be shown that energies of excited states can be found from diagonalising a correlation matrix of many different correlation functions by solving a generalised eigenvalue problem. This process is made possible by the introduction of a special quark smearing algorithm known as distillation [50] which allows for the efficient computation of a myriad of different correlators. The use of appropriate lattice operators in these correlators will allow for the post hoc identification of the spin of the hadronic states.

3.1 Correlation Functions

It is well known from QFT that in the continuum it is the two point correlation function that contains all the necessary spectral information about a particular theory. In the same way, to investigate the spectrum of lattice QCD one must calculate and analyse two point correlation functions on the lattice separated by time $t = n_t a_t$, shown below in Eqn. 3.1.1.

$$C_{ij}(t) = \langle 0|O_i(t)O_j^\dagger(0)|0\rangle. \tag{3.1.1}$$

Here $O_j^\dagger$ and O_i are known as interpolating operators [1]. These interpolators are functionals of the lattice fields which create or annihilate states of the theory on the lattice. These take the form of Dirac bilinears, coupled with lattice derivatives which allow for the interpolation of a range of states with different quantum numbers. The construction of these interpolators will be discussed at length later on in this chapter. It is now relatively straightforward to see by inserting a complete set of states of the lattice Hamiltonian into Eqn. 3.1.1, that the correlation function contains a whole tower of discrete states, labelled by their energy E_n,

$$C_{ij}(t) = \langle 0|e^{Ht}O_i(0)e^{-Ht}O_j^\dagger(0)|0\rangle = \sum_n \frac{1}{2E_n} e^{-E_n t}\langle 0|O_i(0)|n\rangle\langle n|O_j^\dagger(0)|0\rangle. \tag{3.1.2}$$

This is a large, albeit finite and discrete sum, owing to the fact that the theory has been discretised on a finite lattice. That being said, all possible allowed states with the same quantum numbers as the interpolating operators are now represented here. This equation can be rewritten as

$$C_{ij}(t) = \sum_n \frac{Z_i^n Z_j^n}{2E_n} e^{-E_n t}. \tag{3.1.3}$$

[1] We will use the terms interpolator and operator interchangeably to refer to these interpolating operators

$Z_j^n = \langle n|O_j^\dagger|0\rangle$ is known as an *overlap factor*, which is a time independent measure of how strongly the state created from the vacuum by the interpolator $O_j^\dagger$ overlaps with the eigenstate n of the Hamiltonian.

It would be impossible to extract accurate spectroscopic information for any one state from this sum as written, however it is evident that if the temporal separation between the interpolators is taken to be large the ground state energy dominates this sum as

$$\Rightarrow \lim_{t\to\infty} C_{ij}(t) \sim e^{-E_0 t}. \tag{3.1.4}$$

Traditionally this method was used to determine the ground state energies, however we are primarily interested in extracting the energies of excited states in the spectrum. Unfortunately, at lager t, any signal of interest will have decayed considerably and the signal to noise ratio will no longer be negligible. So the separations need to be kept as small as possible but large enough so that the exponential in Eqn. 3.1.2 has had time to suppress most of the unwanted energies.

It is therefore necessary to utilise interpolators that create and annihilate the lower states of the spectrum with greater efficiency, to filter out contamination from other states in the sum of Eqn. 3.1.2 relatively quickly. If the overlaps of these interpolators with the states in question were exact, the correlation function would plateau to the energy E_n for all t and the energy could be extracted straightforwardly, however there will always be some small contamination from other states in the theory at small times. The use of anisotropic lattices minimises the effect of this contamination as it provides a finer temporal than spatial resolution and so allows for a more accurate extraction without increasing the computational cost as much as isotropically reducing a would.

3.2 Interpolator Construction

At their most basic, the meson interpolators used in the aforementioned correlators are color-singlet local fermion bilinears of the form

	Scalar	Pseudo-scalar	Vector	Axial-Vector	Tensor
Γ	$1/\gamma_0$	$\gamma_5/\gamma_0\gamma_5$	$\gamma_i/\gamma_0\gamma_i$	$\gamma_5\gamma_i$	$\gamma_i\gamma_j$
J^{PC}	0^{++}	0^{-+}	1^{--}	1^{++}	1^{+-}
Name	a_0/b_0	π/π_2	ρ/ρ_2	a_1	b_1

TABLE 3.1: Gamma matrix quantum numbers, along with the naming scheme used.

$$O \sim \bar{\psi}_{i\alpha}(\vec{x},t)\Gamma_{\alpha\beta}\psi_{i\beta}(\vec{x},t), \tag{3.2.1}$$

a gauge covariant combination of lattice quark fields ψ and a Dirac gamma matrix Γ. Colour and spinor indicies will be suppressed in equations from now on. These interpolators can again be labelled by their angular momentum, parity and charge conjugation quantum numbers J^{PC}. The charge conjugation and parity quantum numbers of the operator are dependant on the choice of gamma matrix Γ, whose different possible combinations are listed in Table 3.1. It is clear that these simple interpolators do not allow for angular-momentum greater than one nor do they permit any exotic quantum number combinations, such as 0^{+-} and 1^{-+} as discussed in Chapter 1.

To have access to these exotic J^{PC} as well as states with spin $J > 1$ one must use non-local operators. This necessitates the introduction of the spatially directed, gauge covariant, lattice forward-backward derivative $\overleftrightarrow{D} \equiv \overleftarrow{D} - \overrightarrow{D}$. In the construction of these operators a circular basis of these derivatives is formed, which transforms as spin $J = 1$.

$$\begin{aligned}
\overleftrightarrow{D}_{m=+1} &= -\frac{i}{\sqrt{2}}(\overleftrightarrow{D}_x + i\overleftrightarrow{D}_y), \\
\overleftrightarrow{D}_{m=0} &= i\overleftrightarrow{D}_z, \\
\overleftrightarrow{D}_{m=-1} &= \frac{i}{\sqrt{2}}(\overleftrightarrow{D}_x - i\overleftrightarrow{D}_y).
\end{aligned} \tag{3.2.2}$$

Using this new basis and the rules for addition of angular momentum, along with the Clebsch-Gordon coefficients of $SO(3)$, the necessary higher spin interpolators

can be created as described in reference [24]. In this thesis, interpolators of up to spin $J = 4$ are used. All of the operators used have the form

$$O \sim \sum_{m_1,m_2,m_3,...} CGs(m_1, m_2, m_3, ...) \sum_{\vec{x}} \bar{\psi}(\vec{x}, t)\Gamma_{m_1} \overleftrightarrow{D}_{m_2} \overleftrightarrow{D}_{m_3} ... \psi(\vec{x}, t), \quad (3.2.3)$$

where the sum over spatial sites $\vec{x}$ projects to zero momentum. The construction of interpolators at non zero momentum will be discussed later. The simplest example comprises of one spin $J = 1$ covariant derivative coupled to a single vector-like gamma matrix which allows for the creation of an interpolator with spin $J = 0, 1, 2$, and J_z projection M.

$$(\Gamma \times D^{[1]}_{J=1})^{J,M} = \sum_{m_1,m_2} \langle 1, m_1; 1, m_2 | J, M \rangle \, \bar{\psi}\Gamma_{m_1} \overleftrightarrow{D}_{m_2} \psi. \quad (3.2.4)$$

To create interpolators of higher spins necessitates the inclusion of more derivatives, which are chosen to couple to each other first. For example, to create a spin $J = 3$ state one first couples two spin $J = 1$ derivitives to give definite spin $J_D = 0, 1, 2$ which can be then coupled to a vector-like gamma matrix to give total spin $J = 3$, as shown in Eqn. 3.2.5.

$$(\Gamma \times D^{[2]}_{J_D})^{J,M} = \sum_{\substack{m_1,m_2,\\ m_3,m_D}} \langle 1, m_3; J_D, m_D | J, M \rangle \, \langle 1, m_1; 1, m_2 | J_D, m_D \rangle \, \bar{\psi}\Gamma_{m_3} \overleftrightarrow{D}_{m_1} \overleftrightarrow{D}_{m_2} \psi. \quad (3.2.5)$$

With the inclusion of three or more derivatives, a convention for how to couple the various derivatives together is needed. Coupling the derivatives so that the operator has definite charge conjugation symmetry is an appropriate choice. The use of the forward-backward derivative allows this by simply coupling the outer most derivatives first, shown below, as the act of charge conjugation basically amounts to transposing the operators between the quark fields, which are interchanged under charge conjugation. As this work uses only operators with $J \leq 4$ there need be at most three derivatives, as shown in Eqn 3.2.6, however this procedure generalises readily to higher spins.

$$(\Gamma \times D^{[3]}_{J_{13},J_D})^{J,M} = \sum_{\substack{m_1,m_2,\\ m_3,m_4\\ m_{13},m_D}} \langle 1, m_4; J_D, m_D | J, M\rangle \langle 1, m_2; J_{13}, m_{13} | J_D, m_D\rangle \times \langle 1, m_1; 1, m_3 | J_{13}, m_{13}\rangle \bar{\psi}\Gamma_{m_4} \overleftrightarrow{D}_{m_1} \overleftrightarrow{D}_{m_2} \overleftrightarrow{D}_{m_3} \psi. \quad (3.2.6)$$

It is possible to form an interpolator comprising solely of two lattice covariant derivatives with spin $J_D = 1$ which is non zero on non-trivial gauge configurations. This operator is proportional to the commutator of the derivatives and hence the gluonic field strength tensor and so is useful in investigations of hybrid states or glueballs.

3.3 Symmetry on the Lattice

Once a quantum field theory has been discretised on a lattice it is evident that the full rotational symmetry of the continuum is explicitly broken, and one can no longer label individual states of the theory by their continuum spin J. However lattice operators must create eigenstates of the lattice Hamiltonian with well defined quantum numbers, ie. they must transform in an irreducible representation, or irrep, of the reduced symmetry group of the lattice. It is then possible to label the states by these irreps and only later assign a continuum spin to each state in the spectrum. The process of assigning a continuum spin to a certain excitation will be discussed later in greater depth.

The symmetry group of the lattice is that of the octahedral group, O_h, of order 48, of rotations and reflections of a cube. Focusing on the subgroup of rotations only, the 24 elements of the group can be divided into five different conjugacy classes. This leaves five irreducible representations, Λ, which are named A_1, A_2, E, T_1, T_2, with dimensions (1,1,2,3,3) respectively.

Each interpolator used in the lattice computation must transform in one of these irreps. The process of distributing the various M components of these operators into the various lattice irreps is known as subduction. The pattern of subduction for various spins is shown in Table 3.2. For example spin $J = 2$ subduces into

Spin J	Λ(dim)
0	$A_1(1)$
1	$T_1(3)$
2	$E(2) \oplus T_2(3)$
3	$A_2(1) \oplus T_1(3) \oplus T_2(3)$
4	$A_1(1) \oplus E(2) \oplus T_1(3) \oplus T_2(3)$

Λ	Contributing Spins
A_1	0,4,6,8,...
A_2	3,6,7,9,...
E	2,4,5,6,...
T_1	1,3,4,5,...
T_2	2,3,4,5,...

TABLE 3.2: The irreducible representations of the octahedral group a certain spin J will be subjuced into as well as which spins contribute to each individual irrep.

the five dimensional sum of irreps $E(2) \oplus T_2(3)$, ie. the five spin projections $M = (-2, -1, 0, 1, 2)$ are distributed across these two irreps.

Once the pattern of subduction is known, it is possible to construct an interpolator $O^{[J]}_{\Lambda,\lambda}$ which transforms irreducibly in one irrep, Λ, as an appropriate linear combination of the individual M projections.

$$O^{[J]}_{\Lambda,\lambda} \equiv (\Gamma \times D^{[n_D]}_{\dots})^{J}_{\Lambda,\lambda} = \sum_{M} S^{J,M}_{\Lambda,\lambda} (\Gamma \times D^{[n_D]}_{\dots}) \equiv \sum_{M} S^{J,M}_{\Lambda,\lambda} O^{J,M}. \tag{3.3.1}$$

Here λ is the *row* of the irrep which runs from 1 to dim(Λ). The $S^{J,M}_{\Lambda,\lambda}$ are known as subduction coefficients. As a trivial example, the subduction coefficient for a $J = 0$ interpolator which only appears in A_1 is $S^{0,0}_{A_1,1} = 1$. T_1 forms a faithful representation of $J = 1$ shown in Table 3.3, where each row, λ, is in one to one correspondence to an M component. In general, for higher spins the subduction coefficients can be constructed starting from the $J = 0$ and $J = 1$ coefficients as

$$S^{J,M}_{\Lambda,\lambda} = N \sum_{\lambda_1,\lambda_2} \sum_{M_1,M_2} S^{J_1,M_1}_{\Lambda_1,\lambda_1} S^{J_2,M_2}_{\Lambda_2,\lambda_2} C \begin{pmatrix} \Lambda & \Lambda_1 & \Lambda_2 \\ \lambda & \lambda_1 & \lambda_2 \end{pmatrix} \langle J_1, M_1; J_2, M_2 | J, M \rangle \,. \tag{3.3.2}$$

λ^M	1	0	-1
1	1	0	0
2	0	1	0
3	0	0	1

TABLE 3.3: Subduction coefficients for $(J = 1) \to T_1$.

where $C\begin{pmatrix} \Lambda & \Lambda_1 & \Lambda_2 \\ \lambda & \lambda_1 & \lambda_2 \end{pmatrix}$ is the octahedral group Clebsch-Gordon coefficient for $\Lambda_1 \otimes \Lambda_2 \rightarrow \Lambda$. For more information on the construction of these subduction coefficients see reference [24]. It is important to note that a subduced operator transforming in a certain irrep, Λ, will have some overlap with all spins in that irrep. However the operator still has some memory of the spin from which it was subduced and it is this fact that allows for the identification of the continuum spin of the various states in the spectrum [24].

3.4 Distillation

Armed with the lattice subduced operators, one can now proceed with the calculation of the correlation function in Eqn. 3.1.1. However these operators still overlap with a tower of unwanted states in any given irrep. This necessitates a procedure to minimise this excited state contamination. *Smearing* of the quark fields is the most useful tool at a lattice practitioner's disposal in this regard. Rather than using the quark fields which appear in the action directly, the process of smearing involves applying a smearing operator which filters out the short distance fluctuations from the fields in the path-integral, leaving behind the longer distance modes of interest for hadron physics. The most well known method applies the gauge covariant second-order three-dimensional lattice Laplacian operator

$$-\nabla^2_{xy}(t) = 6\delta_{xy} - \sum_{j=1}^{3}(\tilde{U}_j(x,t)\delta_{x+\hat{j},y} + \tilde{U}^\dagger_j(x-\hat{j},t)\delta_{x-\hat{j},y}), \tag{3.4.1}$$

where the gauge fields $\tilde{U}$ have been appropriately smeared using a gauge smearing procedure such as stout smearing, as discussed in Chapter 2. From this one can define a smearing operator as

$$J_{\sigma,n_\sigma}(t) = \left(1 + \frac{\sigma\nabla^2(t)}{n_\sigma}\right)^{n_\sigma}, \tag{3.4.2}$$

where the smearing weight σ and n_σ are tunable parameters. Applying this smearing operator to the quark fields many times, ie. taking n_σ to be large, will exponentially supress the components which do not contribute to the physics of

interest. As suggested in reference [50], it is possible to approximate this smearing algorithm by forming an eigenvector representation, truncated to the lowest modes.

Distillation is the definition of a new smearing operator $\Box$, known as the distillation operator. This is a low rank operator, of rank $N \ll M$, where $M = N_c \times N_x \times N_y \times N_z$ is the rank of the vector space, V_M, of the three dimensional Laplacian. $\Box$ is then defined on timeslice t as a product of an $M \times N$ matrix $V(t)$ and its hermitian conjugate

$$\Box(t) = V(t)V^\dagger(t) \rightarrow \Box_{xy}(t) = \sum_{k=1}^{N} v_x^{(k)} v_y^{(k)\dagger}(t). \tag{3.4.3}$$

Here $v^{(k)}$ are the first N eigenvectors of the lattice Laplacian, ∇^2, ordered by eigenvalue. It is apparent here that the distillation operator is a projection operator as $\Box^2 = \Box$, which projects into the distillation subspace V_N spanned by the N lowest eigenvectors.

Distillation smearing is effectively a choice of fields to use in the operators, where the smeared fields are defined as $\tilde{\psi} = \Box\psi$. The choice of how many distillation vectors to use, N, is important. It is clear that if the number of distillation vectors is chosen to be maximal, ie. when $N = M$, that the distillation operator is then given by the identity and the fields remain unchanged whereas if N is taken to be too small then too much information is lost. It is shown in reference [50] that an appropriate value of N does indeed dampen the effect of the unwanted higher excited modes in the correlator allowing for an accurate energy to be extracted at earlier times.

It is also worth noting that the distillation operator transforms as a scalar under rotations, is covariant under gauge transformations and is parity and charge conjugation invariant, so the newly smeared fields transform in the correct way.

One of the technical benefits of using distillation to smear the quark fields is that it greatly simplifies the calculation of correlation functions needed for spectroscopic calculations. The correlation function seen in Eqn. 3.1.1 can be expanded by inserting simple bilinear interpolators $\bar{\psi}\Gamma\psi$ as

FIGURE 3.1: A simple schematic representation of the connected (left) and disconnected (right) parts of the correlation function shown in Eqn. 3.4.4.

$$\begin{aligned} C_{ij}(t) &= \langle 0|\bar{\psi}_x(t)\Gamma^i_{xy}(t)\psi_y(t)\cdot\bar{\psi}_w(0)\Gamma^j_{wz}(0)\psi_z(0)|0\rangle \\ &= -\mathrm{Tr}[M^{-1}_{zx}(0,t)\Gamma^i_{xy}(t)M^{-1}_{yw}(t,0)\Gamma^j_{wz}(0)] \\ &\quad +\mathrm{Tr}[M^{-1}_{yx}(t,t)\Gamma^i_{xy}(t)]\mathrm{Tr}[M^{-1}_{zw}(0,0)\Gamma^j_{wz}(0)], \end{aligned} \tag{3.4.4}$$

where in the second line a Wick contraction over the quark fields has been performed, leaving just a trace over products of the quark propagators and gamma matrices. The first term is understood as the connected part of the correlator, that is, it describes the propagation of quarks between the source at time 0 to sink at time t. The second term, a product of two traces, is related to the disconnected portion of the correlator, and describes two different propagations from a point back to itself. Both terms are shown in Figure 3.1.

It is clear that the calculation of these correlators amounts to the calculation of quark propagators. Traditionally disconnected diagrams were not included in calculations as they are notoriously noisy and prohibitively expensive to calculate as they include propagators of the form $M^{-1}_{yx}(t,t)$, which must be calculated at every point of the lattice. Distillation allows for a simple solution. By smearing the quark fields in the interpolators it amounts to making the substitution

$$O_i(t) = \bar{\psi}(t)\Gamma^i(t)\psi(t) \rightarrow \bar{\psi}\Box(t)\Gamma^i(t)\Box\psi(t). \tag{3.4.5}$$

Then performimg the same Wick contraction as before by evaluating the quark field portion of the path integral results in, for the connected part of the correlator,

$$\begin{aligned} C_{ij}(t) &= -\mathrm{Tr}[M^{-1}(0,t)\Box(t)\Gamma^i(t)\Box(t)M^{-1}(t,0)\Box(0)\Gamma^j(0)\Box(0)] \\ &= -\mathrm{Tr}[V^\dagger(0)M^{-1}(0,t)V(t)V^\dagger(t)\Gamma^i(t)V(t)V^\dagger(t)M^{-1}(t,0)V(0)V^\dagger(0)\Gamma^j(0)V(0)] \\ &= -\mathrm{Tr}[\tau(0,t)\Phi^i(t)\tau(t,0)\Phi^j(0)], \end{aligned} \tag{3.4.6}$$

where

$$\tau_{\alpha\beta}(t,0) = V^\dagger(t)M^{-1}_{\alpha\beta}(t,0)V(t), \tag{3.4.7}$$

$$\Phi^i_{\alpha\beta}(t) = V^\dagger(t)[\Gamma^i(t)]_{\alpha\beta}V(t). \tag{3.4.8}$$

The correlator can now be written as a simple product of τs and Φs. Φ contains the particular operator construction, while τ, known as a *perambulator*, describes quark propagation. The choice of source and sink interpolators is entirely independent of the computation of τ, and contains only information about the individual quark propagators. This means that the perambulators can be computed and stored and then used at a later time to construct correlators containing any source or sink operators, greatly decreasing the time needed to compute large numbers of correlation functions.

The size of the matrices $\tau_{\alpha\beta}$ and $\Phi^i_{\alpha\beta}$ depends on the number of distillation vectors chosen. They are of size $N \times N_\sigma$ where N_σ is the number of components of a lattice Dirac spinor, and hence it takes this many inversions of the Dirac matrix M to calculate the perambulators. This number is $\mathcal{O}(100)$ with a reasonable number of distillation vectors, orders of magnitude smaller than the size of the full Dirac matrix which can be $\mathcal{O}(10^8)$. This allows for the computation of many correlation functions quickly, as well as providing access to disconnected correlators. Following the same procedure above one finds for the disconnected part of the correlator

$$C_{ij}(t) = \mathrm{Tr}[\Phi^i(0)\tau(0,0)]\mathrm{Tr}[\Phi^j(t)\tau(t,t)], \tag{3.4.9}$$

where the necessity of calculating $M^{-1}_{yx}(t,t)$ has been replaced with the perambulator $\tau(t,t)$, which is computationally more accessible. This process readily extends to more complicated correlation functions such as three-point functions.

3.5 The Variational Method

We have seen how a correlation function of the form in Eqn. 3.1.1 can be used to extract the lowest energy levels of the meson spectrum. However, it has been long known that a practical way to investigate excited states on the lattice is to diagonalise a correlation matrix of a large basis of creation and annihilation operators $\{O_i, O_j^\dagger\}$ [51, 52],

$$C_{ij}(t) = \langle 0|O_i(t)O_j^\dagger(0)|0\rangle. \tag{3.5.1}$$

This equation is now to be thought of as a matrix with i and j running from 1 to n. One such correlation matrix is calculated for each irrep of interest. Once again, the distillation method allows for the calculation of many correlation functions between operators in the basis at computationally little cost, and it is prudent to take advantage of the ability to create many redundant interpolators in each symmetry channel.

Intuitively, it is reasonable for one to assume that there is some linear combination of interpolators contained in the basis that will overlap most strongly with the desired eigenstates and hence be useful in achieving a strong signal for the excited states. It can be shown that the optimal linear combinations are found by solving a generalised eigenvalue problem (GEVP) of the form

$$C_{ij}(t)v_j^n = \lambda^n(t, t_0)C_{ij}(t_0)v_j^n. \tag{3.5.2}$$

Here the λ^n are know as the *generalised eigenvalues*, or *principal correlators*, and are related to the energies of the n states in the spectrum. v^n are known as the *generalised eigenvectors* and are related to the operator state overlaps from Eqn. 3.1.3 as

$$Z_j^n = \sqrt{2m_n}e^{m_n t_0/2}v_i^{n*}C_{ij}(t_0). \tag{3.5.3}$$

t_0 is a carefully chosen reference timeslice on which the eigenvectors are orthogonal, ie. ${v^{n'}}^\dagger C(t_0)v^n = \delta_{n,n'}$, with $\lambda_n(t_0) = 1$. Due to the finite nature of the interpolator basis, it is important to take care in choosing a t_0 that is large enough [22]. If

the correlator is not dominated by the lightest n states on the chosen timeslice t_0, because higher excited states still contribute with a significant signal, then the orthogonality relation on $C(t_0)$ will not be valid. So it is necessary for t_0 to be large enough that the higher excited states have decayed away but not so high as to just extract noise.

Eqn. 3.5.2 is solved independently on each timeslice, and to ensure the ordering of the energies is consistent, eigenvectors for each t are compared to reference eigenvectors taken from some reference t. The actual calculation is performed using singular value decomposition (SVD) on $C(t_0)$ to recast Eqn. 3.5.2 as an ordinary eigenvalue problem. At large times the principal correlators behave as

$$\lambda_n(t, t_0) \sim e^{-E_n(t-t_0)} + O(e^{-E_{n+1}(t-t_0)}). \tag{3.5.4}$$

From this one can extract the spectroscopic data necessary by fitting the principal correlators to

$$\lambda_n = (1 - A_n)e^{-E_n(t-t_0)} + A_n e^{-E'_n(t-t_0)}, \tag{3.5.5}$$

with fit parameters E_n, E'_n and A_n. The second exponential is included here to "mop up" the effect of any remnant excited states and allows one to consider the behaviour of the principal correlator at earlier times. This second exponential decreases rapidly with increasing t_0 and for sufficiently large t_0, E'_n is indeed larger than E_n as needed. This is not necessarily true for smaller t_0, which is indicative of forcing an incorrect orthogonality [24].

Figure 3.2 shows principal correlator fits for the first four states in the T_1^- irrep of the D_s meson spectrum for $t_0 = 10$. Points with errors above a certain threshold relative to the signal are not included in the fits, shown with red error bars on the plots. A plateau can be clearly seen in the case of the ground state which extends to late t. In the case of the excited states the plateau degrades into noise at large t but nevertheless persists long enough to extract an accurate energy for the state. The fact that the statistical uncertainty in the energies doesn't increase is due to the use of an appropriate opperator basis with the GEVP. Higher excited states can overlap with a different subset of operators to the ground state and so the signal does not necessarilly degrade going up in the spectrum.

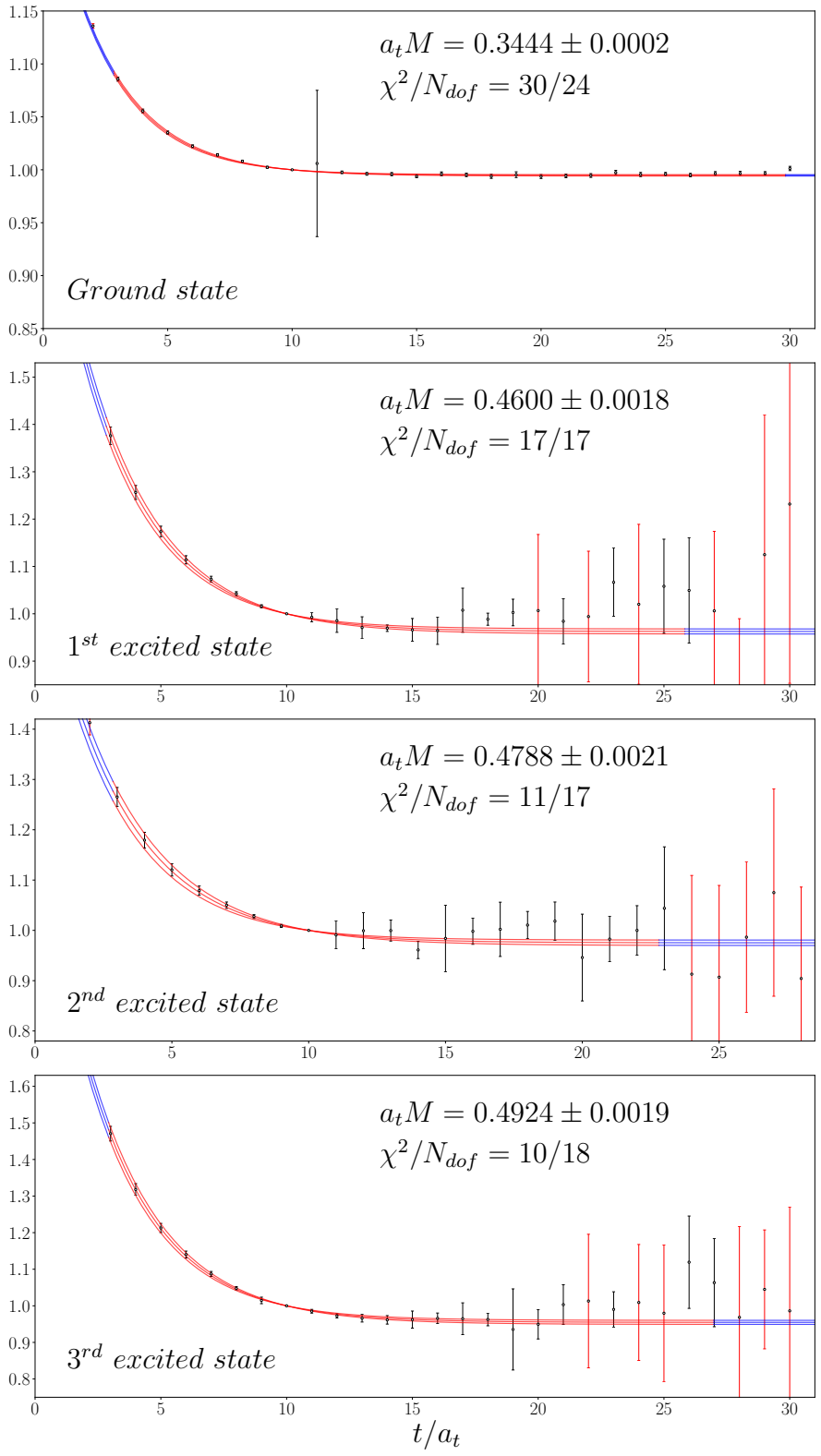

FIGURE 3.2: Example principal correlators for the first four states in the T_1^- irrep of the D_s spectrum at $t_0 = 10$. Plotted is $\lambda^n(t)e^{m_n(t-t_0)}$ with the bands showing the one sigma uncertainty in the fits. Points, shown in red, with errors above a certain threshold relative to the signal are not included in the fits.

In practice the GEVP is solved for a range of different t_0 and then the most appropriate value is chosen a posteriori via the reconstruction method as described in Reference [22]. In the reconstruction method, each energy E_n and overlap Z_i^n are calculated on a single timeslice and substituted into Eqn. 3.1.3. This newly reconstructed correlation matrix is then compared to the original for $t > t_0$ by defining a χ^2 like quantity, with the degree of agreement indicating the acceptability of the spectral decomposition. The agreement between the matrices generally improves with increasing t, up until some point where noise in the signal becomes a problem.

Figure 3.3 shows the energy in lattice units extracted from the principal correlator fits vs t_0, for the first three states in the T_1^- irrep of the D_s spectrum at $t_0 = 10$. There is little change in the energy extracted as t_0 is varied. This is expected, as the principal correlator fits included a second exponential which absorbed contributions from excited states, allowing for a more stable extracted spectrum. Larger changes in the energy vs t_0, can indicate contributions from excited states are playing a more significant role in the signal.

3.6 Spin Identification

Once the energies of the first few excitations in the spectrum have been determined by choosing an appropriate t_0 and extracting the energies from the principal correlators, one must have a way of identifying the continuum spin for each extracted energy. This is a non-trivial problem on the lattice. The most rigorous way of achieving this is to identify degeneracies across the spectrum as the continuum limit is approached.

In analyses of the spectrum as the lattice spacing is decreased, these degeneracies become more apparent. For example, as shown in Table 3.2 a spin $J = 3$ state will be subduced into the A_1, T_1 and T_2 irreps on the lattice. This state is expected to appear across these three irreps with nearly degenerate energies. In principle as the continuum limit is approached these energies should become degenerate due to the absence of discretisation effects. It would be possible to use this procedure to identify and assign a spin to each state in the spectrum.

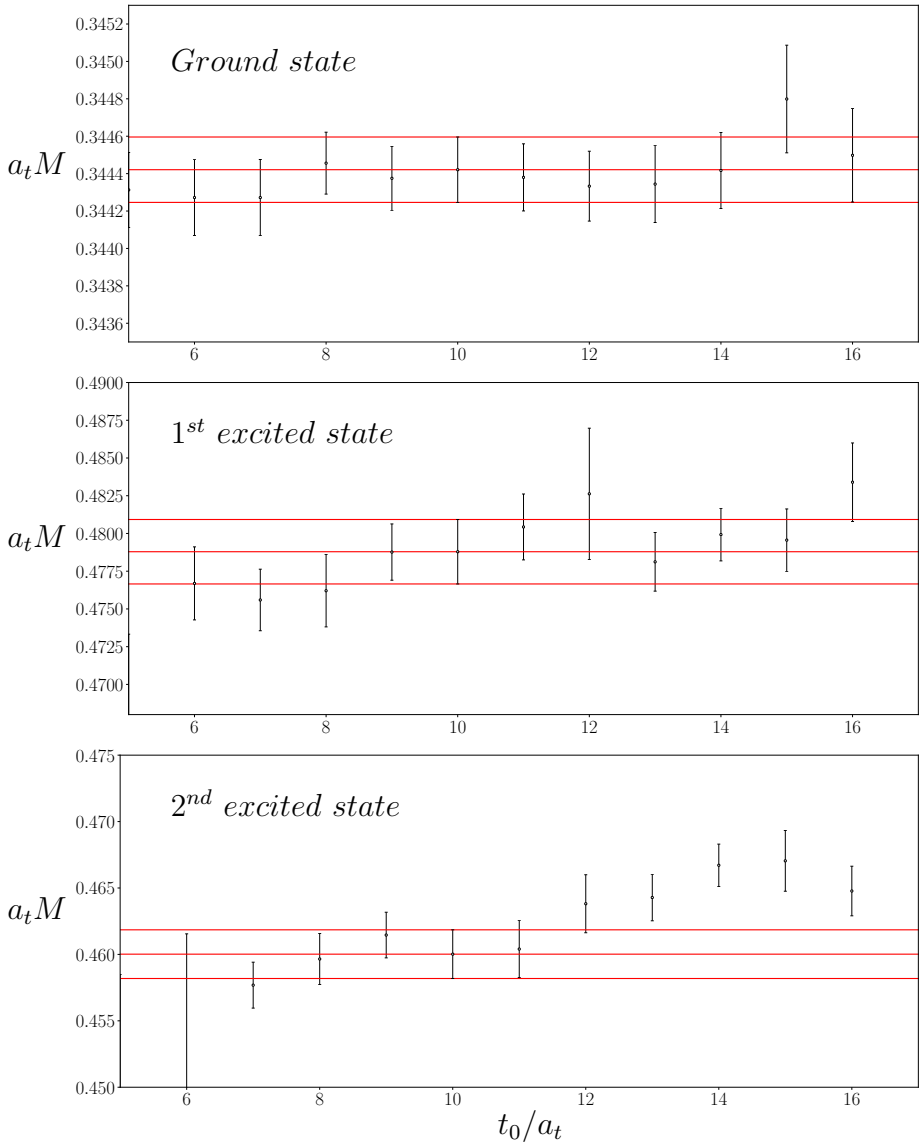

FIGURE 3.3: Example t_0 dependence of the energy for the first three states in the T_1^- irrep of the D_s spectrum at $t_0 = 10$. The bands, which are not fit to the data, show the energy, with the one sigma uncertainty, extracted from the principal correlators at $t_0 = 10$.

However in practice this method is generally problematic. The calculation of the spectra at finer and finer lattice spacing is often not feasable due to the increasing computational costs. As well as that, above the lowest lying states in the meson spectrum, many states appear with naturally nearly degenerate energies. When dealing with the reduced symmetries of the cube, these natural degeneracies are vastly magnified, due to multiple spins being subduced into a single irrep. The problem of identifying which states are naturally degenerate and which are due to the lattice discretisation becomes impossible and would require statistically precise

data beyond which is available.

Ideally there would exist a method that allows for the accurate identification of the spin of a state using data from only one lattice spacing, significantly reducing computation time. Using the methods pioneered by the Hadron Spectrum collaboration it is possible by considering the overlap factors Z_i^n of the interpolating operators. Each of these carefully constructed operators, described in the previous sections, transforms irreducibly in a certain representation of the cubic symmetry group. However, as was stated before, each of these operators contains some memory of the continuum spin operator it was subduced from [24].

As the continuum limit is approached, where the symmetry breaking is small, one would assume an operator that was subduced from $J = 1$ would have a much larger overlap with a state of the same spin as opposed to say a state of $J = 3$. In this way, if the lattice spacing is fine enough as to not break the rotational symmetry of the continuum too forcefully, one would assume that each state would have relatively strong overlaps with a subset of the operator basis, subduced from a single spin J.

This effect is seen quite strongly on the level of individual states, each of which in general show a strong preference to overlap with operators of a certain spin, as shown in Figure 3.4. Shown are the overlaps for each operator in the T_1^- irrep of the D_s spectrum, for the ground and third excited state. Operators subduced from $J = 1$ are coloured red where as operators coloured blue are subduced from $J = 3$. In each case the operators are normalised so that the largest overlap is one. It is clear that the ground state predominantly overlaps with the spin $J = 1$ operators, giving good indication that it is a spin $J = 1$ state. Similarly for the third excited state, there is strong overlap with spin $J = 3$ operators, indicating a state with spin $J = 3$.

To be even more quantitative, one can also compare the overlaps for the same states between different irreps. Obviously continuum operators will only overlap with a single spin, and therefore only spin J states should overlap with a subduced operator, not any other spins in the particular irrep the operator is in.

$$\left\langle 0|O^{J,M}|J',M'\right\rangle = Z^{[J]}\delta_{J,J'}\delta_{M,M'} \Rightarrow \langle 0|O^{[J]}_{\Lambda,\lambda}|J',M\rangle = S^{J,M}_{\Lambda,\lambda}Z^{[J]}\delta_{J,J'}. \tag{3.6.1}$$

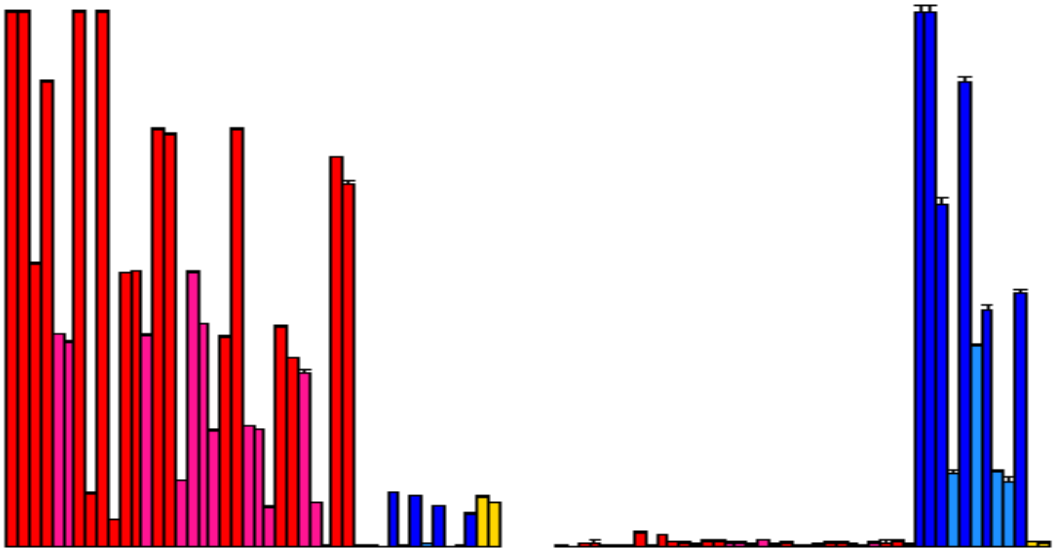

Ground state Third excited state

FIGURE 3.4: Example overlaps for the ground and third excited state in the T_1^- irrep of the D_s meson spectrum. Operators are colour coded with red being spin one and blue being spin three. In both cases the operators have been normalised so the highest overlap has a value of unity.

Using the fact that the subduction coefficients form an orthogonal matrix, or

$$\sum_M S^{J,M}_{\Lambda,\lambda} S^{J,M*}_{\Lambda',\lambda'} = \delta_{\Lambda,\Lambda'}\delta_{\lambda,\lambda'}, \tag{3.6.2}$$

it can be shown that the spectral decomposition of the correlation function has a term proportional to $Z^{[J]} * Z^{[J']}$, ie. there is no irrep dependence. It should be possible to see this manifest as similar overlap values for states degenerate across the different irreps. One would expect the Z values for the aforementioned $J = 3$ state to be similar in the A_2, T_2 and T_1 irreps. Figure 3.5 shows the operator overlaps for the lowest state identified as a spin $J = 3$ state in each irrep, again for D_s. It is evident that the overlap with the blue operators follows the same pattern across irreps, signalling the fact that it is the same state that has been identified in each irrep.

The absolute values of the overlaps, $|Z|$, for each operator can also be compared, and are expected to be degenerate for a single state subduced across different irreps. They will not be exactly degenerate due to discretisation effects however these are not too large, as shown in Figure 3.6, for three spin $J = 3$ operators. As

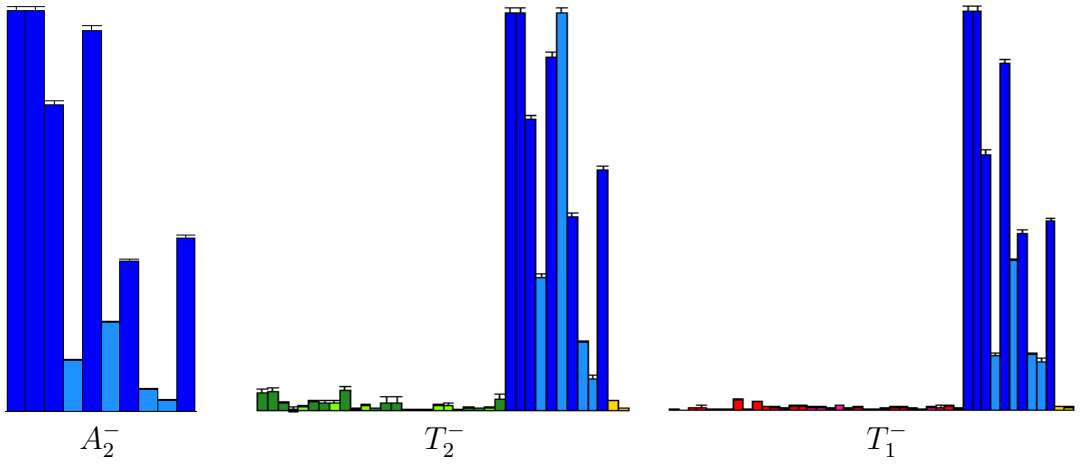

FIGURE 3.5: Comparison of operator overlaps for the first state identified with spin $J = 3$ across the A_2^-, T_2^- and T_1^- irreps in the D_s spectrum. As before in each case the operators have been normalised so that the highest overlap has a value of unity. A clear pattern across irreps can be seen.

was discussed, all states with spins $J \geq 2$ will appear with slight differences across the different irreps. This will also arise in the energies extracted from the fits to the principal correlators. Rather than averaging over the different irreps, a joint fit to each principal correlator is performed while allowing for a differing second exponential in each fit. This is generally very successful with correlated $\chi^2/N_{d.o.f.}$ values close to one.

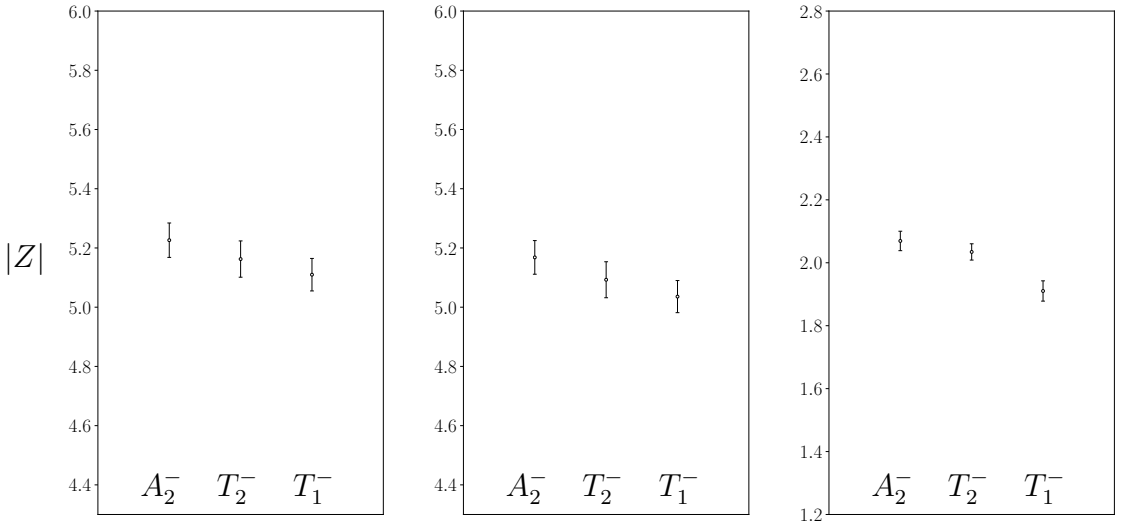

FIGURE 3.6: Absolute value for the operators overlap $|Z|$ for three different spin $J = 3$ operators across irreps A_2^-, T_2^- and T_1^- for the D_s meson. The near degeneracy of the operator overlap for in each irrep can be seen.

In summary, it has been shown how one can calculate the excited meson spectrum of QCD:

1. Create a large basis of lattice interpolators $O_i^\dagger$ with different J^{PC} combinations, from distillation smeared quark fields, with up to three latice derivatives.

2. Using these interpolators compute a matrix of cross correlations between each interpolators, $C_{ij}(t) = \langle 0|O_i(t)O_j^\dagger(0)|0\rangle$, aided by the use of distillation smeared fields.

3. The variational method is then used to solve $C_{ij}(t)v_j^n = \lambda^n(t,t_0)C_{ij}(t_0)v_j^n$, for a range of values of t_0, with an appropriate t_0 being chosen so as to ensure orthongonality of the eigenvectors.

4. Principal correlators λ^n are then fit to a two exponential fit of the form of Eqn. 3.5.5, from which the energies of the excited states in the spectrum E_n can be extracted.

5. The continuum spins of the states in the spectrum are then assigned by analysing the operator overlaps for individual states. Degeneracies across irreps are seen in the value of these overlaps and correlated fits to these degenerate states allow for the extraction of a final energy for the spin identified states.

Chapter 4

D_S and D Meson Spectrum

The spectrum of charmonium has long been a valid testing ground for lattice QCD, with comparisons of precise lattice data to experiment allowing for unprecedented probes of the theory. However investigations into the spectrum of open-charm mesons can also provide much needed insight. As mentioned before, there have been puzzling discoveries in the open-charm sector. The masses and widths of $D^*_{s0}(2317)^{\pm}$ and $D_{s1}(2460)^{\pm}$, seen at BABAR [53] and CLEO [54] have been found to be lighter and narrower than expected from quark model calculations. The nature of these enigmatic resonances is still up for debate and lattice investigations may elucidate some of this uncertainty.

In this chapter results from an investigation of the D_s and D meson spectrums which has been published in reference [1] will be discussed. This was performed on a $32^2 \times 256$ lattice with a pion mass, M_π, of approximately 236 MeV, slightly higher than its experimental value of 135 MeV. After first looking at some of the technical details of the calculation, the full meson spin spectrum calculated will be shown. This will then be used to make a comparison with data from an earlier study described in reference [48], with $M_\pi \sim 391$ MeV. This allows for an investigation into how the spectrum changes as the light quark mass is varied, which is suggested to be non-trivial for excited heavy quarkonia [55]. There has been many lattice studies into the open-charm meson spectrum, some of which focused on precision calculations of the lower lying states [44], whereas others focused on more complete spectrums including states above threshold [47, 49, 56–58]. There have also been lattice studies taking into account scattering resonances, such as [59–61]. In this

Lattice Volume	M_π (MeV)	N_{cfgs}	N_{tsrcs} for $c\bar{s}$, cl	N_{vecs}
$32^3 \times 256$	236	484	1, 2	384
$24^3 \times 128$	391	553	16, 16	162

TABLE 4.1: Details of the lattice gauge field ensembles used. Volume is given as $(L/a_s)^3 \times (T/a_t)$ where L and T are respectively the spatial and temporal extents of the lattice. The number of gauge configurations used, N_{cfgs}, and the number of time-sources used per configuration, N_{tsrcs}, are shown along with the number of eigenvectors used in the distillation N_{vecs}.

work this resonance behavior of states above threshold is not taken into account however this study paves the way towards extending earlier scattering analyses to lighter pion masses.

4.1 Calculation Details

As discussed in the previous chapter, the energies of the excitations in the spectrum are found by solving a generalised eigenvalue problem à la Eqn. 3.5.2 and extracting energies by fitting a double exponential to the generalised eigenvalues, or principal correlators λ_n. This is achieved by diagonalising a correlation matrix C_{ij} for a large basis of interpolating operators for each lattice irrep Λ.

These correlation functions are calculated on dynamical $N_f = 2 + 1$ anisotropic gauge ensembles generated with the action described in section 2.4, with details shown in Table 4.1. For both ensembles the strange quark is tuned to approximately its physical value, but the light quark masses differ between ensembles resulting in the different pion mass.

The charm quark is treated the same as the lighter quarks with a fully relativistic action as described in chapter 2. The valence charm quark anisotropy and mass is tuned so as to reproduce the physical η_c mass and relativistic dispersion relation with lattice discretised momenta $\vec{p} = \frac{2\pi}{L}\vec{n}$ [25]. This dispersion relation can be written as

$$(a_t E)^2 = (a_t M)^2 + \left(\frac{2\pi}{\xi L/a_s}\right)^2 n^2. \tag{4.1.1}$$

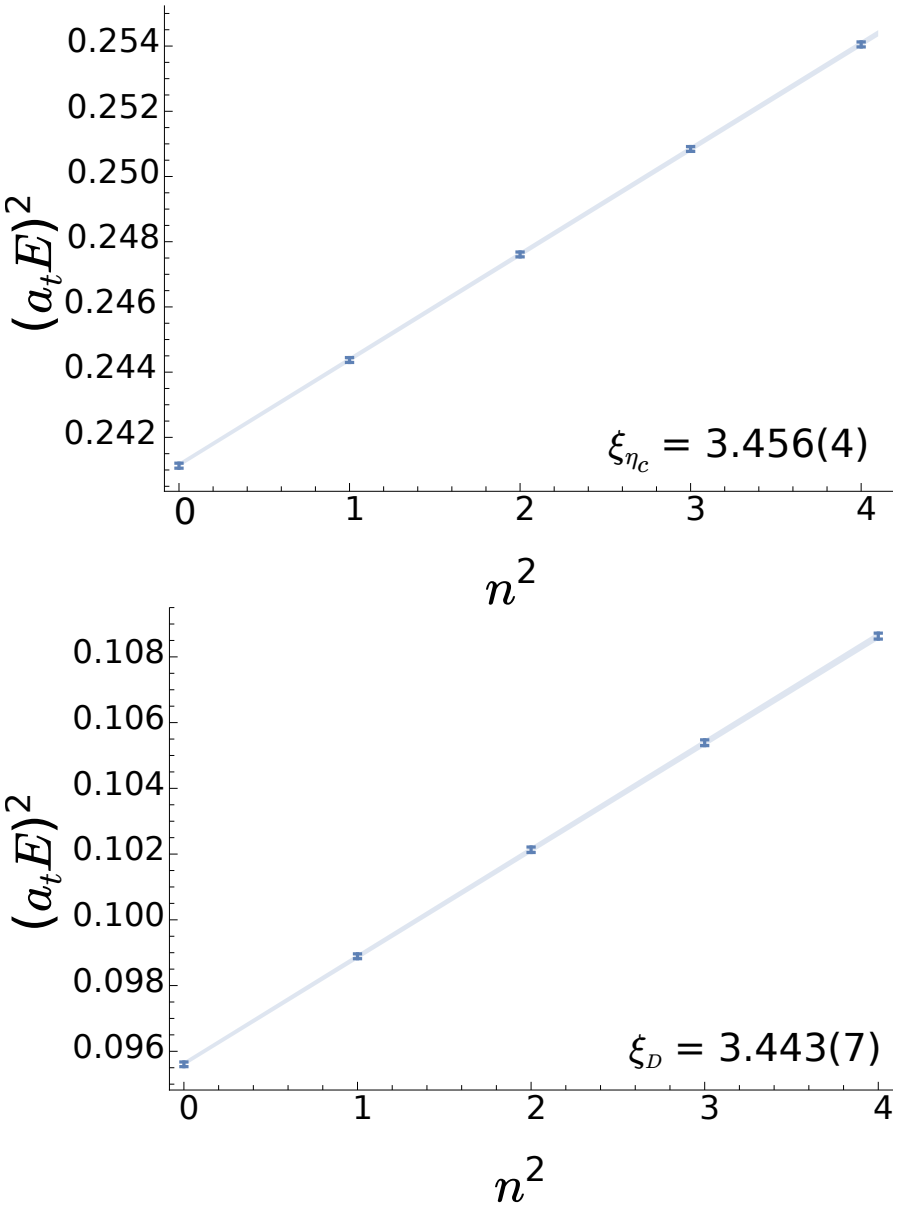

FIGURE 4.1: Points show the dependence of the η_c (upper panel) and D (lower panel) energy on momentum; error bars show the one sigma statistical uncertainty on either side of the mean. Lines are fits to the relativistic dispersion relation, Eq. 4.1.1, giving $\xi_{\eta_c} = 3.456(4)$ ($\chi^2/N_{\text{d.o.f}} = 1.08$) and $\xi_D = 3.443(7)$ ($\chi^2/N_{\text{d.o.f}} = 0.38$). Plot reproduced from [1].

This is shown in Figure 4.1 for the η_c and D meson for the $M_\pi \sim 236$ MeV ensemble. The anisotropy ξ was found from a linear fit to be $\xi_{\eta_c} = 3.456(4)$ for the η_c and $\xi_D = 3.443(7)$ for the D meson, both in reasonable agreement with the anisotropy found from the pion dispersion relation of $\xi_\pi = 3.453(6)$ [62].

Traditionally it has been difficult to treat heavy quarks relativistically on the lattice. Discretisation artifacts of $\mathcal{O}(am_q)$ become large when m_q is large. The

use of anisotropic lattice with finer temporal spacing circumvents this problem by reducing a_t without being too computationally expensive. This is especially salient in the case of mesons with non-zero momenta, as large discretisation artifacts will ruin the relativistic dispersion relation.

As the anisotropy has been tuned in the $c\bar{c}$ sector, the fact that ξ_D is in agreement with ξ_{η_c} is a sign that discretisation effects are small. This is expected as the four-momentum for a heavy meson will be predominantly in the temporal direction, at least for mesons moving with modest momenta, meaning the discretisation errors proportional to $a_t m$ will be small.

From the dispersion fit $M_{\eta_c} = 2945(17)$ MeV is found, to be compared to the experimental value of 2983.9(5) MeV [63]. From this, the systematic uncertainty from tuning the charm-quark mass can be estimated to be of order 1%. It is possible to include a p^4 term in the dispersion fit but this term is found to be negligible.

When extracting energies on the lattice all numbers are given in lattice units. To convert to physical units the scale wa set via $a_t^{-1} = M_\Omega^{\text{phys}}/(a_t M_\Omega)$ using the Ω baryon mass measured on this ensemble, $a_t M_\Omega = 0.2789(16)$ [62]. This leads to a conversion factor of $a_t^{-1} = 5997$ MeV. When quoting D_s and D meson energies in physical units half of M_{η_c} is subtracted to reduce any small error due to the tuning of the charm quark, leaving it negligible compared to other sources of error.

It must be noted that only single meson operators are included in the calculation and as such all of the excitations are treated as stable states. This is of course not correct above the relevant decay thresholds and so these spectra should only be taken as a guide to the pattern of resonances. In the light sector many scattering studies taking into account the unstable nature of these states have been performed to great success, [62, 64]. In the charm sector, there has been some work on this issue at the higher pion mass of 391 MeV [59]. This study paves the way for these to be extended towards the physical point on the newer lattices.

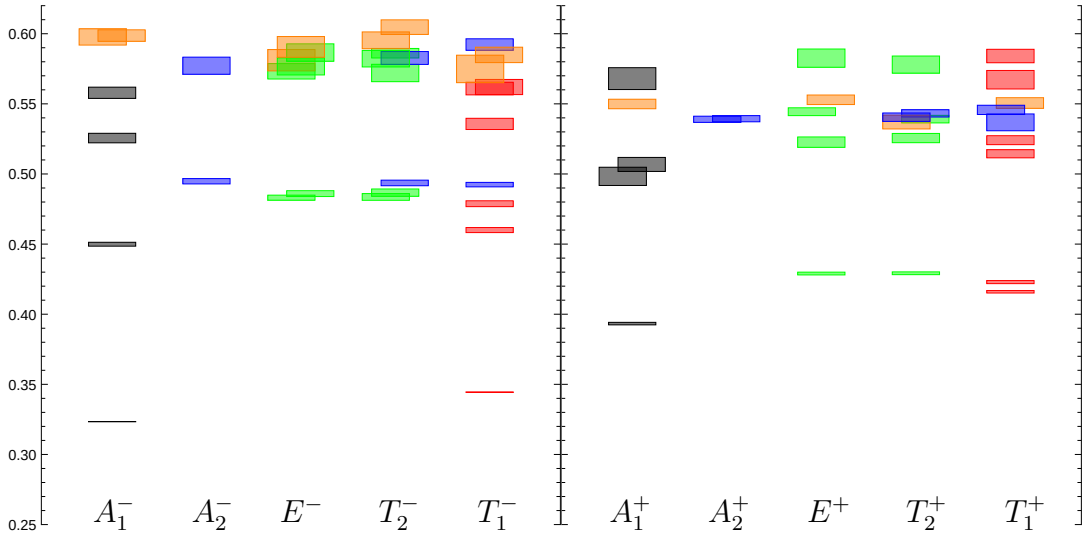

FIGURE 4.2: Extracted D_s meson spectrum in lattice units labelled by lattice irrep, Λ^P. The one sigma statistical uncertainty on either side of the mean is represented by the verticle height of each box while the different colours represent different continuum spins as discussed in the text.

4.2 D_s and D Spectrum

In Figure 4.2 the extracted spectrum of charm-strange excitations is shown in lattice units labelled by lattice irrep, Λ^P, for both positive and negative parity. As discussed earlier, mesons that are not eigenstates of the charge conjugation operator, such as the D_s meson ($c\bar{s}$), are grouped by their J^P quantum numbers as opposed to J^{PC}.

The energies are extracted from the principal correlators and spins are assigned according to the pattern of operators overlaps as detailed in the previous chapter. The various different colors in Figure 4.2 correspond to different continuum spins. States with $J = 0$ are grey, $J = 1$ are red, $J = 2$ are green, $J = 3$ are blue and $J = 4$ are orange.

The pattern of subduction into the different irreps for all $J \geq 2$, as described in Table 3.2 is evident. For example, for both positive and negative parity, in the A_2, T_2 and T_1 irreps the appearance of two almost degenerate blue states can be seen, as expected for a spin $J = 3$ state. As discussed before, it is checked that the states have similar operator overlap values, to ensure the matching across the different irreps is correct, shown in Figure 3.5. These degeneracies should become more exact as the continuum limit is approached. This overlap method is necessary as

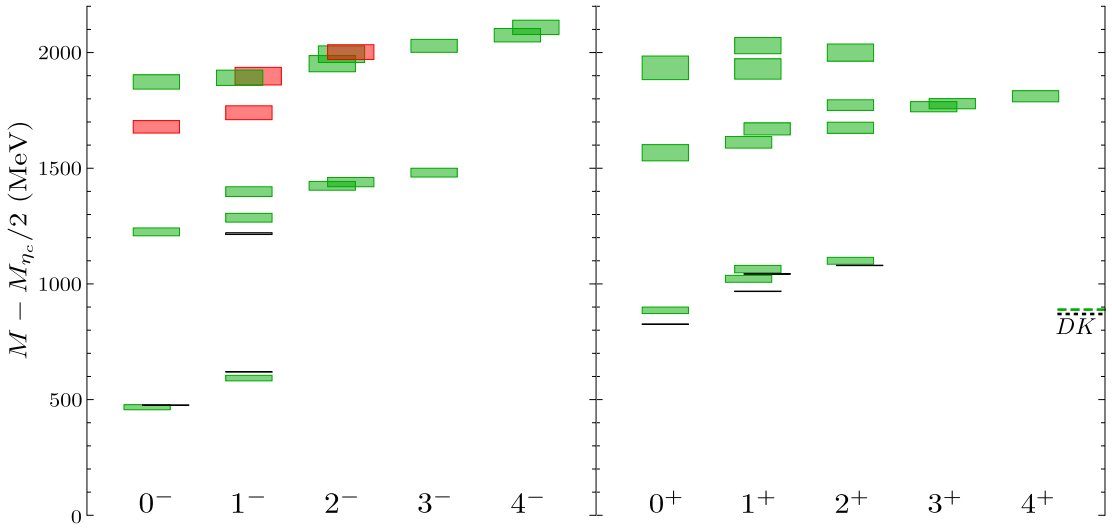

FIGURE 4.3: D_s meson spectrum labelled by J^P. Green and red boxes are the masses computed on the $M_\pi \sim 240$ MeV ensemble while black boxes are experimental masses of the neutral D_s mesons from the PDG summary tables [65]. The vertical size of the boxes indicates the one-sigma statistical (or experimental) uncertainty on either side of the mean. Red boxes show states identified as constituting the lightest hybrid supermultiplet, as described in the text. Dashed lines indicate the DK threshold using computed (coarse green dashing) and experimental (fine grey dashing) masses.

higher in the spectrum there is a large amount of overlapping states which would be impossible to untangle by eye alone.

Having identified the spin of the states, a joint fit to the principal correlators is performed across the various subduced irreps to extract a single energy for the spin identified spectrum. In Figure 4.3 the energies of the different excitations are shown in MeV for each value of $J \leq 4$. As was stated before, the energies are shown with half of the mass of the η_c subtracted. This is to reduce any systematic uncertainty which may arise due to the tuning of the charm quark mass.

The energy threshold for strong decays into DK has also been included in Figure 4.3. Above this line the various excitations should be thought of as resonances, however as was stated before, there are no operators that interpolate two-meson states in the operator basis for the GEVP, so these states are treated as stable. The energies of the experimentally observed states have also been added in black.

On inspection, among the states a clear pattern can be seen. They follow the simple quark model $n^{2S+1}L_J$ pattern. For instance the lowest two states with negative parity can be identified as an S wave doublet, with an excited doublet

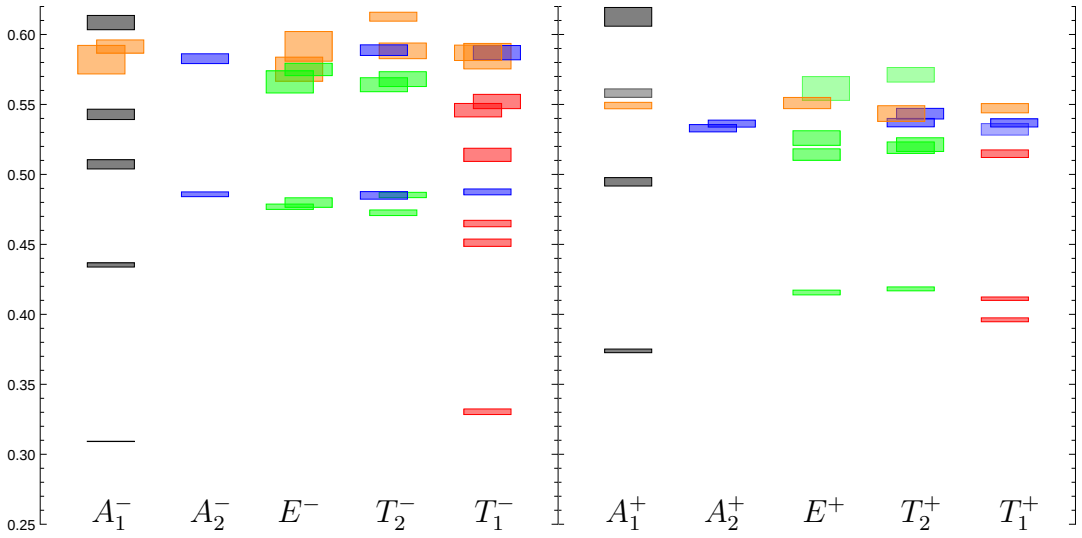

FIGURE 4.4: As Figure 4.2 but for the D spectrum.

about 700 MeV higher. In the positive parity sector the lowest four states are a P wave singlet and triplet. Above these excited S and P as well as D and F multiplets can be identified.

There are however some states which do not fit in with this pattern in the negative parity sector, labelled in red in Figure 4.3. These states have relatively strong overlap with operators that are proportional to the gluonic field strength tensor ie. states where the gluonic field has explicit excited degrees of freedom. It is proposed that these are members of the lightest hybrid supermultiplet, $[(0^-, 1^-, 2^-), 1^-]$. This is consistent with a 1^{+-} gluonic excitation coupled to an S wave meson.

In Figure 4.4 the spectrum computed on the same gauge configurations for the D meson is shown labelled by lattice irrep. The D meson correlators used two different time sources as opposed to one for the D_s meson. The spectrum can be seen to be qualitatively the same as the previous D_s meson spectrum shown in 4.2. The states of spin $J \geq 2$ are subduced across the appropriate irreps and the overall pattern is the same. Some higher lying states have not been included in the plot due to noisy principal correlators.

The spin identified D meson spectrum is shown in 4.5. This time two relevant decay thresholds are included, that of $D\pi$ and $D^*\pi$, using both experimental and calculated masses. A similar spin structure can be seen and S, P, D and F wave multiplets can be identifed. A hybrid multiplet in the negative parity sector is

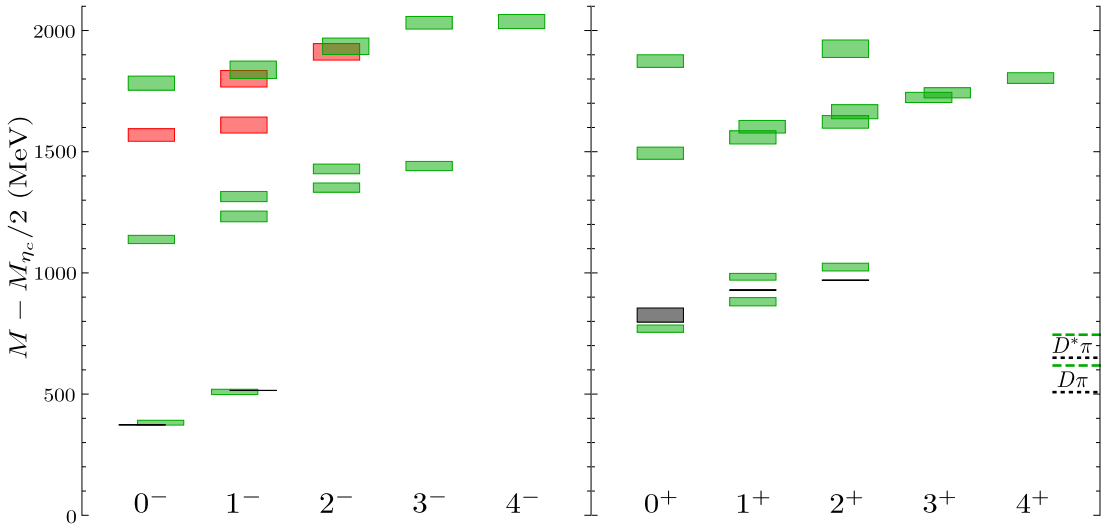

FIGURE 4.5: As Figure 4.2 but for the D meson spectrum. Dashed lines show the $D\pi$ and $D^*\pi$ thresholds using computed (coarse green dashing) and experimental (fine grey dashing) masses.

also identified in the same position in the spectrum as before. The energies shown in both the D_s and D spin plots are tabulated in Appendix B.

It is worth noting that the data agrees quite closely with the few available experimentally observed masses. The fact that the calculation was performed at an unphysically heavy pion mass may go some way towards explaining any discrepancies. There may also be discretisation effects due to the finite lattice spacing which lead to increased uncertainty.

4.3 Light Quark Mass Comparison

A comparison of the results discussed in the previous section with those shown in [48] was also performed. This comparison is made with energies extracted from a smaller volume and heavier pion mass, but it is noteworthy that the statistical precision is greater on the $M_\pi \sim 400$ lattices due to the number of time sources used in the construction of the correlation functions, as shown in Table 4.1.

Figures 4.6 and 4.7 show the comparison for the D_s and D mesons respectively. It can be seen that while there is some movement due to the difference in quark masses there is no major overall change in the pattern of states extracted between

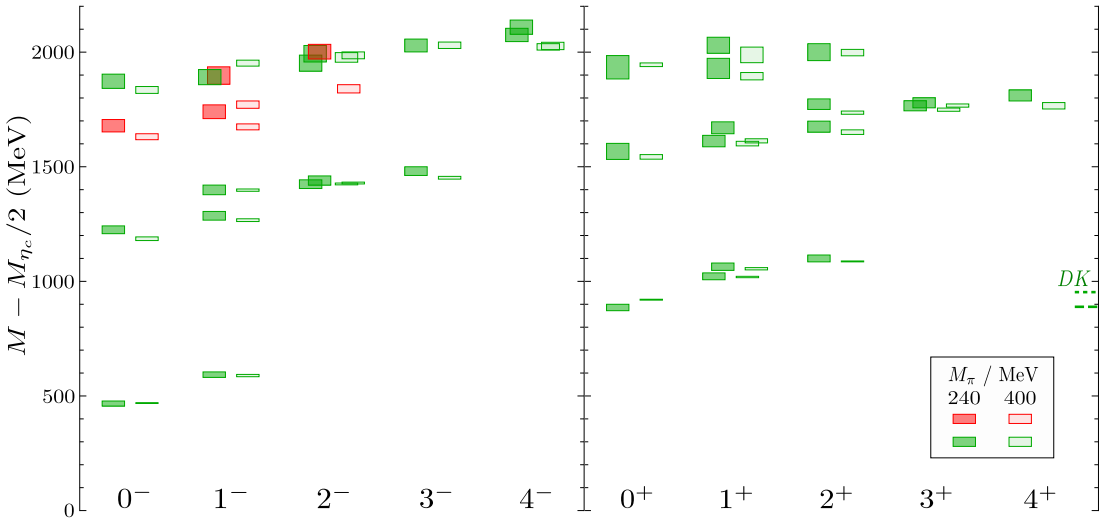

FIGURE 4.6: Comparison of the D_s meson spectrum for two different light quark masses labelled by J^P. Data from the $M_\pi \sim 240$ MeV lattices is shown on the left of each column with opaque boxes, while $M_\pi \sim 400$ MeV data is transparent. As before, hybrids are marked in red and the lowest relevant decay threshold is marked.

the two different ensembles. Particularly in the D spectrum there is a tendency for the energies to drop, an expected consequence of the lighter valence quark.

On the lower end of the spectrum some slight movement is seen in the lowest few excitations, the most apparent being in the 0^+ channel. This is where one would expect to find the enigmatic $D^*_{s0}(2317)$. The large movement might be explained by the close proximity to the decay thresholds. For the D_s meson this state has decreased just enough to stay below the DK threshold, as expected from experiment. In the case of the D meson, there is also an appreciable change seen in the 1^+ channel which would also be affected by the nearby decay threshold.

Interestingly the most obvious movement between the two is in the hybrid supermultiplet, particularly in the case of D_s which contains no light quark. It is found that the hybrid states become heavier as the quark mass is decreased, an observation shared with the charmonium spectrum, [1]. This is due to an increase in the splitting between the hybrids and the lower lying conventional mesonic states as M_π is increased. This general trend is less obvious in the case of the D meson due to the reduction in the mass of the light quark. It is worth noting that due to lying higher in the spectrum, these states are statistically less precise and the choice to disregard their unstable nature may have an effect.

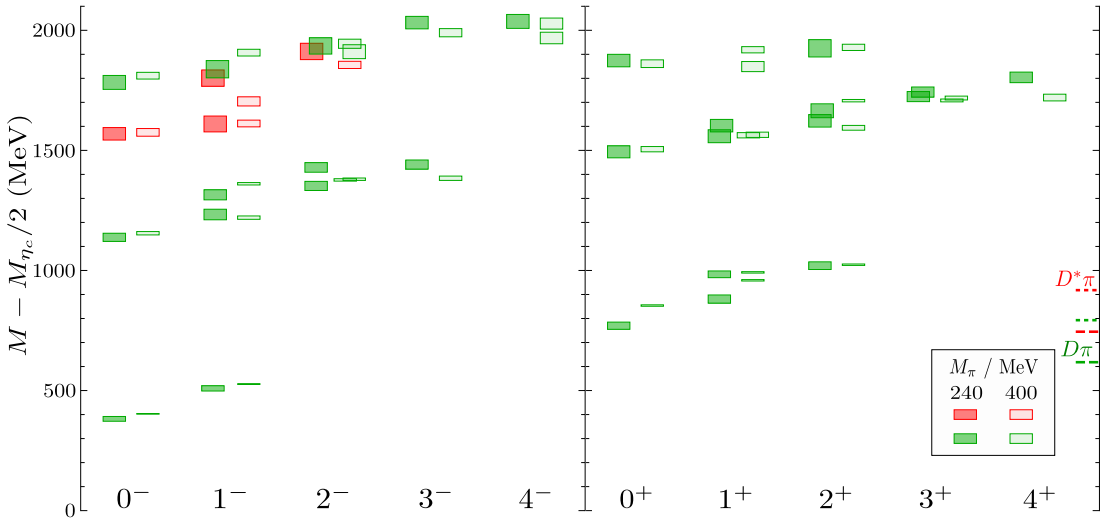

FIGURE 4.7: As Figure 4.6 but for the D meson spectrum labelled by J^P.

4.4 Spin-Singlet and Spin-Triplet state mixing

Due to the large difference in the value of the mass of a charm quark and the lighter quarks, any potential $SU(4)$ symmetry in our system is badly broken. This leads to the fact that charm-light and charm-strange mesons are not eigenstates of charge conjugation or any potential generalisation. There is therefore some mixing of singlet and triplet states when $J = L$, ie. the quark model singlet ($^1L_{J=L}$) and triplet ($^3L_{J=L}$) states can mix. An analysis of this mixing can help quantify this flavour symmetry breaking.

Assume energy independent mixing and two states written in terms of the singlet and triplet states,

$$\begin{aligned} |A\rangle &= +\cos\theta|^1L_{J=L}\rangle + \sin\theta|^3L_{J=L}\rangle, \\ |B\rangle &= -\sin\theta|^1L_{J=L}\rangle + \cos\theta|^3L_{J=L}\rangle. \end{aligned} \tag{4.4.1}$$

B is chosen to be the heavier of the two states. Certain operators, using the naming convention shown in Table 3.1, such as $\left[(\rho - \rho_2) \times D_L^{[L]}\right]_{J=L}$ only overlap onto $^3L_{J=L}$ states, where as $\left[\{\pi, \pi_2\} \times D_L^{[L]}\right]_{J=L}$ only overlap onto $^1L_{J=L}$ states. Taking ratios of the operator overlap combinations allows for the extraction of this mixing angle for a range of states, as shown in Table 4.2. Also shown are

	J^P	M_π / MeV	$\|\theta\|/^\circ$ $\sim (\rho - \rho_2)$	$\sim \pi$	$\sim \pi_2$	Heavy-quark limit
c-s	1^+	240	60.2(0.4)	63.1(0.7)	65.4(0.7)	54.7 or 35.3
		400	60.9(0.6)	64.9(0.2)	66.4(0.4)	
	2^-	240	56.3(0.9)	60.7(0.8)	63.5(0.9)	50.8 or 39.2
		400	64.9(1.9)	68.7(2.0)	70.9(1.8)	
	1^- (hybrid)	240	58.9(1.0)	66.2(1.9)	65(2.0)	
		400	59.9(1.7)	67.9(0.9)	67.3(0.9)	
c-l	1^+	240	52.7(0.9)	61.4(0.4)	67.1(1.0)	54.7 or 35.3
		400	60.1(0.4)	62.6(0.2)	65.4(0.2)	
	2^-	240	50.4(0.7)	57.5(0.8)	61.4(0.9)	50.8 or 39.2
		400*	63.3(2.2)	67.8(3.7)	71.1(3.9)	
	1^- (hybrid)	240	57.8(1.1)	71.4(2.2)	69.9(2.5)	
		400	59.7(1.1)	68.4(0.8)	67.4(0.9)	

TABLE 4.2: Absolute value of the mixing angles for the lightest pairs of 1^+, 2^- and hybrid 1^- states in the charm-strange (c-s) and charm-light (c-l) sectors on the two ensembles. The mixing angles expected in the heavy-quark limit are also shown [66]. In the $M_\pi \sim 400$ MeV case highlighted by the *, the angle given in reference [48] from 90° so that the mass ordering of the states is consistent between the two ensembles. Reproduced from [1].

the values expected in the heavy quark limit where $m_c \gg m_{u,d,s}$ [66]. There the mixing angle for the lightest pairs of P-wave ($J^P = 1^+$), D-wave ($J^P = 2^-$) and $J^P = 1^-$ hybrid states are shown as well as a comparison with the angles found in [48]. The overall sign of the angle is unobservable in the calculation so we show only the absolute value.

By using the three different operators to determine the variation between mixing angles an estimate of the size of the systematic uncertainties can be found as discussed in reference [48]. The 1^+ mixing angle from the $\rho - \rho_2$ operator in the charm-light sector is closer to the heavy-quark limit value on the $M_\pi \sim 240$ MeV ensemble, but the analogous angle in the charm-strange sector does not differ significantly between the ensembles. For both charm-light and charm-strange mesons, the 2^- mixing angle is closer to the heavy-quark limit value for the lighter pion mass whereas the 1^- hybrid mixing angle shows no significant difference between the two ensembles.

We see a larger difference between the angles for the charm light and charm strange mesons on the 240 MeV lattice as expected. In the previous analysis the light quarks were closer to the strange quark mass and we would expect similar θ values

as we approach the $SU(3)$ limit. Even though the charm quark is much heavier than the light and strange quarks, it is not heavy enough to be considered in the heavy-quark limit. The extracted mixing angles for both ensembles can be seen to lie somewhere between the heavy quark limit values and the flavour symmetry limit (0° or 90°), as expected.

4.5 Summary of Results

D_s and D meson spectra have been shown, calculated on $32^3 \times 256$ lattices with a pion mass of approimately 236 MeV. A matrix of correlation funtions between a wide range of operators with spin $J \leq 4$ was calculated using distillation and diagonalised using the generalised eigenvalue problem method. The energies of states were extracted from the principal correlators and the use of appropriately chosen operators allowed for the reliable assigning of continuum spins to each state extracted in the spectrum. It is clear that this robust method allows for the accurate extraction of a plethora of states above threshold, including some potential hybrid states.

The pattern of both D_s and D meson states follows the traditional potential model pattern $n^{2S+1}L_J$, with the exception of the potential hybrid states which are not expected from these simple models. A hybrid supermultiplet was identified, consistent with an S wave quark-anitquark excitation coupled to an 1^{+-} gluonic excitation. The overall pattern of states including these hybrids is found to be in close allignment with previous studies in the light and charmed meson sectors, [24, 48, 67, 68].

A comparison with previous results from lattices with a pion mass of approximately 391 MeV discussed in reference [48] showed little qualitative change in the overall spectrum, confirming the validity of the method. Small quanitative differences can be accounted for with the lower pion mass. The hybrid mesons appear to show a mild increase in mass however the overall pattern is the same.

While not containing operators that look like two meson states, necessary for the correct treatment of states above threshold, this work provides valuable insight for future studies in the charmed meson sector. This will allow for previous studies investigating scattering in charm-light and charm-strange mesons, such as [59], to advance closer to the physical point.

Chapter 5

Radiative Transitions in Charmonium

As discussed in previous chapters, charmonium spectroscopy allows for the precision testing of the theory of the strong interactions. Accurate lattice calculations of meson spectra, which can be compared to recent experimental results, go a long way towards investigating the theory of QCD, as well as potentially predicting states which have yet to be discovered. However a complete picture of the spectrum will necessitate more than just the calculation of the various allowed energy levels. Radiative transition matrix elements describing decays involving the emission of a photon can also be calculated on the lattice and provide an opportunity to investigate other properties of the spectrum. These calculations give access to photocouplings for the various states as well as providing some insight into the size and internal structure of these bound states, information unavailable from simple spectrum calculations. Knowledge of these couplings is particularly relevant in the charmonium sector as the low lying states in the spectrum lie below the energy level needed to create two lighter charmed mesons, the $D\bar{D}$ threshold. These states are unable to decay via an OZI allowed strong decay and so have relatively large branching fractions to radiative decays, many of which have been measured experimentally [14, 63]. In addition, knowledge of the photocouplings for charmonium is of great interest to many experiments where the photo-production of charm mesons is relevant, such as ALICE [69], Glue-X and the proposed PANDA experiment [17].

In this chapter the innovative technology for extracting radiative transition form-factors from lattice three-point correlation functions will be discussed. This was first introduced in the light sector in reference [70]. To extract these form-factors there will be a need to compute correlation functions between states of various momenta, necessitating the introduction of helicity states, or states with well defined helicity. As before with the two point functions, a simple spectral decomposition shows that all states with the same quantum numbers will be present in the correlation function. The idea of an improved or optimised operator which interpolates a particular state with greater accuracy will be introduced. This will allow for the eventual goal of investigating decays involving the higher lying, and traditionally more noisy, excited states in the spectrum. This is the first investigation of radiative transitions in charmonium using this technology on lattices with $N_f = 2 + 1$ dynamical quarks. Preliminary discussion of this work can be found in [71] as well as earlier work in charmonium on quenched lattices in [72, 73].

5.1 Radiative Transitions on the Lattice

The continuum object of interest is the electro-magnetic vector current j^μ matrix element between, a hadron h of spin J with helicity projection λ along $\vec{p}$ and a second hadron h' with $J', \lambda', \vec{p}'$, namely

$$\langle h'_{J'}(\lambda', \vec{p}')|j^\mu|h_J(\lambda, \vec{p})\rangle. \tag{5.1.1}$$

Here $j^\mu = \frac{2}{3}\bar{c}\gamma^\mu c$ is the standard vector current coupling to a charm quark, where $\frac{2}{3}$ is the charge of the charm quark in units of e. To leading order in α_{em} these matrix elements encode the coupling of hadrons to the photon and can be related to the helicity amplitude for the process $\gamma h \to h'$ simply by contracting with a photon polarisation vector,

$$\mathcal{M}(\gamma(\lambda_\gamma, \vec{q})h_J(\lambda, \vec{p}) \to h'_{J'}(\lambda', \vec{p}')) = \epsilon_\mu(\lambda_\gamma, \vec{q})\langle h'_{J'}(\lambda', \vec{p}')|j^\mu|h_J(\lambda, \vec{p})\rangle. \tag{5.1.2}$$

It is possible to write these matrix elements as a sum over various form factors $F(Q^2)$ multiplying kinematic Lorentz factors K_i as

$$\langle h'_{J'}(\lambda', \vec{p}')|j^\mu|h_J(\lambda, \vec{p})\rangle = \sum_i K_i^\mu[h'_{J'}(\lambda', \vec{p}'); h_J(\lambda, \vec{p})]F_i(Q^2). \tag{5.1.3}$$

Q^2 is the photon virtuality, which measures the degree to which the photon is off shell and is given as $Q^2 = -q^2 = |\vec{p}' - \vec{p}|^2 - (E_{h'}(\vec{p}') - E_h(\vec{p}))^2$. It is these unknown form factors $F_i(Q^2)$ that are of interest in the calculation of decay rates. If the initial and final states are the same when calculating matrix elements of the form of Eqn. 5.1.1, one extracts what are called radiative or charge form-factors. If the states are different then transition form-factors are extracted.

The general procedure for decomposing the matrix elements is to write down all possible kinematic factors consistent with Lorentz invariance from the meson four-momenta and any necessary polarisation tensors. Constraints due to the conservation of the current and parity invariance can then be used to constrain the form-factor decompositon. The general procedure is decribed in detail in reference [72]. As an example, take the simplest case of interest, a transition from a pseudoscalar state , P, with momentum p to itself with momentum p'. This can be expressed in terms of two form-factors multiplying two kinematic factors,

$$\langle P(p')|j^\mu|P(p)\rangle = (p' + p)^\mu F_1(Q^2) + (p' - p)^\mu F_2(Q^2). \tag{5.1.4}$$

However, due to current conservation there is the constraint that

$$\langle P(p')|\partial_\mu j^\mu|P(p)\rangle = (p' - p) \cdot \langle P(p')|j^\mu|P(p)\rangle = 0 \tag{5.1.5}$$

This constraint eliminates the need for $F_2(Q^2)$, and results in one single form-factor for this decomposition. In the case of charmonium this is the η_c state and the decomposition can be written as

$$\langle \eta_c(p')|j^\mu|\eta_c(p)\rangle = (p + p')^\mu F_{\eta_c}(Q^2). \tag{5.1.6}$$

A slightly more complicated case is a transition between a vector particle, such as the J/ψ, and the pseudoscalar η_c. In this case there are multiple possible Lorentz covariant kinematic factors allowed, however the constraints again eliminate all but one, leaving the decomposition as

$$\langle \eta_c(p')|j^\mu|J/\psi(\lambda,p)\rangle = \epsilon^{\mu\nu\rho\sigma}p'_\nu p_\rho \epsilon_\sigma(\lambda,p)\frac{2}{m_{\eta_c}+m_{J/\psi}}F_{J/\psi\eta_c}(Q^2). \tag{5.1.7}$$

Here $\epsilon_\sigma(\lambda,p)$ is the polarisation vector for the J/ψ. This decomposition will allow for the extraction of the form-factor needed to calculate the decay rate for $J/\psi \to \eta_c\gamma$. Similarly, the transitions from a vector state to a scalar can be parameterised using two form factors, an electromagnetic form-factor $E(Q^2)$ and a transverse form-factor $C_1(Q^2)$,

$$\begin{aligned}\langle \chi_{c0}(\vec{p}')|j^\mu|J/\psi(\lambda,\vec{p})\rangle = \;& \Omega^{-1}(Q^2)\,(\,E_1(Q^2)[\Omega(Q^2)\epsilon^\mu(\lambda,\vec{p}) \\ & - \epsilon(\lambda,\vec{p})\cdot p'(p^\mu p\cdot p' - m_{J/\psi}p^{\mu\prime})] \\ & + \frac{C_1(Q^2)}{\sqrt{q^2}}m_{J/\psi}\epsilon(\lambda,\vec{p})\cdot\vec{p}'[\vec{p}\cdot\vec{p}'(\vec{p}+\vec{p}')^\mu \\ & - m^2_{\chi c0}p^\mu - m^2_{J/\psi}p^{\mu\prime}]\big)\,.\end{aligned} \tag{5.1.8}$$

Finally a vector to vector transition has three form-factors, which can be written as

$$\begin{aligned}\langle J/\psi(\lambda',\vec{p}')|j^\mu|J/\psi(\lambda,\vec{p})\rangle = & -[(p+p')^\mu\epsilon^*(\lambda',\vec{p}')\cdot\epsilon(\lambda,\vec{p})]G_1(Q^2) \\ & + [\epsilon^\mu(\lambda,\vec{p})\epsilon^*(\lambda',\vec{p}')\cdot p + \epsilon^{\mu*}(\lambda',\vec{p}')\epsilon(\lambda,\vec{p})\cdot p']G_2(Q^2) \\ & - [(p+p')^\mu\epsilon^*(\lambda',\vec{p}')\cdot p\epsilon(\lambda,\vec{p})\cdot p'\frac{1}{2m^2}]G_3(Q^2).\end{aligned} \tag{5.1.9}$$

In principle states in the charmonium spectrum have no radiative form factors. This is because the photon has a charge conjugation quantum number $C=-1$ and charmonium states are eigenstates of charge conjugation. A radiative transition can therefore only occur between states of different C. This can be explained by

the photon coupling equally to both the quark and the anti-quark in the meson. However in a lattice calculation, by coupling the photon to only the quark, transitions between states of equal C can be investigated. These unphysical transitions can not be compared to experiment but can be used to shed some light on the inner structure of the meson such as giving an estimate for the charge radius.

To investigate these transitions on the lattice one is interested in calculating the three point function

$$C^{\mu}_{ij}(\Delta t, t) = \langle 0|\mathbb{O}_i(\Delta t) j^{\mu}(t) \mathbb{O}^{\dagger}_j(0)|0\rangle. \tag{5.1.10}$$

from a large basis of lattice subduced *helicity operators* $\mathbb{O}_i, \mathbb{O}^{\dagger}_j$ with a local vector current insertion placed at time t. As mentioned in Chapter 2, Wick's theorem says that evaluating the correlation function amounts to evaluating products of quark propagators on the lattice. There are three different classes that these products, or Wick contractions, fall into, which are shown in Figure 5.1. However the first class of diagram, the connected part of the correlator, it solely necessary for this calculation. The second class is highly OZI suppressed and so should have little influence. The third class of contraction, with a vacuum loop should also be negligible. In the case of a charge form-factor this will be zero due to charge-conjugation invariance. In addition the large mass of the charm quark makes the occurance of these vacuum loops small and so is not included in the computation. The correlators are computed using the distillation method as described in Chapter 3, with one alteration. As the quark fields in the vector current should be the unsmeared fields of the action, perambulators involving a current insertion are replaced with *generalised perambulators* which are unsmeared at one end, [70].

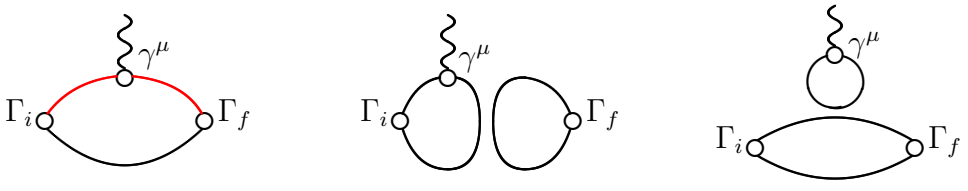

FIGURE 5.1: Schematic of the possible Wick contractions for the three point function 5.1.10. Generalised perabulators are highlighted in red.

As before in the case of a two point function it is possible to expand Eqn. 5.1.10 over a complete set of states of the lattice Hamiltonian. From this spectral decomposition it is evident that the correlator contains contributions from all of the states having the same quantum numbers as the interpolating operators,

$$C_{ij}^{\mu}(\Delta t, t) = \sum_{m,n} \frac{1}{2E_m} \frac{1}{2E_n} e^{-E_m(\Delta t - t)} e^{-E_n t} \langle 0|\mathbb{O}_i(0)|m\rangle\langle m|j^{\mu}(0)|n\rangle\langle n|\mathbb{O}_j^{\dagger}(0)|0\rangle. \quad (5.1.11)$$

This correlator now contains, unlike in Eqn. 3.1.2, the required matrix element, $\langle m|j^{\mu}(0)|n\rangle$, between state m and n. As before, taking large Δt will ensure that all higher lying excited states will go to zero more quickly than the ground state due to the exponential suppression and so one may extract the matrix element between the lowest energy states of the theory. However in practice on the lattice it is not possible to take very large t separations as it has been shown to increase the amount of noise in the correlator. In addition, if the goal is to analyse higher excited states in the spectrum, t must be small enough so that the signal for the excited state has not decayed to zero. For this reason, methods that allow the extraction of information from the correlation function at earlier times are crucial.

5.2 Helicity Operator Construction

When attempting to calculate radiative form-factors $F(Q^2)$, in many cases the physical point, where $Q^2 \to 0$, is inaccessible to lattice calculations due to the discretised momenta available. The value of the form-factor at $Q^2 = 0$ is necessary to make contact with experiment so one must interpolate between spacelike and timelike values of Q^2. It is therefore important to have as many values of Q^2 as possible to ensure a reliable fit.

To access the form-factor for a wide range of Q^2 one must calculate three point functions between interpolating operators having a wide range of different momenta. However creating operators of definite momenta is not as straight forward as just Lorentz boosting previously constructed at-rest operators. As described in Chapter 3, each operator in the basis is formed from appropriate combinations of Dirac gamma matrices and lattice derivatives. These operators are then subduced

Lattice Momentum	Little Group	Irreps(Λ or Λ^p)
$(0,0,0)$	O_h^D	$A_1^{\pm}$ $A_2^{\pm}$ $E^{\pm}$ $T_1^{\pm}$ $T_2^{\pm}$
$(0,0,n)$	Dic_4	A_1 A_2 B_1 B_2 E_2
$(0,n,n)$	Dic_2	A_1 A_2 B_1 B_2
(n,n,n)	Dic_3	A_1 A_2 E_2

TABLE 5.1: Allowed lattice momenta on a cubic lattice in a finite cubic box, along with the corresponding little groups for relevant momenta. Lattice momenta are given in units of $2\pi/(L_s a_s)$ where $n \in Z$ is a non-zero integer. The A and B irreps have dimension one, E is dimension two and T is dimension three. Dic_n is the dicyclic group of order $4n$.

into the proper lattice irrep to take into account the reduced rotational symmetry after discretising on a lattice, as shown in Eqn. 3.3.1.

In the case of an operator at non-zero momentum, the symmetry group of the lattice is further reduced. The relevant group is now the *little group* of lattice rotations which keep the momentum invariant. The distribution of the various possible lattice momenta into lattice irreps is shown in Table 5.1. As before we define an operator with spin J, spin z component M and spatial momentum $\vec{p}$ as

$$O^{J,M}(\vec{p}) \sim \sum_{m_1,m_2,m_3,\ldots} CGs(m_1,m_2,m_3,\ldots) \sum_{\vec{x}} e^{i\vec{p}\cdot\vec{x}} \bar{\psi}(\vec{x},t) \Gamma_{m_1} \overleftrightarrow{D}_{m_2} \overleftrightarrow{D}_{m_3} \ldots \psi(\vec{x},t) \tag{5.2.1}$$

up to a constant, where D are the forward-backward lattice covariant derivatives defined in Eqn. 3.2.2. At $\vec{p} = 0$ this operator will have definite spin J and z-projection M, however when $\vec{p} \neq 0$, M is no longer a good quantum number, unless the momentum is purely in the z direction. Instead it is more useful to use operators with definite helicity λ, or the projection of the spin component in the direction of momentum. These *helicity operators* can be formed using the appropriate Wigner-D matrix $\mathcal{D}^{(J)*}_{M\lambda}(R)$, [74].

$$\mathbb{O}^{J,\lambda}(\vec{p}) = \sum_M \mathcal{D}^{(J)*}_{M\lambda}(R) \mathcal{O}^{J,M}(\vec{p}). \tag{5.2.2}$$

Here, R is the rotation that takes $(0,0,|\vec{p}|)$ to $\vec{p}$. In the continuum, there are an infinite number of rotations that will achieve this, however on the finite volume lattice the correct choice of R is important. Due to the reduced symmetry, an

Little group	$\vec{p}_{ref}$	ϕ	θ	ψ
Dic_4	$(0,0,n)$	0	0	0
Dic_2	$(0,n,n)$	$\pi/2$	$\pi/4$	$-\pi/2$
Dic_3	(n,n,n)	$\pi/4$	$\cos^{-1}(1/\sqrt{3})$	0

TABLE 5.2: Rotations, R_{ref}, used as described in the text, for rotation $\hat{R}_{\phi,\theta,\psi} = e^{-i\phi\hat{J}_z}e^{-i\theta\hat{J}_y}e^{-i\psi\hat{J}_z}$ that takes $(0,0,|\vec{p}|)$ to $\vec{p}_{ref}$ [74].

incorrect choice of R can lead to inconsistencies when dealing with different momenta and different irreps may end up mixing. The rotation is broken up into two separate steps, $R = R_{lat}R_{ref}$. First, R_{ref} rotates from $(0,0,|\vec{p}|)$ to a specially chosen reference momenta $\vec{p}_{ref}$. This rotation is in general not an allowed lattice rotation. This ensures consistency when dealing with different momenta in the star of $\vec{p}$, ie. momenta equivalent up to a simple lattice rotation. Each type of momenta shown in Table 5.1 belongs to a different star. The allowed lattice rotation R_{lat} then rotates from $\vec{p}_{ref}$ to $\vec{p}$. Table 5.2 shows the angles used to rotate to the reference momenta $\vec{p}_{ref}$. In this work it is beneficial to work with operators whose momenta aligns with one of the reference momenta as in this case the rotation R simplfies to just R_{ref}.

As for the zero-momentum case, due to the reduced symmetry of the discretised lattice, operators must be subduced into the relevant lattice irreps so as to have well defined behaviour under a transformation. It is then possible to form a *subduced helicity operator*, in lattice irrep Λ as

$$\mathbb{O}^{[J,P,|\lambda|]}_{\Lambda,\mu}(\vec{p}) = \sum_{\hat{\lambda}=\pm|\lambda|} S^{\tilde{\eta},\hat{\lambda}}_{\Lambda,\mu}\mathbb{O}^{JP,\hat{\lambda}}(\vec{p}). \tag{5.2.3}$$

Here $\tilde{\eta} \equiv P(-1)^J$ where J and P are the spin and parity of the operator and μ is the row of the irrep Λ. These subduced operators are formed as orthogonal combinations of the two helicities $+|\lambda|$ and $-|\lambda|$. Table 5.3 shows the appropriate subduction coefficients needed for construction of the subduced operators used in this work. There are other procedures one could follow to create lattice helicity operators, for example projecting directly from the continuum J_z operators into little group irreps, however the method employed here allows for the relatively simple post hoc identification of the continuum quantum numbers of the identified spectrum of states. A full discussion on the construction of these states can be found in reference [74].

Group	$\lvert\lambda\rvert^{\tilde{\eta}}$	$\Lambda(\mu)$	$S^{\tilde{\eta},\lambda}_{\Lambda,\mu}$
Dic_4	0^+	$A_1(1)$	1
$(0,0,n)$	0^-	$A_2(1)$	1
	1	$E_2(12)$	$(\delta_{s,+} \pm \tilde{\eta}\delta_{s,-})/\sqrt{2}$
	2	$B_1(1)$	$(\delta_{s,+} + \tilde{\eta}\delta_{s,-})/\sqrt{2}$
	2	$B_2(1)$	$(\delta_{s,+} - \tilde{\eta}\delta_{s,-})/\sqrt{2}$
	3	$E_2(12)$	$(\pm\delta_{s,+} + \tilde{\eta}\delta_{s,-})/\sqrt{2}$
	4	$A_1(1)$	$(\delta_{s,+} + \tilde{\eta}\delta_{s,-})/\sqrt{2}$
	4	$A_2(1)$	$(\delta_{s,+} - \tilde{\eta}\delta_{s,-})/\sqrt{2}$
Dic_2	0^+	$A_1(1)$	1
$(0,n,n)$	0^-	$A_2(1)$	1
	1	$B_1(1)$	$(\delta_{s,+} + \tilde{\eta}\delta_{s,-})/\sqrt{2}$
	1	$B_2(1)$	$(\delta_{s,+} - \tilde{\eta}\delta_{s,-})/\sqrt{2}$
	2	$A_1(1)$	$(\delta_{s,+} + \tilde{\eta}\delta_{s,-})/\sqrt{2}$
	2	$A_2(1)$	$(\delta_{s,+} - \tilde{\eta}\delta_{s,-})/\sqrt{2}$
	3	$B_1(1)$	$(\delta_{s,+} + \tilde{\eta}\delta_{s,-})/\sqrt{2}$
	3	$B_2(1)$	$(\delta_{s,+} - \tilde{\eta}\delta_{s,-})/\sqrt{2}$
	4	$A_1(1)$	$(\delta_{s,+} + \tilde{\eta}\delta_{s,-})/\sqrt{2}$
	4	$A_2(1)$	$(\delta_{s,+} - \tilde{\eta}\delta_{s,-})/\sqrt{2}$
Dic_3	0^+	$A_1(1)$	1
(n,n,n)	0^-	$A_2(1)$	1
	1	$E_2(12)$	$(\delta_{s,+} \pm \tilde{\eta}\delta_{s,-})/\sqrt{2}$
	2	$E_2(12)$	$(\pm\delta_{s,+} - \tilde{\eta}\delta_{s,-})/\sqrt{2}$
	3	$A_1(1)$	$(\delta_{s,+} - \tilde{\eta}\delta_{s,-})/\sqrt{2}$
	3	$A_2(1)$	$(\delta_{s,+} + \tilde{\eta}\delta_{s,-})/\sqrt{2}$
	4	$E_2(12)$	$(\delta_{s,+} \mp \tilde{\eta}\delta_{s,-})/\sqrt{2}$

TABLE 5.3: Subduction coefficients, $S^{\tilde{\eta},\lambda}_{\Lambda,\mu}$, for $|\lambda| \leq 4$ with $s \equiv \mathrm{sign}(\lambda)$, reproduced from [74].

5.3 Optimised Operators and Extracting Form-Factors

Excited state contamination of three point correlation functions is a well known and significant problem especially in precision calculations of quantities, such as the muon anomalous magnetic moment $g-2$. To ameliorate this issue of contamination from higher lying states in the three point correlation funtions the three point functions were calculated using *improved operators*, Ω_n. These operators are chosen as a linear combination of the standard operators in the basis so as to have maximum overlap with a particular state in the spectrum.

In general, any one interpolating operator has some overlap onto all states in the spectrum with the same quantum numbers, and will create a tower of states as can be seen by inserting a complete basis of states,

$$\mathbb{O}_i^\dagger|0\rangle = \sum_n \frac{1}{2E_n}|n\rangle\langle n|\mathbb{O}_i^\dagger|0\rangle. \tag{5.3.1}$$

However as discussed in Chapter 3, it is reasonable to assume that some linear combination of the operators in the basis will overlap more strongly onto the desired state.

$$\Omega_n^\dagger = \sum_i w_i^{(n)}\mathbb{O}_i^\dagger \sim \frac{1}{2E_n}|n\rangle\langle n|\mathbb{O}_i^\dagger|0\rangle + ... \tag{5.3.2}$$

It can be shown that the best estimates for the weights w_i for this optimal linear combination are given by solving the GEVP as described in the previous chapters [22]. Using the generalised eigenvalues $v_i^{(n)}$ extracted from the two point correlation function analysis, one can form these improved operators by dotting the eigenvector $v_i^{(n)}$ into the basis of operators $\mathbb{O}_i$,

$$\Omega_n^\dagger(\vec{p}) = \sqrt{2E_n}e^{-E_n t_0/2}\sum_i v_i^{(n)}\mathbb{O}_i^\dagger(\vec{p}). \tag{5.3.3}$$

As an example of how this optimisation procedure affects the correlation function, Figure 5.2 shows the principal correlator for the lowest state in the charmonium

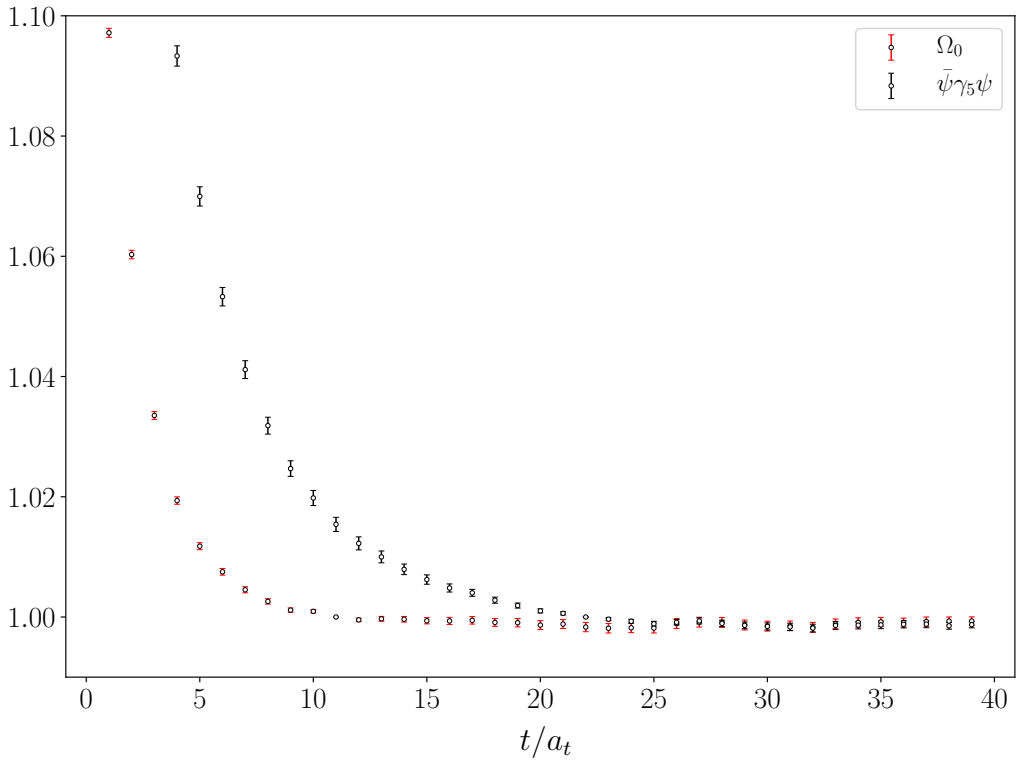

FIGURE 5.2: $\lambda e^{M_{\eta_c}(t-t_0)}$ plotted for the η_c at rest using the optimised η_c-like operator (shown in red) and the standard $\bar{\psi}\gamma_5\psi$ operator (in black). The earlier plateau in the case of optimised operator can be seen clearly.

spectrum, the η_c, calculated with a simple pseudo-scalar γ_5 operator vs an optimised η_c operator. It is clear that the optimised operator plateaus a significant number of timeslices earlier, allowing for the efficent extraction of the state's energy. This is of particular benefit in the case of a three point function where the plateau must be approached from both sides.

Figure 5.3 shows a similar plot but for the first excited state in the T_1^{--} irrep, the ψ'. Shown in black is the principal correlator for the state using two operators, a γ_i and $\gamma_i\gamma_0$ operator, as it is necessary to use at least two operators to extract a state which is orthogonal to the ground state. Shown in red is the principal correlator for the optimised operator formed from a basis of 26 operators. It can be seen that the optimised operator again plateaus at earlier t allowing for a more accurate energy extraction, before the signal degrades into noise.

Once a set of optimised operators has been formed, the three point function shown in Eqn. 5.1.11 can be rewritten more simply. Using operators Ω_m, Ω_n which project onto state m and n, and a normalisation where $\langle n|\Omega_n^\dagger|0\rangle = 2E_n$, the equation becomes

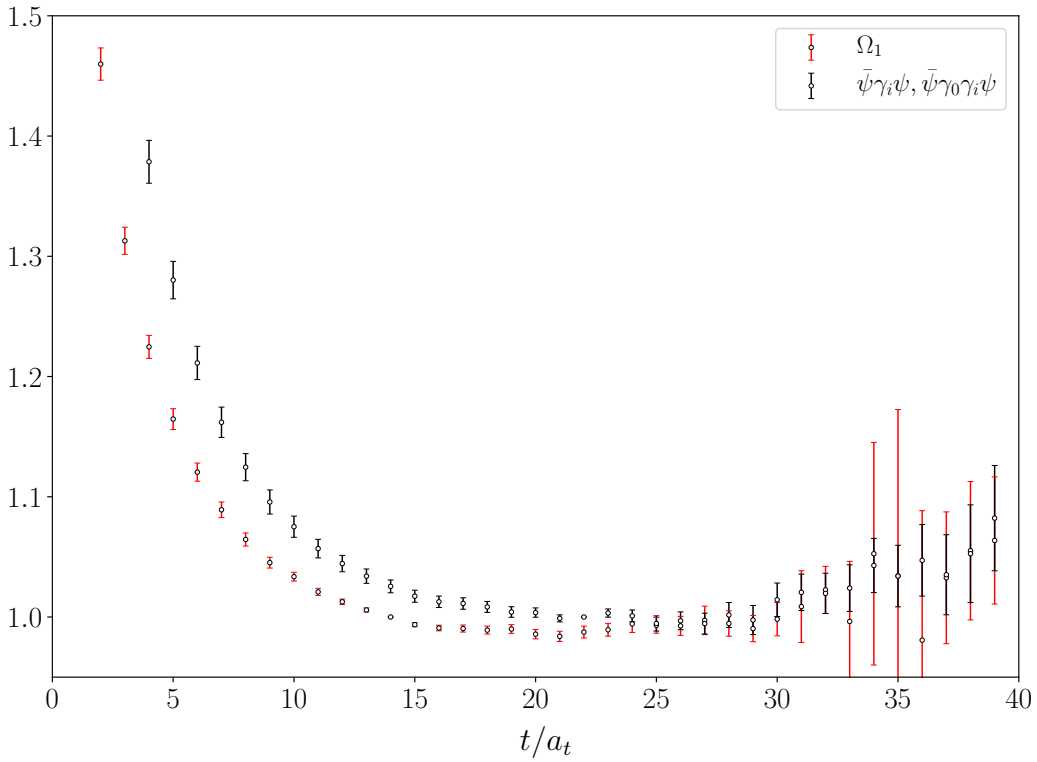

FIGURE 5.3: $\lambda e^{M(t-t_0)}$ plotted for the first excited state at rest in the T_1^{--} irrep using the fully optimised operator (shown in red) and the operator formed from a two operator basis(in black). The earlier plateau in the case of optimised operator can be seen clearly.

$$C^{\mu}_{mn}(\Delta t, t) = \langle 0|\Omega_m(\Delta t) j^{\mu}(t) \Omega_n^{\dagger}(0)|0\rangle = e^{-E_m(\Delta t - t)} e^{-E_n t} \langle m|j^{\mu}(0)|n\rangle + \ldots \quad (5.3.4)$$

The ellipsis here represents any leftover contamination from other states in the spectrum which should be minimal with appropriately chosen optimised operators, at least for the lower lying states. It is simple to see that the desired matrix element can be extracted now by simply dividing out the dominant Euclidean time dependence from the three point correlation functions.

When the decomposition shown in Eqn. 5.1.3 contains only one form factor, such as in the pseudo-scalar to pseudo-scalar transition, it is a simple task to extract a value for the form factor from the matrix element. In some cases however the form-factor decomposition will involve multiple form factors. In these cases, one correlation function will obvioulsy not contain enough information to extract multiple form factors. However multiple correlation functions at the same value

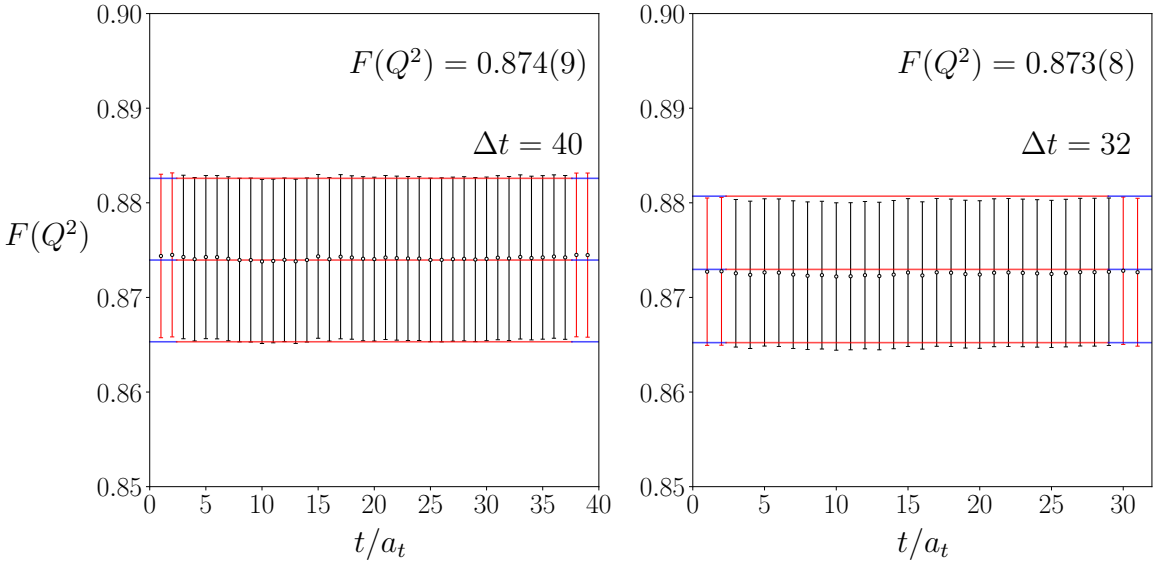

FIGURE 5.4: The temporal η_c form-factor calculated on 50 configurations for $\Delta t = 40$ (left) and $\Delta t = 32$ (right), with $\vec{p} = (0, 1, 1)$ at both source and sink. The use of only a small subset of the 603 configurations available has resulted in a larger statistical uncertainty.

of Q^2 can be used to over-constrain the system and form a matrix equation which can be inverted to find the various form-factors, [70].

When calculating the three point functions, the source and sink separation Δt is held constant and the current insertion is evaluated at each value of t, for $0 < t < \Delta t$. Figure 5.4 shows the η_c form-factor calculated on 50 configurations for $\Delta t = 40$ and $\Delta t = 32$. Both form-factors are statistically in agreement and $\Delta t = 40$ was chosen for this work to allow ample time for any excited state contamination at either the source or the sink to decay.

For each momentum and Q^2 combination one extracts a value for the form factor $F(Q^2)$ by fitting to $F(Q^2; t)$ vs t. As a first attempt, a constant fit is used when clear plateau behaviour is observed. If there is a relatively noisy plateau a fit using up to two exponential forms can allow for some residual contamination from higher excited states with energies of the order δE_n and δE_m,

$$F(Q^2; t) = F(Q^2) + f_n e^{-\delta E_n (\Delta t - t)} + f_m e^{-\delta E_m t}. \tag{5.3.5}$$

Here $F(Q^2), f_n, f_m, \delta E_n$ and δE_m are all real fit parameters. A selection of spatial current three point functions with improved η_c operators at the source and sink

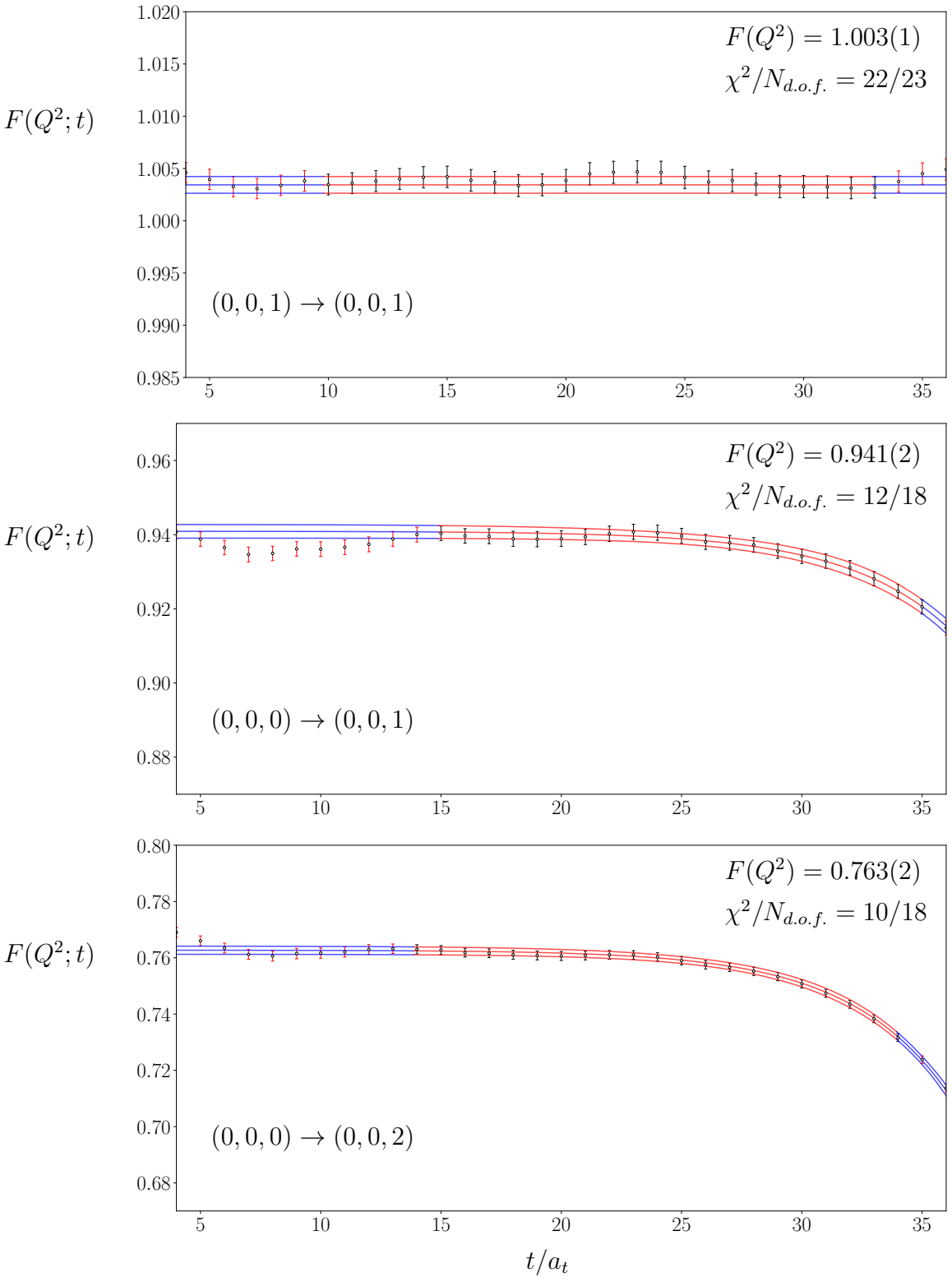

FIGURE 5.5: A selection of correlation functions plotted for a range of different source and sink momenta. Shown is $\frac{Z_V^s}{(p+p')^i} e^{E_{\eta_c}(\Delta t - t)} e^{E_{\eta_c} t} \langle 0|\Omega_{\eta_c}|\gamma^i|\Omega_{\eta_c}^\dagger|0\rangle$. Fits of the form of Eqn. 5.3.5 allow for the extraction of $F(Q^2)$.

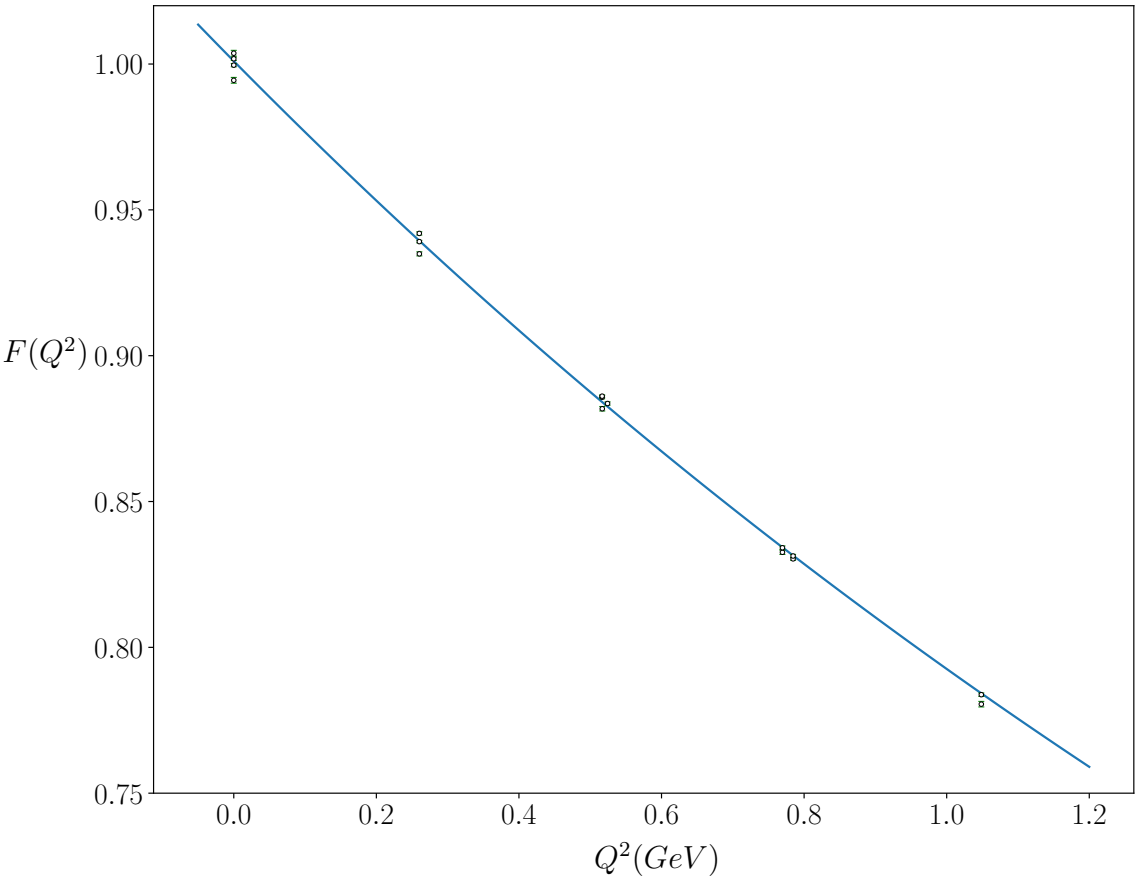

FIGURE 5.6: The temporal η_c form-factor $F(Q^2)$ vs Q^2. Each individual point is from a fit to a three point correlation function as shown in Figure. 5.5

are shown in Figure 5.5. The leading energy dependence shown in Eqn. 5.3.4 and the appropriate kinematic factor $(p + p')^\mu$ for a pseudoscalar form-factor has been removed. The data has also been renormalised by a renormalisation factor Z_V^s. For the upper most fit, it is clear that the data plateau in the central region, allowing for the extraction of $F(Q^2)$ with a simple constant fit, for that particular Q^2 value. These plateaus become shorter as the momentum at the source and sink is increased but the separation is large enough to allow a plateau to form. For the lower two fits a single exponential fit plus a constant is used, to account for some of the excited state contamination at later times.

This procedure is repeated many times and correlation functions are calculated for a range of different source and sink momenta allowing for a range of different Q^2 values. A fit can then be performed to the $F(Q^2)$ vs Q^2 allowing for the extraction of the form-factor at zero virtuality. This is shown in Figure 5.6, for the η_c form-factor. The data here has been renormalised so that the value of the

η_c form-factor at $Q^2 = 0$ is one, as will be described in the next section. When analysing transitions between different states, one cannot calculate the value of Q^2 directly for $Q^2 = 0$. A fit to the points at $Q^2 > 0$ allows one to extrapolate to $Q^2 = 0$ and make connection with experiment.

5.4 Renomalisation and Improvement of the Vector Current

In the construction of the three point correlation functions used in this work the local vector current $\bar{\psi}\gamma^\mu\psi$ is utilised. This is not conserved on a lattice with finite lattice spacing, so it must be multiplicatively renormalised with a factor Z_V. Due to the anisotropic nature of the lattice, this renormalistion factor will be different for spatial and temporal currents, giving Z_V^s and Z_V^t respectively.

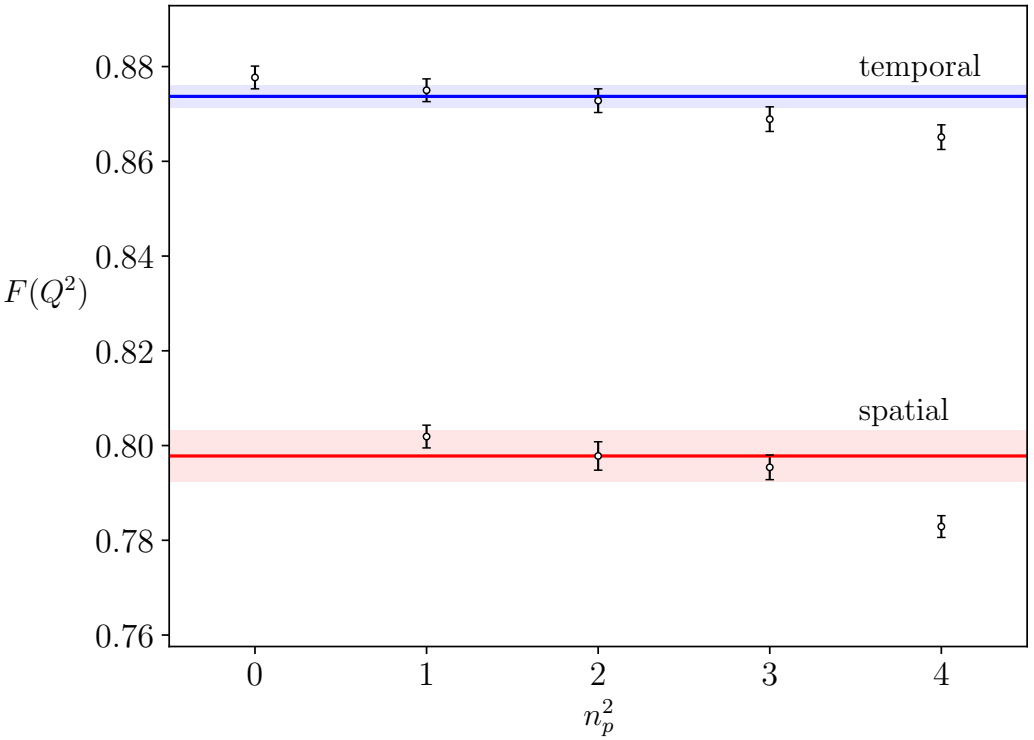

FIGURE 5.7: Value for zero momentum transfer form-factor. Plotted are the spatial (red) and temporal (blue) unrenormalised η_c form-factors for different values of $n_p^2 = (\frac{L}{2\pi})^2|\vec{p}|^2$. The horizontal bands are not fits to the data shown but show the average with the one sigma uncertainty about the average, excluding the points at $n_p^2 = 4$.

It is possible to extract these renormalisation constants from the pseudoscalar charge form-factor, which arises in the three point function with an improved η_c operator at the source and sink for zero momentum transfer. Figure 5.7 shows the value of the η_c form-factor for zero momentum transfer, for source and sink momentum $\vec{p} = (0,0,0), (0,0,1), (0,1,1), (1,1,1)$ and $(0,0,2)$ Its lattice value $F^{lat}_{\eta_c}(0)$, is normalised to its continuum value of unity (in units of e),

$$Z_V = \frac{F^{cont.}_{\eta_c}(0)}{F^{lat.}_{\eta_c}(0)} = \frac{1}{F^{lat.}_{\eta_c}(0)}. \tag{5.4.1}$$

The inverse of the average of the values for $F(Q^2)$ is used to find the renormalisation constant. The values found from a fit to the average renormalisation factor data, not including the highest momentum point were,

$$Z^s_V = 1.251(4), \qquad Z^t_V = 1.144(3), \tag{5.4.2}$$

where the errors are in the last significant figure. The errors here a purely statistical. A more complete estimate could included errors due to the discretisation, by varrying the lattice spacing at which this calculation was performed. All subsequent form-factors shown, as well as those shown in the previous section are renormalised using the appropriate renormalisation factor.

As has been previously discussed in Chapter 2, when discretising on a lattice, there are artefacts proportional to the lattice spacing in any observables calculated. One way to reduce the effect of these artefacts is via an improvement procedure [36], where additional terms are added to the lattice action so as to cancel the leading order behavior of the discretisation artifacts. The process necessary to arrive at the improved action given in Eqn. 2.4.2 can be recast as a field redefinition. Applying this same field redefinition to the fields in the vector current introduces an improvement term such that the improved renormalised currents can be ultimately written as

$$\begin{aligned} j_0 &= Z^t_V(\bar{\psi}\gamma_0\psi + \frac{1}{4}\frac{\nu_s}{\xi}(1-\xi)a_s\partial_j(\bar{\psi}\sigma_{0j}\psi)), \\ j_k &= Z^s_V(\bar{\psi}\gamma_k\psi + \frac{1}{4}(1-\xi)a_t\partial_0(\bar{\psi}\sigma_{0k}\psi)). \end{aligned} \tag{5.4.3}$$

It is clear from these expressions that it is in fact the use of an anisotropic lattice that leads to the introduction of this term, which will disappear if $a_t = a_s$, as then the anisotropy ξ will equal one. Figure 5.8 shows the effect of the use of the improved current vs the unimproved on the η_c form factor with a temporal and spatial current. It is clear that the addition of the improvement term has an effect on the values for the form-factor $F(Q^2)$ calculated, at least in the case for high Q^2, narrowing the difference observed between the spatial and temporal currents. We will utilise the improved current for the various transitions shown in the following chapter.

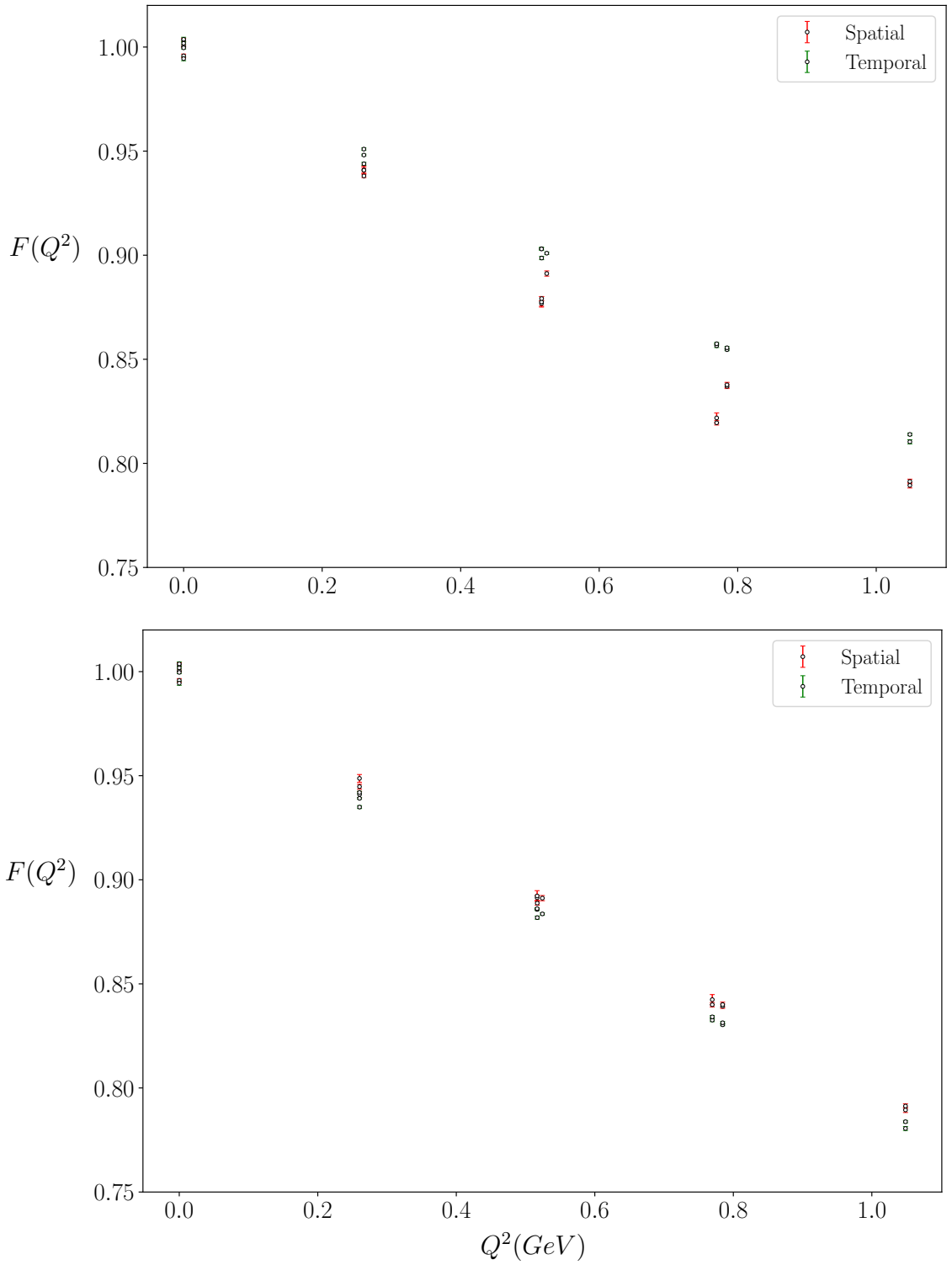

FIGURE 5.8: η_c spatial and temporal form-factors, using the unimproved (above) and improved (below) currents. Each spatial (red) and temporal (green) data point and its associated statistical error is take froma fit to $F(Q^2;t)$ vs t data, such as those shown in Figure 5.5.

In summary, in this chapter it was shown how it is possible to investigate radiative transition matrix elements on the lattice:

1. Create a large basis of lattice subduced helicity operators $\mathbb{O}_i^\dagger$ for a range of different momentum values, in any symmetry channel of interest.

2. Form optimal combinations of the operators in this basis for each symmetry channel which interpolate from the vacuum the state in question. This is done by using the variational method to solve the GEVP $C_{ij}(t)v_j^n = \lambda^n(t,t_0)C_{ij}(t_0)v_j^n$ for the generalised eigenvectors v_j^n.

3. Using these improved operators compute three point correlation functions between the states in question with a vector current insertion. Different combinations of source and sink momentum allows access to a range of Q^2 values.

4. After proper normalistion, these three point functions can be expressed as a sum over a number of form-factors $F(Q^2)$. These can be extracted from the time slice data by removing the dominant energy dependence and fitting to plateaus in the $F(Q^2 : t)$ vs t data.

5. When enough values for $F(Q^2)$ have been computed a fit vs Q^2 allows for the extraction of the form-factor at $Q^2 = 0$. This can then be used to make contact with experiment.

Chapter 6

Radiative Transitions Results

It has been shown how Lattice QCD can be used to investigate the charmed meson spectrum by analysing two point functions using the variational method. It was also discussed how this can be extended to the analysis of three point functions which allows one to investigate some interesting quantities such as vector current matrix elements involved in decays. In this chapter, results of a lattice calculation in the charmonium sector for a number of transitions involving the emission of a photon are discussed. This data is used to extract form-factors and where possible make a link to experimentally measured transition rates [75, 76].

These transitions in charmonium were first investigated by members of the Hadron Spectrum Collaboration on quenched lattices using domain wall fermions in reference [72]. This was expanded on in reference [73] where some higher excited and exotic transitions in charmonium were included. The first use of the distillation method and variationally optimised operators to investigate radiative transitions was in the light sector with $N_f = 3$ dynamical lattices discussed in reference [70]. These studies paved the way for this work which employs distillation and the variationally optimised operator technology on $N_f = 2 + 1$ dynamical lattices to investigate radiative transitions in charmonium for the first time.

A number of other groups have also performed studies of transitions in the charmonium spectrum. In particular for the decay $J/\psi \to \eta_c\gamma$, calculations using $N_f = 2$ twisted mass fermions [77, 78] or the highly improved staggered quark action on

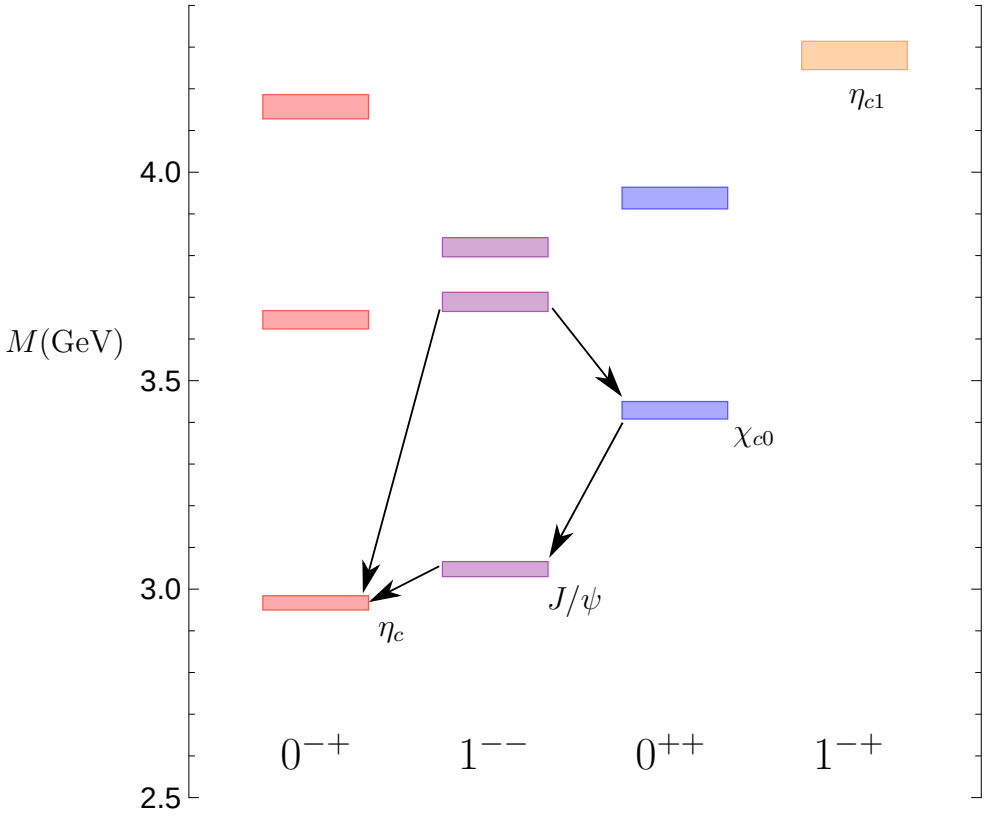

FIGURE 6.1: A simple charmonium spectrum calculated on the 20^3 lattices. Shown schematically are the experimentally allowed transitions, as well as the exotic hybrid state in the $J^{PC} = 1^{-+}$ channel. In each case the height of the box denotes the statistical uncertainty measured in the energy.

$N_f = 2 + 1$ lattices [79] have been performed. These results provide a fairly consistent theoretical estimate of this decay width which provides a benchmark for the work discussed here.

Figure 6.1 shows the spectrum of states calculated on the lattice described in the following section with details shown in Table 6.1. Plotted is the energy of the lowest few states in the J^{PC} channels relevant for the η_c, J/ψ, χ_{c0} and exotic hybrid 1^{-+} η_{c1} state. The energies have been converted form lattice units to GeV and the height of each box represents the statistical uncertainty associated with each energy.

As has been stated before, transitions involving the emission of a photon occur only between states of different C, as shown in the figure. However in this study the photon is coupled solely to the quark line in the meson and so it is possible to analyse transitions between states of the same C. The arrows in Figure 6.1 show some of the potential transitions allowed in the charmonium spectrum via the

emission of a photon. These transitions all have experimentally measured partial decay widths which have been tabulated in reference [63].

6.1 Calculation Details

The three point correlation functions necessary for this calculation were calculated on an $N_f = 2+1$ anisotropic lattice of volume $20^3 \times 128$, generated using the same action as described in reference [28]. The pion mass, M_π, was measured to be approximately 391 MeV. Information on these gauge configurations can be seen in Table. 6.1. More details on these ensembles can be found in [59].

The majority of the correlators were evaluated on the full 603 gauge configurations available, however due to time and storage constraints some transitions were calculated on a reduced set of 300 configurations. All correlation functions were calculated with $\Delta t = 40$.

As discussed before, the charm quark mass has been tuned so as to reproduce the relativistic dispersion relation shown in Eqn. 4.1.1. The dispersion relation for the η_c meson is shown in Figure. 6.2. The anisotropy was determined, when not including the final $n^2 = 4$ point, to be 3.476(3) which agrees closely with the value extracted from the D meson dispersion relation of $\xi = 3.454(6)$ on the same lattice. This allows us to be sure that discretisation effects due to the tuning are small. With the inclusion of the $n^2 = 4$ point the anisotropy is found to be approximately $\xi = 3.5$, however the $\chi^2/N_{d.o.f.}$ for the fit was very large. This is consistent with a larger discretisation effect in the case of data involving a boost of $\vec{p} = (0, 0, 2)$. This effect can also be seen in Figure 5.7 in the extraction of Z_V. Primarily, boosts of up to $\vec{p} = (1, 1, 1)$ were used to minimize any effect this may have on the $F(Q^2)$ extraction. The Ω-baryon mass was found on this lattice to

Lattice Volume	M_π (MeV)	N_{cfgs}	N_{tsrcs}	N_{vecs}
$20^3 \times 128$	391	603(300)	1	128

TABLE 6.1: Details of the lattice gauge field ensembles used. Volume is given as $(L/a_s)^3 \times (T/a_t)$ where L and T are respectively the spatial and temporal extents of the lattice. The number of gauge configurations used, N_{cfgs}, and the number of time-sources used per configuration, N_{tsrcs}, are shown along with the number of eigenvectors used in the distillation, N_{vecs}.

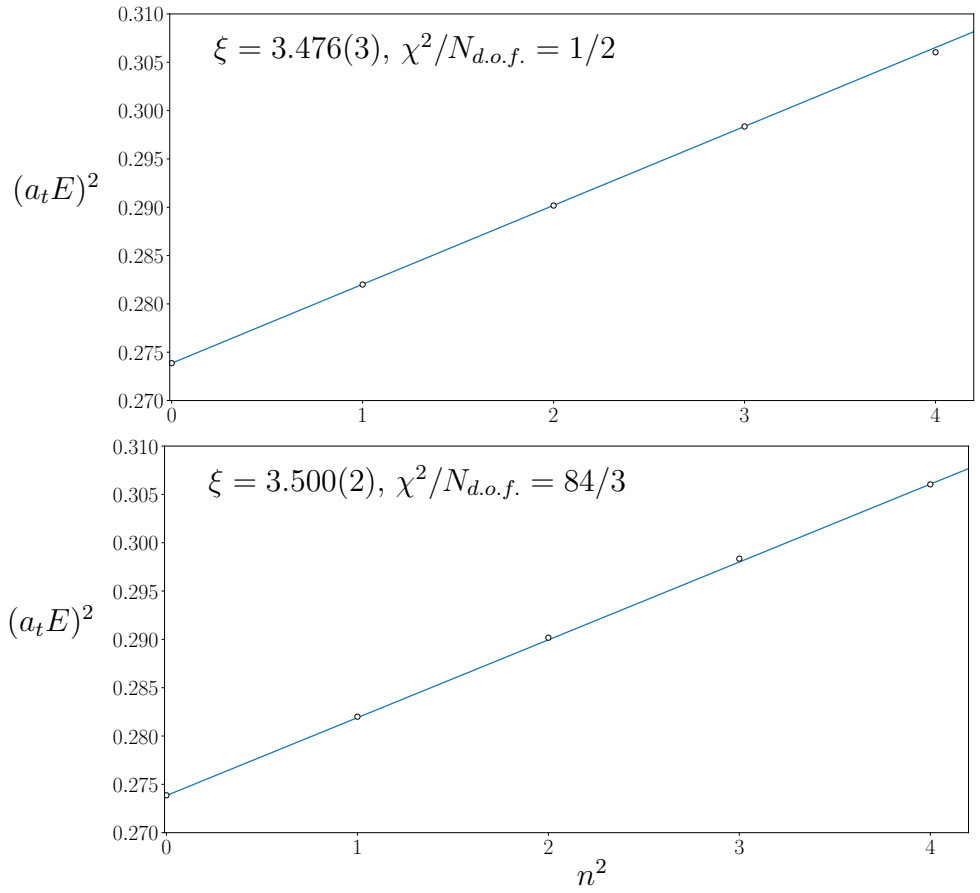

FIGURE 6.2: Dispersion relation for the η_c meson measured on the $m_\pi \sim 391$ lattice. The fit in the above panel does not include the $n^2 = 4$ points, which is included in the lower panel.

be $a_t m_\Omega = 0.2951$, leading to an inverse lattice spacing and conversion factor of $a_t^{-1} = 5.667$ GeV [59].

6.2 Form-Factors

First some elastic radiative form-factors in charmonium, namely the η_c, η_c' and χ_{c0} form-factors will be investigated. These benchmark calculations can be used to test the efficacy of the method used as well as compare to previous studies of the same quantities, such as references [72, 77].

6.2.1 η_c Form-Factor

The simplest transition to investigate is between a ground state pseudoscalar η_c meson and itself, $\eta_c \to \eta_c\gamma$. As this is not a physical transition it cannot be compared to experiment, however it may be used to shed some light on the internal charge distribution of the meson resulting in a charge radius.

The single form factor of interest, $F_{\eta_c}(Q^2)$, appears in the Lorentz decomposition of the vector current matrix element with improved η_c operators at the source and sink,

$$\langle \eta_c(p')|j^\mu|\eta_c(p)\rangle = (p+p')^\mu F_{\eta_c}(Q^2). \tag{6.2.1}$$

Three point correlation functions were evaluated for a range of source and sink momentum combinations allowing for momentum transfers of $\vec{p} = (0,0,0), (0,0,1), (0,1,1), (1,1,1)$ and $(0,0,2)$. This provides for an adequate range of Q^2 values, allowing for an accurate fit to the $F(Q^2)$ data vs Q^2.

These correlation functions are calculated for temporal and spatial currents and are renormalised by the aformentioned renormalisation factors Z_V^t or Z_V^s respectively. This then gives the matrix element of interest by removing the dominant energy dependence given in Eqn. 5.3.4. As was seen earlier in Figure 5.5, a number of correlation functions with clear plateaus away from the source and sink allow for an accurate extraction for $F(Q^2)$. Figure 6.3 shows the η_c form-factor $F_{\eta_c}(Q^2)$ vs Q^2 calculated for the unimproved temporal and spatial current.

The data was fit using an exponential form as described in [72],

$$F(Q^2) = F(0)\exp[-\frac{Q^2}{16\beta^2}(1+\alpha Q^2)], \tag{6.2.2}$$

with fit parameters, $F(0)$, α and β, for values of $Q^2 > 0$. It is clear that for the unimproved current the temporal data is described more accurately by the fit. A larger spread of points about the fit can be seen in the case of the spatial current, and the extracted value of $F(0)$ is not consistent with one. This may be due to the larger spacing in the spatial directions, leading to increased discretisation errors.

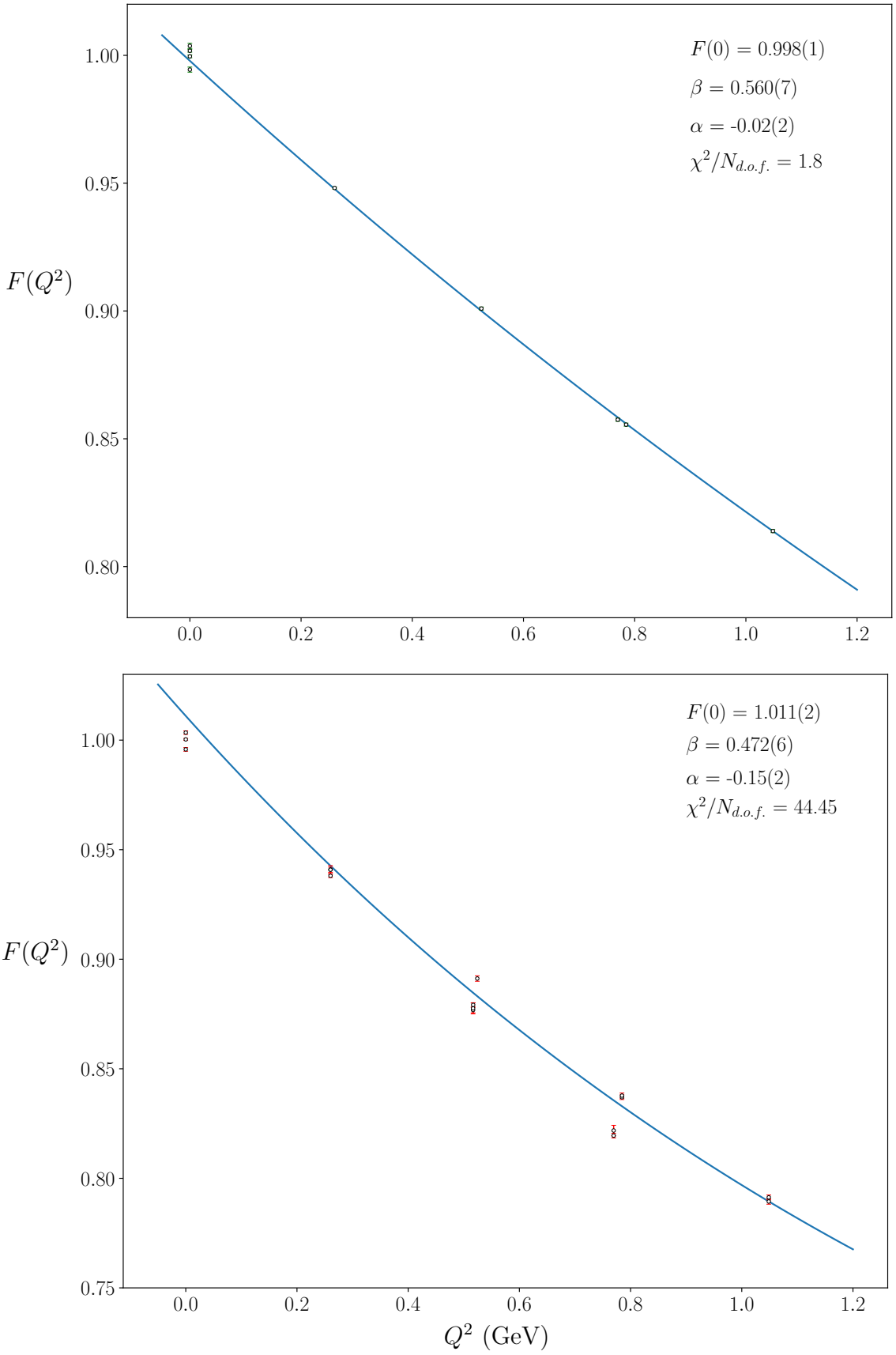

FIGURE 6.3: η_c form-factor, $F(Q^2)$, for unimproved temporal (above) and spatial (below) currents. Each data point and its one sigma uncertainty is from a fit to a three-point function with different source and sink momentum. $Q^2 = 0$ data is not included in the fit.

Figure 6.4 again shows the η_c form-factor, this time computed with the improved current. It can be seen that the addition of the improvement term reduces the spread in the spatial current so that it is more accurately described by the fit. The extracted value of $F(0)$ is now consistent with unity for both spatial and temporal currents, which is expected as the data has been renormalised such that the form factor at $Q^2 = 0$ is unity. The fact that the fit to the $Q^2 > 0$ data gives an appropriate $F(0)$ value shows that no extra renormalisation is necessary.

In addition, as was mentioned in Chapter 5, the improved temporal and spatial currents agree more closely than in the unimproved case. It is possible to define a squared charge radius for the meson [72], via the slope of the form-factor at $Q^2 = 0$, as

$$\langle r^2 \rangle = \frac{6}{16\beta^2}. \tag{6.2.3}$$

This can be used to characterise the distribution of charge in the meson. The values extracted from the fit using the improved current shown in Figure 6.4 can then be used to give an estimate of this charge radius. The fits to both the improved spatial and temporal currents now show an appropriate $\chi^2/N_{d.o.f.}$ close to one. Using the values for β from these fits it was found that

$$\langle r_s^2 \rangle^{\frac{1}{2}} = 0.234(4)\text{fm}, \quad \langle r_t^2 \rangle^{\frac{1}{2}} = 0.236(2)\text{fm}. \tag{6.2.4}$$

These values are in line with previous results from references [72, 77], the former finding a value of 0.255(2) fm from a quenched study, while the latter found a value of 0.213(1) fm from a $N_f = 2$ calculation. As described in [77], it is expected that an unquenched calculation should give a smaller radius than its quenched counterpart, due to the increased coupling strength due to the unquenching. A more complete analysis taking into account the various systematic errors discussed in Chapter 1, could explain some of the descrepancy with previous results.

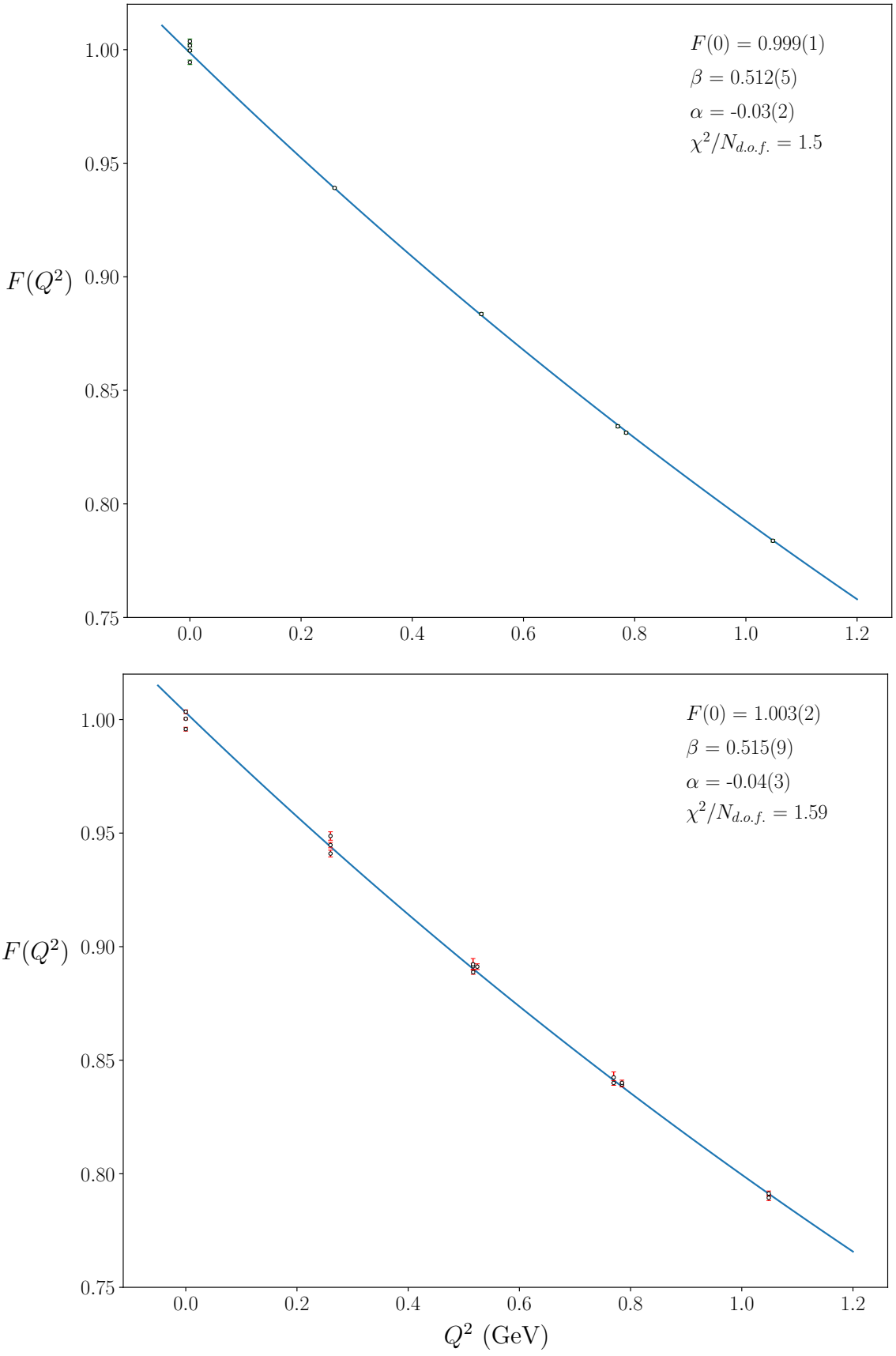

FIGURE 6.4: η_c form-factor for improved temporal (above) and spatial (below) currents. Each data point and its one sigma uncertainty is from a fit to a three-point function with different source and sink momentum. $Q^2 = 0$ data is not included in the fit.

6.2.2 χ_{c0} Form-Factor

The second form-factor of interest is for the ground state χ_{c0}. In this case the decomposition for the matrix element $\langle\chi_{c0}(p')|j^{\mu}|\chi_{c0}(p)\rangle$ is the same as for the η_c, shown in Eqn. 6.2.1.

The signal in both the two-point functions for this state necessary to create the optimised χ_{c0} operator and the three point functions calculated with this optimised operator were slightly noiser than those for the η_c. This is reflected in the larger statistical errors in the individual $F(Q^2)$ values. As well as this a number of momentum combinations failed to produce a satisfactory plateau, and so were not included.

Despite the noisier signal, a number of combinations showed appropriate plateaus. Figure 6.5 shows $F(Q^2)$ vs Q^2 for the χ_{c0} computed for the improved temporal and spatial currents. The data is again fit with the analytic form shown in Eqn. 6.2.2. The data is accurately described by this fit, with low $\chi^2/N_{d.o.f.}$ values in part due to the increased statistical uncertainty.

Following the same procedure as before the charge radius for the χ_{c0} can be estimated from the fit parameter β. This results in

$$\langle r_s^2\rangle^{\frac{1}{2}} = 0.34(3)\text{fm}, \quad \langle r_t^2\rangle^{\frac{1}{2}} = 0.30(2)\text{fm}. \tag{6.2.5}$$

As is expected, the charge radius for the χ_{c0} is notably larger than the η_c. This makes sense as the χ_{c0} can be thought of as a P-wave state, which is spatially larger due to the increased angular momentum of the constituent quarks.

It should be noted that it was necessary to include some data points at $Q^2 = 0$ in the fit so as to extract a value for $F(0)$ which is consistent with one.

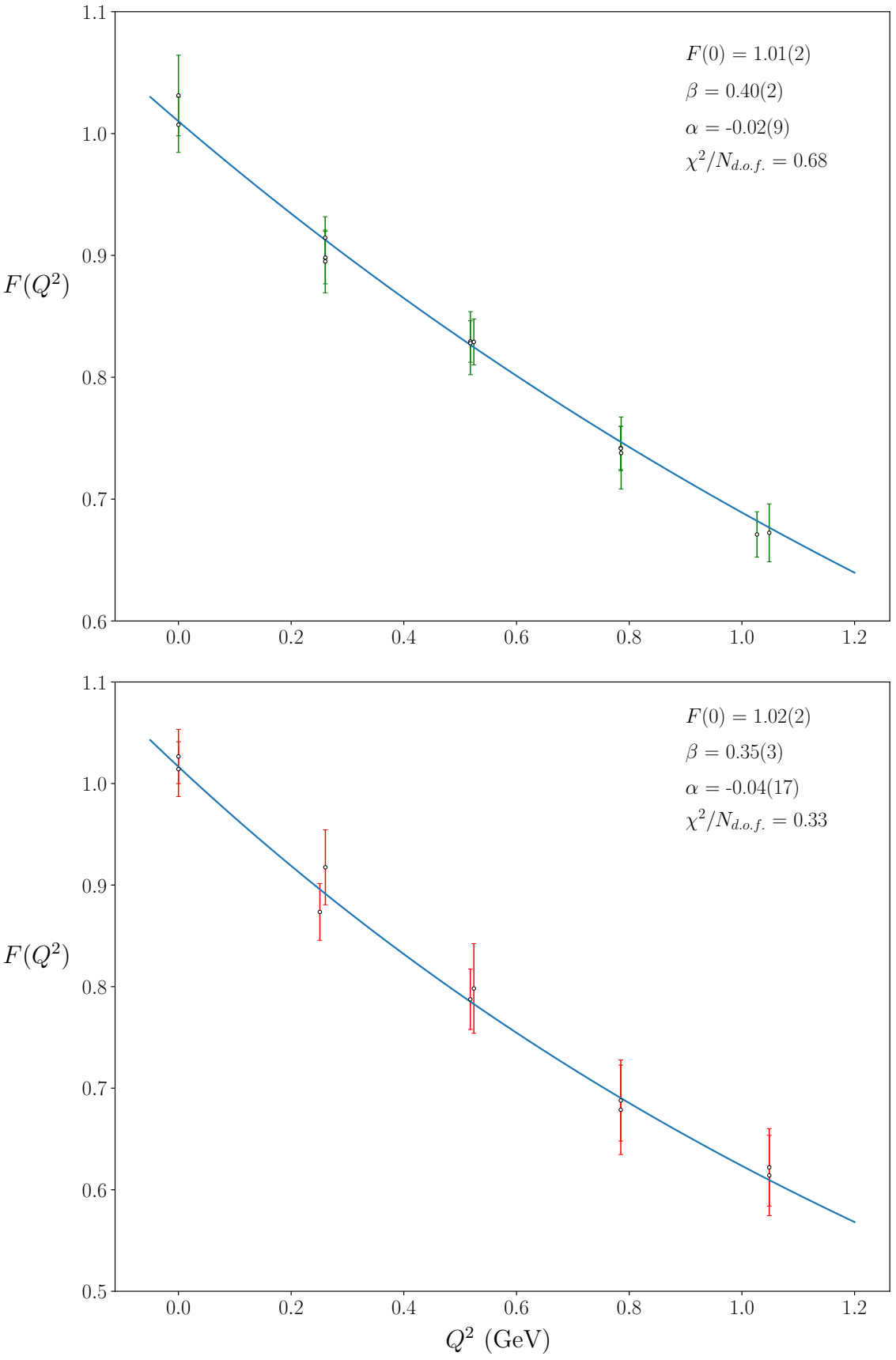

FIGURE 6.5: χ_{c0} form-factor for improved temporal (above) and spatial (below) currents. Each data point and its one sigma uncertainty is from a fit to a three-point function with different source and sink momentum.

6.2.3 η_c' Form-Factor

As the aim is to work towards investigating transitions involving excited states in the charmonium spectrum, it is prudent to investigate the form-factor for the lowest lying excited state, the η_c'. The form-factor decomposition is the same here as it was in the previous two cases, with one single form-factor as shown in Eqn. 6.2.1.

Unfortunately when dealing with excited states, considerably more noise is observed in the three point correlation functions leading to increased uncertainty in any form-factor extraction. This uncertainty is then increased further when dealing with correlation functions involving states with higher momenta.

Figure 6.6 shows the form-factor $F(Q^2)$ vs Q^2 temporal and spatial currents. It is evident that there is a much larger statistical uncertainty in each $F(Q^2)$ extraction, which is subsequently reflected in the rather low $\chi^2/N_{d.o.f.}$ value and large errors on the individual fit parameters. $F(0)$ is found to not be consistent with one, even when the data at $Q^2 = 0$ is included in the fit. This suggests that an additional renormalisation constant is necessary in the case of excitations with weaker signals.

The values for the charge radius were found to be

$$\langle r_s^2 \rangle^{\frac{1}{2}} = 0.49(13)\text{fm}, \quad \langle r_t^2 \rangle^{\frac{1}{2}} = 0.45(7)\text{fm}. \tag{6.2.6}$$

Again it was found that the spatial extent of the η_c' is larger than that of the η_c and χ_{c0}, as expected for an excited state.

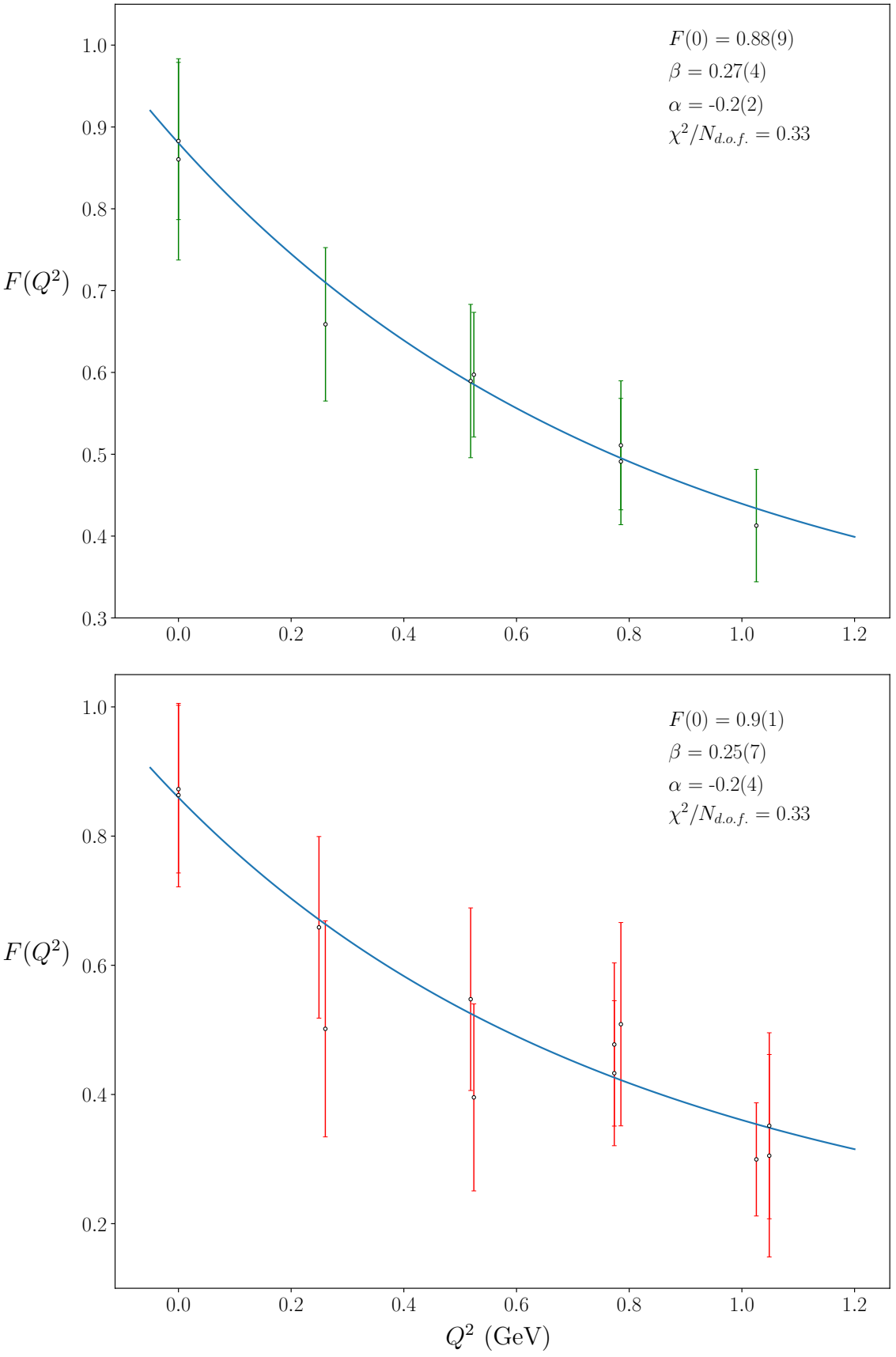

FIGURE 6.6: η_c' form-factor for improved temporal (above) and spatial (below) currents. Each data point and its one sigma uncertainty is from a fit to a three-point function with different source and sink momentum.

6.3 Radiative Transitions

In this section two different transitions will be investigated. First the transition between the two lightest states in the charmonium spectrum, $J/\psi \to \eta_c\gamma$, which will then be followed by an investigation of the transition $\chi_{c0} \to J/\psi\gamma$. As was mentioned before, below the $D\bar{D}$ threshold, charmonium states are OZI suppressed, meaning these transitions have non-negligible, transition rates which can be measured in experiment [80].

6.3.1 $J/\psi \to \eta_c\gamma$ Transition

The matrix element of interest for the $J/\psi \to \eta_c\gamma$ transition can be expressed with a single form-factor as

$$\langle \eta_c(p')|j^\mu|J/\psi(\lambda,p)\rangle = \epsilon^{\mu\nu\rho\sigma} p'_\nu p_\rho \epsilon_\sigma(\lambda,p) \frac{2}{m_{\eta_c}+m_{J/\psi}} F_{J/\psi\eta_c}(Q^2), \tag{6.3.1}$$

where $\epsilon_\sigma(\lambda,p)$ is the polarisation vector for the J/ψ with momentum p and helicity λ. The partial decay width for this transition can be related to the form-factor at zero virtuality measured on the lattice by

$$\Gamma(J/\psi \to \eta_c\gamma) = \frac{64\alpha}{27} \frac{|\mathbf{q}|^3}{(m_{\eta_c}+m_{J/\psi})^2} |F_{J/\psi\eta_c}(0)|^2, \tag{6.3.2}$$

where α is the fine structure constant. In the frame where the J/ψ is at rest it is found that, for $Q^2 \to 0$,

$$|\mathbf{q}|^2 = \frac{(m_{J/\psi}^2 - m_{\eta_c}^2)^2}{4m_{J/\psi}^2} \tag{6.3.3}$$

There is however a slight ambiguity in whether to use lattice or experimental masses in these equations to make connection to experimental results. Table 6.2 shows the values for the masses found on the lattice as well as their experimental counterparts. While the energies extracted on the lattice are quite close to the experimental values, the difference between the lightest two charmonium states, the η_c and J/ψ, known as the hyperfine splitting, is found to be less than in

	m_{η_c}	$m_{J/\psi}$	$m_{\chi_{c0}}$
Lattice	2966.4(3)	3046.9(4)	3430(2)
Experiment	2983.9(5)	3096.9(6)	3414.7(3)

TABLE 6.2: Summary of the masses for the $\eta_c, J/\psi$ and χ_{c0} found on the lattice, as well as their experimental values quoted in the PDG [63]. All figures are quoted in MeV. All errors are in the last digit.

experiment. This is a well known problem in lattice studies and is sensitive to the discretisation used, the values for the quark masses and the inclusion of the disconnected diagrams in the correlators [81]. The value for the splitting found here of 81(1) MeV is consistent with that found on 16^3 and 24^3 lattices with the same pion mass [25], suggesting it is not due to finite volume effects. In references [25, 48] it was discussed that an increase of the clover coefficient from the tree-level tadpole-improved value of $c_{SW} = 1.35$ to 2 resulted in a value for the hyperfine splitting which was in line with the experimental value. This allows for an estimate of the leading $O(a_s)$ systematic uncertainty which was found to be $\sim O(40)$ MeV on these lattices. This uncertainty is not included in the results presented in this thesis.

In the same way as before, improved spatial current correlation functions for different momentum combinations at source and sink are calculated which will allow for the extraction of a value for the form-factor $F(Q^2)$ at zero virtuality. Combinations resulting in $Q^2 < 0$, ie. when $p_i = p_f$, were found to produce no discernable plateau or were polluted with large amounts of noise and so are not included. To extract the form-factor at zero virtuality the data was fit to an exponential fit form

$$F(Q^2) = F(0)e^{-\frac{Q^2}{16\beta^2}}, \tag{6.3.4}$$

with fit parameters $F(0)$ and β. This form is motivated by simple quark model considerations as described in reference [72]. Figure 6.7 shows the form-factor $F(Q^2)$ vs Q^2. The data was found to be well described by the fit, up to momentum transfers of $\vec{p} = (1, 1, 1)$. A single point, with momentum transfer $\vec{p} = (0, 0, 2)$ is shown in Figure 6.7, but is not included in the fit. The same discretisation errors when dealing with higher momentums seen before arise here.

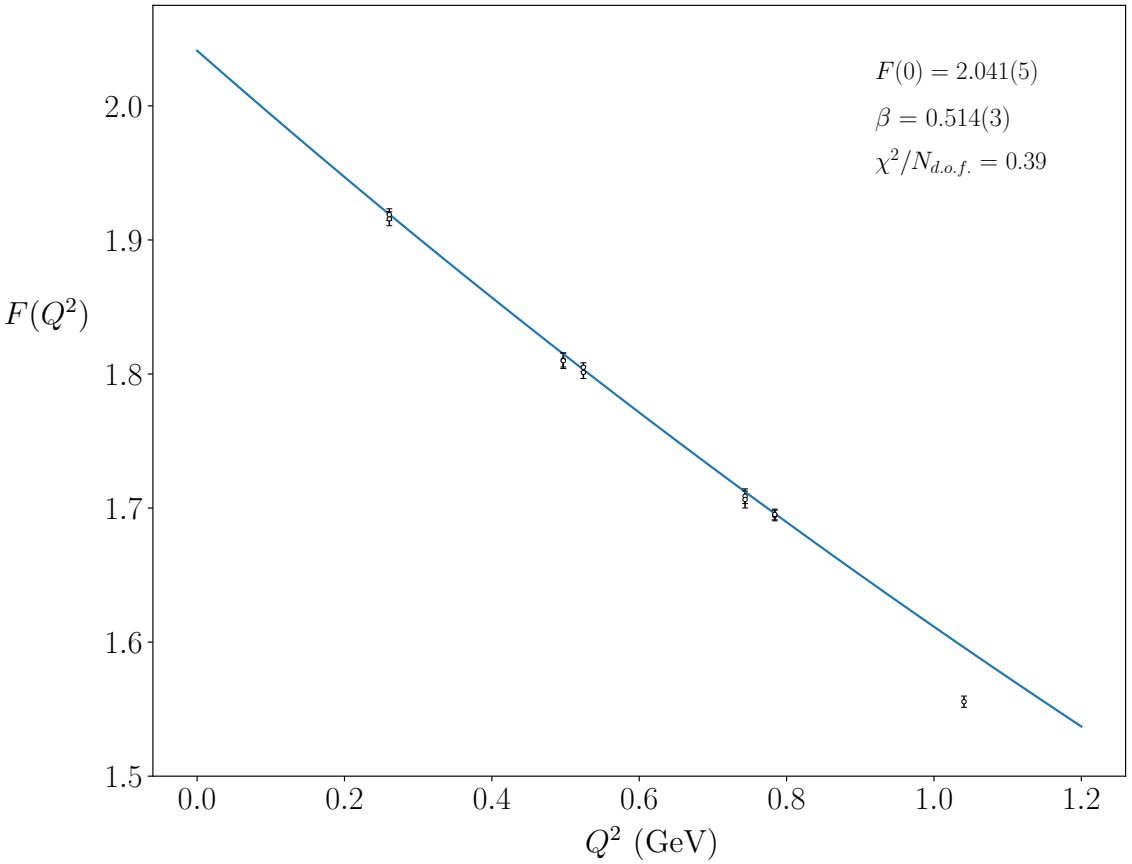

FIGURE 6.7: Form-factor $F(Q^2)$ vs Q^2 for the $J/\psi \to \eta_c$ transition using the improved spatial current. Each data point and its one sigma uncertainty is from a fit to a three-point function with different source and sink momentum.

Using the value of $F(0) = 2.041(5)$ extracted from the fit to the $F(Q^2)$ data the partial decay width, Γ, can be estimated using Eqn. 6.3.2 and was found to be

$$\Gamma_{m_{exp}} = 2.66(4)\text{keV}, \qquad \Gamma_{m_{lat}} = 1.01(1)\text{keV}, \tag{6.3.5}$$

where m_{exp} and m_{lat} are found using the experimental and lattice masses for the η_c and J/ψ respectively. These values lie on either side of the value for the decay width quoted in the PDG of 1.6(4) keV [63].

As $\mathbf{q}$ is quite sensitive to differences in the hyperfine splitting any change in the value used will have a large effect on these decay rates, which depends on $\mathbf{q}^3$, and explains the large difference between the two values. Moving towards physical quark masses with a more accurate value for the hyperfine splitting may help to decrease this difference.

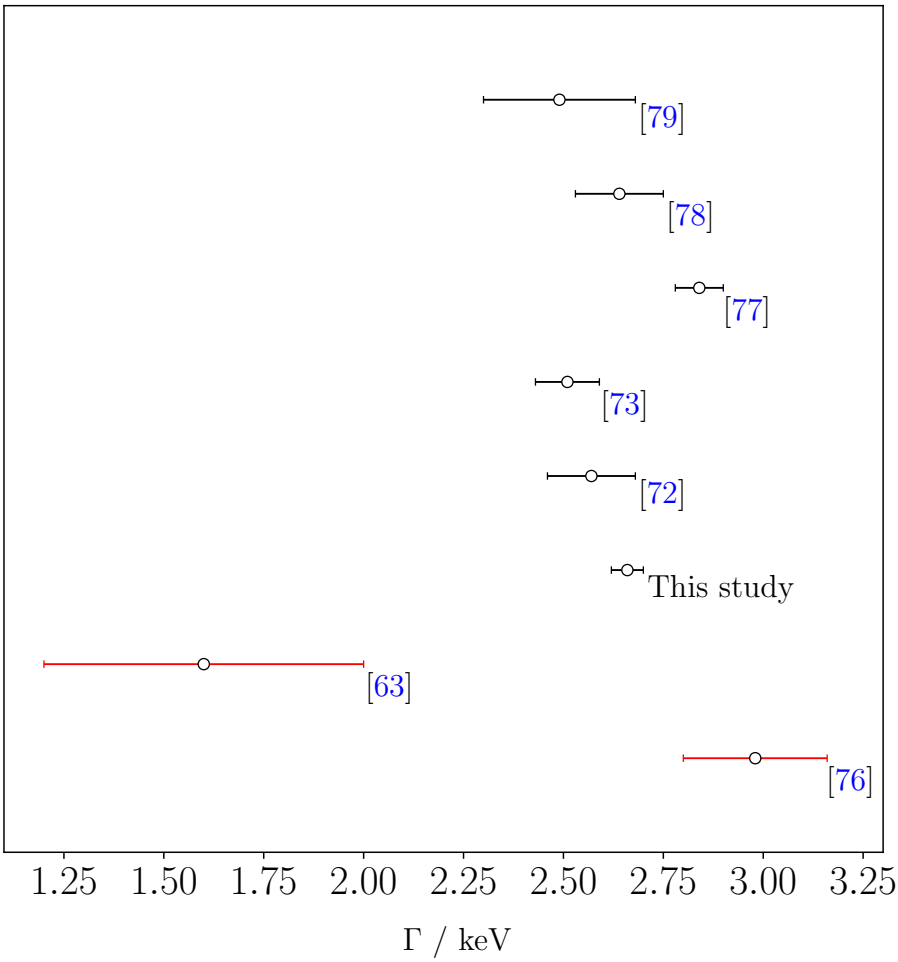

FIGURE 6.8: Comparison of the results from different lattice calculations of $\Gamma(J/\psi \to \eta_c\gamma)$ using experimental masses, as well as the PDG average [63] and experimental result from KEDR [76] in red. The error budgets in references [78] and [79] are more complete than in this work and so result in larger error bars.

A number of other lattice studies investigating this transition have also been performed, with results shown in Figure 6.8 The value found in this study using experimental masses for the η_c and J/ψ of 2.66(4) keV is consistent with the result of 2.57(11) keV found in the original quenched paper [72]. It is also consistent with the results found in dynamical studies of 2.64(11) keV [78] and 2.49(19) keV [79]. While not included in the PDG average, a recent experimental study at KEDR [76] quotes a larger decay width of $\Gamma(J/\psi \to \eta_c\gamma) = 2.98(18)$ keV, which is considerably closer to the lattice results. The inclusion of this result in the PDG average could remove some of the descrepancy between the lattice and PDG results.

6.3.2 $\chi_{c0} \to J/\psi\gamma$ Transition

The matrix element for the $\chi_{c0} \to J/\psi\gamma$ transition can be characterised by two form-factors as shown in Eqn. 5.1.8, an electric form-factor $E_1(Q^2)$ and a longitudinal form-factor $C_1(Q^2)$. Physically, only E_1 is measurable in experiment, as all photons must be on-shell ie. $Q^2 = 0$. It is possible to choose certain momentum combinations such that C_1 does not contribute, even for values of $Q^2 > 0$, leaving the matrix element simply proportional to $E_1(Q^2)$,

$$\langle \chi_{c0}(\vec{p}')|j^\mu|J/\psi(\lambda,\vec{p})\rangle = E_1(Q^2)\epsilon^\mu(\lambda,\vec{p}). \tag{6.3.6}$$

Here again $\epsilon^\mu(\lambda,\vec{p})$ is the polarisation of the vector J/ψ. In order to make connection with experiment, the partial decay width for the $\chi_{c0} \to J/\psi\gamma$ can be expressed as

$$\Gamma(\chi_{c0} \to J/\psi\gamma) = \alpha\frac{|\vec{q}|}{m^2_{\chi_{c0}}}\frac{16}{9}|\hat{E}_1(0)|^2, \tag{6.3.7}$$

where α is the fine structure constant and $\hat{E}_1$ is the form-factor extracted on the lattice. As before there is some ambiguity as to whether one should use the experimental or lattice mass for the χ_{c0} in this equation. The value for $m_{\chi_{c0}}$ extracted on this lattice was found to be 3430(2) MeV, which is to be compared with the experimental value of 3414.7(3) MeV quoted in the PDG [63].

Spatial three point functions for a number of momentum combinations were computed using the improved current such that the decomposition shown in Eqn. 6.3.6 could be used. The form-factor $E_1(Q^2)$ was then found by fitting the data to an exponential form again motivated by simple relativistic quark model calculations as suggested in [72],

$$F(Q^2) = \hat{E}_1(0)(1+\lambda Q^2)\exp[-\frac{Q^2}{16\beta^2}], \tag{6.3.8}$$

with fit parameters $\hat{E}, \lambda$ and β. This fit can be seen in Figure 6.9. From the fit a value for the form-factor $\hat{E}(0)$ of 0.140(1) in lattice units was found.

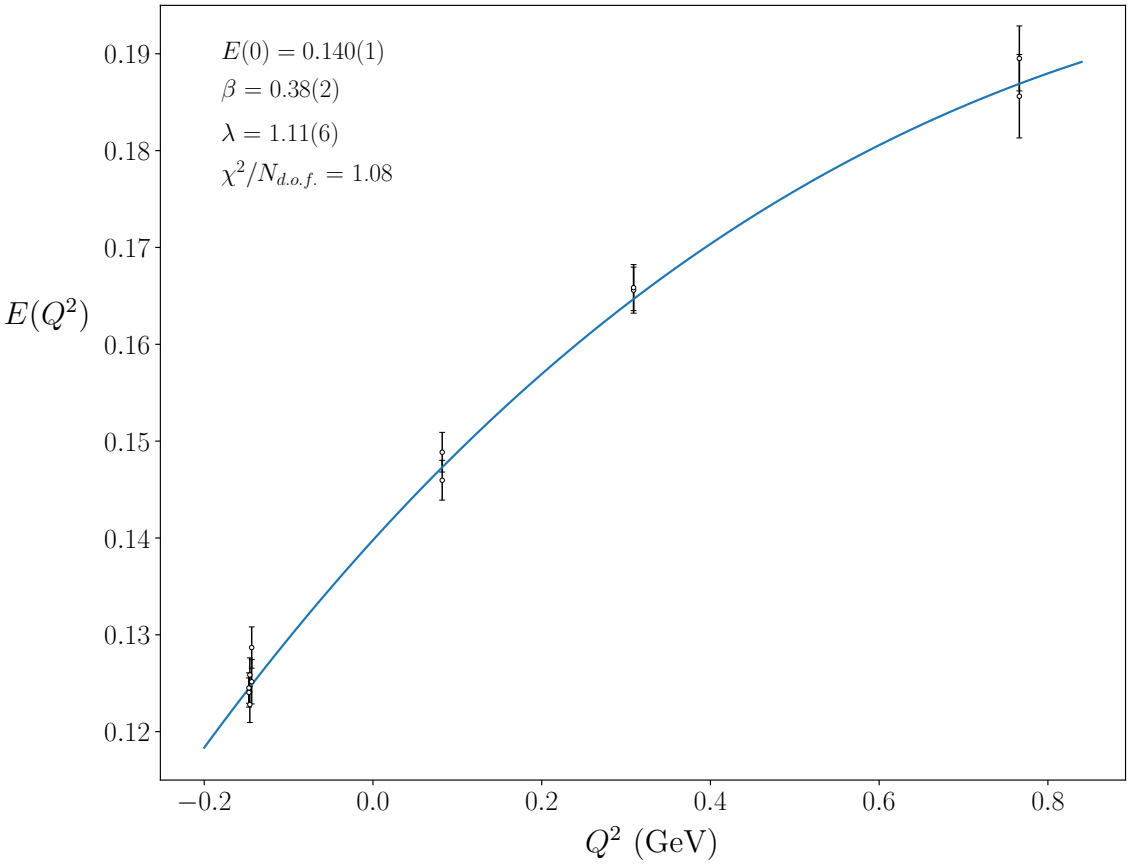

FIGURE 6.9: Form-factor $E(Q^2)$ vs Q^2 for the $\chi_{c0} \to J/\psi$ transition using the improved spatial current. Each data point and its one sigma uncertainty is from a fit to a three-point function with different source and sink momentum.

The results for the partial decay width using both experimental and lattice masses were found to be

$$\Gamma_{m_{exp}} = 212(3) \text{ keV}, \qquad \Gamma_{m_{lat}} = 251(3) \text{ keV} \tag{6.3.9}$$

This is to be compared with the PDG average experimental value of 147(12) keV. In the previous quenched studies, the values found for this transitions using the experimental masses were 232(41) keV [72] and 131(14) keV [73], which fall either side of the value found here. Reference [77] also quotes a value for this transition, however it is substantially lower at 85(7) keV.

6.4 Exotic η_{c1} (1^{-+}) State

The goal of this current work was to work towards the calculation of transitions involving exotic or hybrid states. This would be a timely goal as there is currently much interest in the phenomenology of these hybrid states in the physics community. In reference [73], the authors investigate a transition between the exotic $J^{PC} = 1^{-+}$ state, referred to as the η_{c1}, and J/ψ, where it is identified as a hybrid. This state was also identified to be a hybrid in reference [25], where it was proposed that it is part of the lightest hybrid supermultiplet in charmonium. It can be explained as an S-wave quark-antiquark pair coupled to a 1^{+-} gluonic excitation.

Figure 6.10 shows the principal correlators for the η_c, η_c' and η_{c1} as found in this work. It is clear that the signal for the η_{c1} state is considerably more noisy than the relatively flat η_c and η_c'. The plateau exists only for a short number of timeslices before disappearing into noise. It is proposed that to investigate this transition a greater number of timesources are necessary to get an adequate plateau that extends out far enough to extract a reliable signal from the three point functions. As this was an exploratory study only one timesource was used, in contrast to the maximum of 128 used in reference [25]. Unfortunately the generaton of more timesources was not feasible due to the time constraints for this thesis but a more in-depth analysis of this transition would be next in line to be analysed.

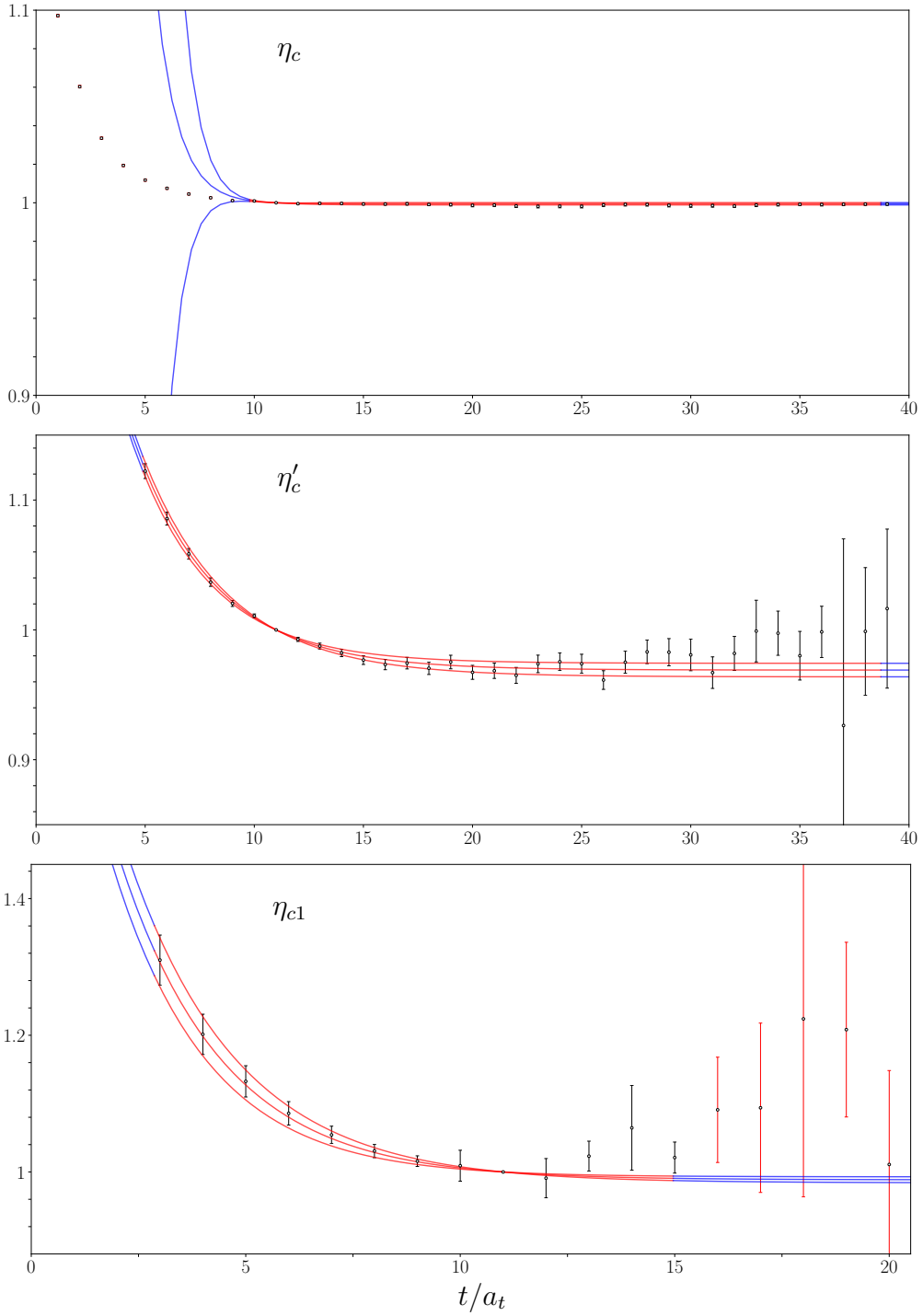

FIGURE 6.10: Principal correlators $\lambda^n e^{M_n(t-t_0)}$ for η_c, η_c' and η_{c1} at rest for $t_0 = 11$. Points in red are not included in the fit. The hybrid state η_{c1} signal disappears into noise after a small number of timeslices.

6.5 Summary of Results

Results from a dynamical $N_f = 2 + 1$ lattice study of radiative transitions in charmonium using technology pioneered by the Hadron Spectrum Collaboration have been presented. This is the first such dynamical study attempted in the charmonium spectrum. Distillation and a variational approach to optimising interpolating operators was used to create a large number of three point correlation functions with a range of souce and sink momenta. This allowed for the calculation of radiative form-factors $F(Q^2)$ at a wide range of Q^2 values. Fits to this data was used to find a value for $F(0)$ which provided a way to calculate physical decay rates that can be compared to experiment.

First the charge form-factors for the η_c, χ_{c0} and η_c' were presented. From fits to the form-factor data a value for the charge radius of these excitations was measured. The charge radius for the η_c was found to be 0.234(4) fm from the spatial current and 0.236(2) fm from the temporal current. These values lie in between the values of 0.255(2) fm found from a quenched analysis in reference [72] and 0.213(1) fm presented in reference [77] from a dynamical $N_f = 2$ study. The radius for the χ_{c0} was then found to be slightly larger at 0.34(3) fm for the spatial current and 0.30(2) for the temporal current. The values for the radius of the η_c' were found to be larger still at 0.49(13) for the spatial current and 0.45(7) for the temporal current. These larger radii are to be expected and can be explained as the χ_{c0} is a P wave state and the η_c' is an excitation of the ground state η_c.

Next results for two transitions in the charmonium spectrum were presented. First the partial decay width for the transitions $J/\psi \to \eta_c\gamma$ was found to be 2.66(4) keV and 1.01(1) keV using experimental and lattice masses respectively in Eqn. 6.3.2. This large discrepancy can be explained by the fact that the value for the hyperfine splitting, which the decay width is sensitive to, was found to be lower than its experimental value. A number of other studies resulted in comparable decay widths, as shown in Figure 6.8. Then the partial decay width for $\chi_{c0} \to J/\psi\gamma$ was found to be 212(3) keV and 251(3) keV using experimental and lattice masses respectively in Eqn. 6.3.7.

Finally some preliminary correlators were presented for the exotic hybrid state η_{c1}. This state is involved in the phenomenologically interesting transition $\eta_{c1} \to J/\psi\gamma$. The signal for this state was found to be short lived and it is proposed that for a

robust determination of this transition more time sources would be needed. This was employed in reference [25], where up to 128 timesources were used to extract robust energy levels for high lying and exotic states.

Chapter 7

Conclusions and Future Directions

This thesis began with an attempt to motivate why lattice quantum chromodynamics is necessary to move forward in the quest to understand the world at its most fundamental level. The Standard Model of particle physics encapsulates our theoretical understanding of the sub-atomic world and should continue to be tested via both experimental and theoretical studies. Unfortunately, the non-abelian nature of the strong interaction results in a large coupling at hadronic energy scales. This prohibits perturbative investigations and so one must turn to the lattice. This is especially important as many unexplained hadronic resonances have been observed in collider experiments and there is great interest in understanding their nature.

After a brief recap of continuum QCD, the need for regularisation when calculating path integrals in quantum field theory led to the introduction of a finite spacetime lattice on which the theory of QCD was discretised. It was discussed how one may write down a simple discretised action which reproduces the continuum action in the limit where the lattice spacing goes to zero. With this comes discretisation errors which are systematically improvable by a procedure known as Symanzik improvement. Then the technology necessary to extract mesonic energy levels on the lattice was introduced. Correlation functions between interpolators with appropriate quantum numbers contain all the requisite information however it is buried in a tower of other excited state energies. The variational method along

with distillation were introduced which provided a way to extract accurate energies for ground and excited states in the meson spectrum.

In Chapter 4 results of a dynamical $N_f = 2 + 1$ spectrum calculation for D_s and D mesons were shown, as presented in [1]. A correlation matrix between a large basis of interpolating operators was calculated using the distillation method and then diagonalised by solving a generalised eigenvalue problem. This allowed for the extraction of the highly excited energies in the spectrum and the use of appropriately chosen operators provided a way for the post hoc identification of each state's continuum spin. The states were found to lie in the traditional n^{2S+1} pattern with some exceptions, which were identified as potential hybrid states. The overall pattern of states was found to be qualitatively in line with that of similar earlier studies of the charm-light spectrum on lattices with heavier pion mass [48]. While not accounting for the unstable nature of the states above threshold, this study paves the way to extend earlier scattering studies in the charm-light sector performed at higher pion mass towards the physical point.

This was followed by a discussion on extracting radiative transition form-factors on the lattice. The ideas used in the calculation of the meson spectra were extended so as to access radiative transition matrix elements on the lattice which appear in the decomposition of three point correlation functions. To minimise contamination from higher excited states improved operators construced via solving the generalised eigenvalue problem were used. Finally results were shown from a recent study investigating radiative transitions between states in the charmonium spectrum. The individual form-factors for the η_c, χ_{c0} and η_c' were investigated. This allowed for an estimate of the charge radius of these mesons. The transitions $J/\psi \to \eta_c\gamma$ and $\chi_{c0} \to J/\psi\gamma$ were then measured, resulting in a value for the partial decay rates which can be compared to experimentally measured values. However these calculations are primarily exploratory and only account for errors which are statistical in nature. To make a more accurate comparison to experiment or provide valid predictions, a more conservative investigation of the associated systematic errors would need to be performed.

The work discussed in this thesis has laid the ground work needed to study radiative transitions involving higher excited states in the spectrum of charmonium. Of particular interest is the transition involving the exotic 1^{-+} state, $\eta_{c1} \to J/\psi\gamma$.

Previous studies of the charmonium spectrum have identified this state as a potential gluonic hybrid. A lattice calculation of this transition using up to date dynamical lattices and the technology discussed here would be the first of its kind. This would allow access to photocouplings of great interest to many experiment where the photo-production of these mesons is thought to be significant and so would be a timely endeavour.

Appendix A

Error Analysis

A.1 Jackknife Resampling

For a set of N uncorrelated measurements, $\{x_i\}$, of some observable on a set of Monte Carlo generated configurations one can define the standard mean and variance of the observable as

$$\langle x \rangle = \frac{1}{N} \sum_{i}^{N} x_i, \tag{A.1.1}$$

$$\sigma_x^2 = \frac{1}{N} \sum_{i}^{N} (x_i - \langle x \rangle)^2. \tag{A.1.2}$$

From this one can then quote a value for the observable with a one sigma uncertainty as $\langle x \rangle \pm \sigma_x$.

In order to make an improved estimate for the variance of the data one may use a process known as single elimination jackknife resampling. A new set of N data, $\{y_i\}$, is defined by forming N subsets of the original data via removing the i^{th} measurement,

$$y_i = \frac{1}{N-1} \sum_{j \neq i}^{N} x_j. \tag{A.1.3}$$

This new set of data $\{y_i\}$ has the same mean as the original data set as

$$\begin{aligned} y_i &= \frac{1}{N-1}\sum_j^N x_j - \frac{1}{N-1}x_i \\ &= \frac{1}{N-1}(N\langle x\rangle - x_i) \\ &= \langle x\rangle + \frac{1}{N-1}(\langle x\rangle - x_i). \end{aligned} \tag{A.1.4}$$

From this it is clear that

$$\langle y\rangle = \frac{1}{N}\sum_i^N y_i = \langle x\rangle. \tag{A.1.5}$$

The variance of the new jackknife data set is given as

$$\begin{aligned} \sigma_y^2 &= \frac{N-1}{N}\sum_i^N (y_i - \langle y\rangle)^2 \\ &= \frac{N-1}{N}\sum_i^N (\langle x\rangle + \frac{1}{N-1}(\langle x\rangle - x_i) - \langle y\rangle)^2 \\ &= \frac{N-1}{(N-1)^2}\frac{1}{N}\sum_i^N (\langle x\rangle - x_i)^2 \\ &= \frac{1}{N-1}\sigma_x^2. \end{aligned} \tag{A.1.6}$$

It is clear that the new estimate for the value of the observable $\langle y\rangle \pm \sigma_y$ has a reduced error compared to the original estimate.

The use of jackknife resampling also allows for the estimate of errors for various quatities which may not be just simple functions of the measured lattice data such as fits to the data, without the need for complicated formulae relating to propagation of errors. All errors quoted in this work are calculated from the appropriate jackknife data sets.

Appendix B

Tables of Results

B.1 D_s and D meson energies

In Tables B.1 and B.2 numerical values for D_s and D meson masses obtained for $M_\pi \sim 240$ MeV are presented. Masses are given in MeV with half the mass of the η_c subtracted in order to minimise the systematic uncertainty in tuning the charm quark mass. In all cases the quoted error corresponds to the (one-sigma) statistical uncertainty. As discussed earlier, above the lowest multi-hadron threshold in each channel states can decay strongly into lighter hadrons and, aside from any other systematic uncertainties, the masses are only expected to be correct up to around the width of the state [24].

J^P	$M - M_{\eta_c}/2\ (MeV)$					
0^-	467(11)	1225(17)	1679(27)	1873(31)		
1^-	593(12)	1286(12)	1399(21)	1740(30)	1891(33)	1898(38)
2^-	1424(19)	1440(20)	1952(35)	1993(36)	2002(32)	
3^-	1481(19)	2029(28)				
4^-	2075(29)	2109(31)				
0^+	886(14)	1567(35)	1934(51)			
1^+	1022(15)	1064(16)	1612(25)	1670(26)	1929(44)	2030(35)
2^+	1100(15)	1675(24)	1773(23)	2000(37)		
3^+	1766(22)	1779(22)				
4^+	1811(24)					

TABLE B.1: Summary of the D_s meson spectrum presented in Figure 4.3. Masses are shown with $M_{\eta_c}/2$ subtracted. Quoted uncertainties are statistical only. Reproduced from [1].

J^P	$M - M_{\eta_c}/2\ (MeV)$					
0^-	382(10)	1138(17)	1569(26)	1783(29)	2176(37)	
1^-	509(11)	1233(22)	1315(21)	1610(33)	1801(34)	1838(36)
2^-	1352(19)	1429(20)	1912(34)	1935(34)		
3^-	1441(19)	2032(26)				
4^-	2037(29)					
0^+	770(15)	1494(25)	2201(45)	1874(26)		
1^+	881(17)	984(14)	1559(27)	1603(26)		
2^+	1020(16)	1623(26)	1665(29)	1925(36)		
3^+	1724(21)	1743(21)				
4^+	1804(22)					

TABLE B.2: Summary of the D meson spectrum presented in Figure 4.5. Masses are shown with $M_{\eta_c}/2$ subtracted. Quoted uncertainties are statistical only. Reproduced from [1].

B.2 Form-Factor Values

The following tables show the values used in the form factor fits shown in Chapter 6.

η_c	Q^2	$FF(Q^2)$	$\delta FF(Q^2)$
temporal	0.26027	0.94811	0.00043
	1.04858	0.81391	0.00062
	0.52429	0.90096	0.00059
	0.78456	0.85553	0.00060
	0.76960	0.85746	0.00062
temporal	0.26027	0.93911	0.00043
improved	1.04858	0.78377	0.00059
	0.52429	0.88360	0.00057
	0.78456	0.83132	0.00056
	0.76960	0.83414	0.00064
spatial	0.26023	0.94092	0.00186
	0.51671	0.87680	0.00126
	0.76960	0.81949	0.00104
	0.26027	0.94085	0.00119
	1.04858	0.79129	0.00111
	0.52429	0.89119	0.00125
	0.51671	0.87755	0.00250
	0.51689	0.87916	0.00097
	0.26032	0.93808	0.00079
	1.04858	0.78942	0.00123
	0.78456	0.83702	0.00106
	0.78456	0.83775	0.00119
	0.76960	0.82182	0.00236
spatial	0.26023	0.94871	0.00186
improved	0.51671	0.89137	0.00125
	0.76960	0.83998	0.00105
	0.26027	0.94473	0.00120
	1.04858	0.79129	0.00111
	0.52429	0.89119	0.00125
	0.51671	0.89223	0.00255
	0.51689	0.88878	0.00098
	0.26032	0.94098	0.00150
	1.04858	0.78942	0.00123
	0.78456	0.83929	0.00106
	0.78456	0.84003	0.00119
	0.76960	0.84242	0.00243

TABLE B.3: Summary of the η_c form-factor values.

χ_{c0}	Q^2	$FF(Q^2)$	$\delta FF(Q^2)$
temporal	0.26041	0.91445	0.01729
improved	1.02682	0.67103	0.01864
	0.51804	0.82936	0.01700
	0.26074	0.89821	0.02151
	0.52429	0.82898	0.01888
	0.51819	0.82801	0.02587
	0.26049	0.89506	0.02573
	1.04858	0.67237	0.02373
	0.78503	0.74192	0.01771
	0.78503	0.74158	0.01820
	0.78566	0.73788	0.02951
	0.0	1.00719	0.02269
	0.0	1.03123	0.03305

χ_{c0}	Q^2	$FF(Q^2)$	$\delta FF(Q^2)$
spatial	0.25093	0.87357	0.02793
improved	0.26074	0.91750	0.03687
	1.04858	0.62205	0.03814
	0.52429	0.79816	0.04413
	0.51804	0.78749	0.02971
	1.04858	0.61407	0.03956
	0.78503	0.67869	0.04402
	0.78503	0.68786	0.03992
	0.0	1.01415	0.02697
	0.0	1.02668	0.02672

TABLE B.4: Summary of the χ_{c0} form-factor values.

η_c'	Q^2	$FF(Q^2)$	$\delta FF(Q^2)$
temporal	1.02567	0.41278	0.06873
improved	0.26097	0.65881	0.09376
	0.52429	0.59724	0.07620
	0.51861	0.58948	0.09369
	0.78525	0.51092	0.07882
	0.78525	0.49110	0.07718
	0.0	0.88288	0.09606
	0.0	0.86040	0.12300

η_c'	Q^2	$FF(Q^2)$	$\delta FF(Q^2)$
spatial	0.26067	0.50162	0.16725
improved	1.02567	0.29951	0.08759
	0.77350	0.47738	0.12629
	0.24938	0.65872	0.14058
	1.04858	0.35157	0.14396
	0.52429	0.39550	0.14477
	0.51861	0.54748	0.14132
	1.04858	0.30520	0.15669
	0.78525	0.50881	0.15739
	0.77350	0.43294	0.11223
	0.0	0.87273	0.12979
	0.0	0.86345	0.14199

TABLE B.5: Summary of the η_c' form-factor values.

$J/\psi \to \eta_c$	Q^2	$FF(Q^2)$	$\delta FF(Q^2)$
	0.26082	1.91582	0.00522
	0.52423	1.80113	0.00447
	0.78392	1.69439	0.00393
	0.26082	1.91889	0.00437
	0.52423	1.80503	0.00335
	0.78392	1.69524	0.00398
	0.49692	1.81043	0.00518
	0.74361	1.70883	0.00549
	0.49692	1.80992	0.00580
	0.74361	1.70638	0.00631

$\chi_{c0} \to J/\psi$	Q^2	$FF(Q^2)$	$\delta FF(Q^2)$
	-0.14699	0.12451	0.00157
	-0.14699	0.12404	0.00150
	0.08207	0.14886	0.00205
	0.08207	0.14596	0.00205
	0.76617	0.18952	0.00335
	0.76617	0.18562	0.00431
	0.30893	0.16559	0.00238
	0.30893	0.16585	0.00238
	-0.14595	0.12585	0.00177
	-0.14595	0.12280	0.00186
	-0.14374	0.12869	0.00213
	-0.14374	0.12515	0.00229

TABLE B.6: Summary of the $J/\psi \to \eta_c$ and $\chi_{c0} \to J/\psi$ transitionform-factor values.

Bibliography

[1] Gavin K. C. Cheung, Cian O'Hara, Graham Moir, Michael Peardon, Sinéad M. Ryan, Christopher E. Thomas, and David Tims. Excited and exotic charmonium, D_s and D meson spectra for two light quark masses from lattice QCD. *JHEP*, 12:089, 2016. doi: 10.1007/JHEP12(2016)089.

[2] F. Abe et al. Observation of top quark production in $\bar{p}p$ collisions. *Phys. Rev. Lett.*, 74:2626–2631, 1995. doi: 10.1103/PhysRevLett.74.2626.

[3] S. Abachi et al. Observation of the top quark. *Phys. Rev. Lett.*, 74:2632–2637, 1995. doi: 10.1103/PhysRevLett.74.2632.

[4] Issac. Newton. PhilosophiæNaturalis Principia Mathematica. 1687.

[5] Albert. Einstein. Zur allgemeinen Relativitätstheorie. 1915.

[6] S. L. Glashow. Partial Symmetries of Weak Interactions. *Nucl. Phys.*, 22: 579–588, 1961. doi: 10.1016/0029-5582(61)90469-2.

[7] Steven Weinberg. A model of leptons. *Phys. Rev. Lett.*, 19:1264–1266, Nov 1967. doi: 10.1103/PhysRevLett.19.1264. URL https://link.aps.org/doi/10.1103/PhysRevLett.19.1264.

[8] Abdus Salam. Weak and Electromagnetic Interactions. *Conf. Proc.*, C680519: 367–377, 1968.

[9] Ahmed Ali, Jens Sören Lange, and Sheldon Stone. Exotics: Heavy Pentaquarks and Tetraquarks. *Prog. Part. Nucl. Phys.*, 97:123–198, 2017. doi: 10.1016/j.ppnp.2017.08.003.

[10] Tatsumi Aoyama, Katsuyuki Asano, Masashi Hayakawa, Toichiro Kinoshita, Makiko Nio, and Noriaki Watanabe. Tenth-order lepton $g-2$: Contribution

from diagrams containing sixth-order light-by-light-scattering subdiagram internally. *Phys. Rev. D*, 81:053009, Mar 2010. doi: 10.1103/PhysRevD.81.053009. URL https://link.aps.org/doi/10.1103/PhysRevD.81.053009.

[11] Kenneth G. Wilson. Confinement of quarks. *Phys. Rev. D*, 10:2445–2459, Oct 1974. doi: 10.1103/PhysRevD.10.2445.

[12] J. J. Aubert et al. Experimental Observation of a Heavy Particle J. *Phys. Rev. Lett.*, 33:1404–1406, 1974. doi: 10.1103/PhysRevLett.33.1404.

[13] J. E. Augustin et al. Discovery of a Narrow Resonance in e^+e^- Annihilation. *Phys. Rev. Lett.*, 33:1406–1408, 1974. doi: 10.1103/PhysRevLett.33.1406. [Adv. Exp. Phys.5,141(1976)].

[14] N. Brambilla et al. Heavy quarkonium: progress, puzzles, and opportunities. *Eur. Phys. J.*, C71:1534, 2011. doi: 10.1140/epjc/s10052-010-1534-9.

[15] Atsushi Hosaka, Toru Iijima, Kenkichi Miyabayashi, Yoshihide Sakai, and Shigehiro Yasui. Exotic hadrons with heavy flavors: X, Y, Z, and related states. *PTEP*, 2016(6):062C01, 2016. doi: 10.1093/ptep/ptw045.

[16] Eric S. Swanson. XYZ States: Theory Overview. *AIP Conf. Proc.*, 1735: 020013, 2016. doi: 10.1063/1.4949381.

[17] Elisabetta Prencipe. Hadrons with c-s content: past, present and future. In *Proceedings, 53rd International Winter Meeting on Nuclear Physics (Bormio 2015): Bormio, Italy, January 26-30, 2015*, 2015. URL https://inspirehep.net/record/1397172/files/arXiv:1510.03053.pdf.

[18] S. Durr, Z. Fodor, C. Hoelbling, S. D. Katz, S. Krieg, T. Kurth, L. Lellouch, T. Lippert, K. K. Szabo, and G. Vulvert. Lattice QCD at the physical point: light quark masses. *Phys. Lett.*, B701:265–268, 2011. doi: 10.1016/j.physletb.2011.05.053.

[19] J. Koponen, F. Bursa, C. T. H. Davies, R. J. Dowdall, and G. P. Lepage. Size of the pion from full lattice QCD with physical u , d , s and c quarks. *Phys. Rev.*, D93(5):054503, 2016. doi: 10.1103/PhysRevD.93.054503.

[20] Chuan Liu. Review on Hadron Spectroscopy. *PoS*, LATTICE2016:006, 2017. doi: 10.22323/1.256.0006.

[21] Zoltan Fodor and Christian Hoelbling. Light hadron masses from lattice qcd. *Rev. Mod. Phys.*, 84:449–495, Apr 2012. doi: 10.1103/RevModPhys.84.449. URL https://link.aps.org/doi/10.1103/RevModPhys.84.449.

[22] Jozef J. Dudek, Robert G. Edwards, Nilmani Mathur, and David G. Richards. Charmonium excited state spectrum in lattice QCD. *Phys. Rev.*, D77:034501, 2008. doi: 10.1103/PhysRevD.77.034501.

[23] Jozef J. Dudek, Robert G. Edwards, Michael J. Peardon, David G. Richards, and Christopher E. Thomas. Highly excited and exotic meson spectrum from dynamical lattice QCD. *Phys. Rev. Lett.*, 103:262001, 2009. doi: 10.1103/PhysRevLett.103.262001.

[24] Jozef J. Dudek, Robert G. Edwards, Michael J. Peardon, David G. Richards, and Christopher E. Thomas. Toward the excited meson spectrum of dynamical QCD. *Phys. Rev.*, D82:034508, 2010. doi: 10.1103/PhysRevD.82.034508.

[25] L. Liu et al. Excited and exotic charmonium spectroscopy from lattice QCD. *JHEP*, 07:126, 2012. doi: 10.1007/JHEP07(2012)126.

[26] F. Knechtli, M. Günther, and M. Peardon. Lattice Quantum Chromodynamics: Practical Essentials. *Springer*, 2017. doi: 10.1007/978-94-024-0999-4.

[27] T. Umeda et al. Two flavors of dynamical quarks on anisotropic lattices. *Phys. Rev.*, D68:034503, 2003. doi: 10.1103/PhysRevD.68.034503.

[28] Robert G. Edwards, Balint Joó, and Huey-Wen Lin. Tuning for Three-flavors of Anisotropic Clover Fermions with Stout-link Smearing. *Phys. Rev.*, D78: 054501, 2008. doi: 10.1103/PhysRevD.78.054501.

[29] N. Metropolis, A. W. Rosenbluth, M. N. Rosenbluth, A. H. Teller, and E. Teller. Equation of State Calculations by Fast Computing Machines. *Journal of Chemical Physics*, 21:1087–1092, 1953. doi: 10.1063/1.1699114.

[30] M. A. Clark. The Rational Hybrid Monte Carlo Algorithm. *PoS*, LAT2006: 004, 2006.

[31] A. D. Kennedy. Algorithms for dynamical fermions. 2006.

[32] Christof Gattringer and Christian B. Lang. Quantum chromodynamics on the lattice. *Lect. Notes Phys.*, 788:1–343, 2010. doi: 10.1007/978-3-642-01850-3.

[33] H.B. Nielsen and M. Ninomiya. A no-go theorem for regularizing chiral fermions. *Physics Letters B*, 105(2):219 – 223, 1981. ISSN 0370-2693. doi: https://doi.org/10.1016/0370-2693(81)91026-1. URL http://www.sciencedirect.com/science/article/pii/0370269381910261.

[34] John Kogut and Leonard Susskind. Hamiltonian formulation of wilson's lattice gauge theories. *Phys. Rev. D*, 11:395–408, Jan 1975. doi: 10.1103/PhysRevD.11.395. URL https://link.aps.org/doi/10.1103/PhysRevD.11.395.

[35] S. Sint. Lattice qcd with a chiral twist. *Perspectives in Lattice QCD, Proceedings of the Workshop in Nara, Japan*, 2005.

[36] G. Curci, P. Menotti, and G. Paffuti. Symanzik's Improved Lagrangian for Lattice Gauge Theory. *Phys. Lett.*, 130B:205, 1983. doi: 10.1016/0370-2693(83)91043-2. [Erratum: Phys. Lett.135B,516(1984)].

[37] M. Luscher and P. Weisz. On-Shell Improved Lattice Gauge Theories. *Commun. Math. Phys.*, 97:59, 1985. doi: 10.1007/BF01206178. [Erratum: Commun. Math. Phys.98,433(1985)].

[38] G. Peter Lepage and Paul B. Mackenzie. On the viability of lattice perturbation theory. *Phys. Rev.*, D48:2250–2264, 1993. doi: 10.1103/PhysRevD.48.2250.

[39] B. Sheikholeslami and R. Wohlert. Improved Continuum Limit Lattice Action for QCD with Wilson Fermions. *Nucl. Phys.*, B259:572, 1985. doi: 10.1016/0550-3213(85)90002-1.

[40] M. Albanese et al. Glueball Masses and String Tension in Lattice QCD. *Phys. Lett.*, B192:163–169, 1987. doi: 10.1016/0370-2693(87)91160-9.

[41] Anna Hasenfratz and Francesco Knechtli. Flavor symmetry and the static potential with hypercubic blocking. *Phys. Rev. D*, 64:034504, Jul 2001. doi: 10.1103/PhysRevD.64.034504. URL https://link.aps.org/doi/10.1103/PhysRevD.64.034504.

[42] Colin Morningstar and Mike J. Peardon. Analytic smearing of SU(3) link variables in lattice QCD. *Phys. Rev.*, D69:054501, 2004. doi: 10.1103/PhysRevD.69.054501.

[43] Huey-Wen Lin et al. First results from 2+1 dynamical quark flavors on an anisotropic lattice: Light-hadron spectroscopy and setting the strange-quark mass. *Phys. Rev.*, D79:034502, 2009. doi: 10.1103/PhysRevD.79.034502.

[44] R.J. Dowdall, C.T.H. Davies, T.C. Hammant, and R.R. Horgan. Precise heavy-light meson masses and hyperfine splittings from lattice QCD including charm quarks in the sea. *Phys.Rev.*, D86:094510, 2012. doi: 10.1103/PhysRevD.86.094510.

[45] Y. Namekawa et al. Charm quark system at the physical point of 2+1 flavor lattice QCD. *Phys.Rev.*, D84:074505, 2011. doi: 10.1103/PhysRevD.84.074505.

[46] S. Aoki et al. Review of lattice results concerning low-energy particle physics. *Eur. Phys. J.*, C77(2):112, 2017. doi: 10.1140/epjc/s10052-016-4509-7.

[47] G. Bali et al. Spectra of heavy-light and heavy-heavy mesons containing charm quarks, including higher spin states for $N_f = 2 + 1$. *PoS*, LATTICE2011:135, 2011.

[48] Graham Moir, Michael Peardon, Sinead M. Ryan, Christopher E. Thomas, and Liuming Liu. Excited spectroscopy of charmed mesons from lattice QCD. *JHEP*, 05:021, 2013. doi: 10.1007/JHEP05(2013)021.

[49] Martin Kalinowski and Marc Wagner. Masses of D mesons, D_s mesons and charmonium states from twisted mass lattice QCD. *Phys. Rev.*, D92(9): 094508, 2015. doi: 10.1103/PhysRevD.92.094508.

[50] Michael Peardon et al. A novel quark-field creation operator construction for hadronic physics in lattice QCD. *Phys. Rev.*, D80:054506, 2009. doi: 10.1103/PhysRevD.80.054506.

[51] Christopher Michael. Adjoint Sources in Lattice Gauge Theory. *Nucl. Phys.*, B259:58, 1985. doi: 10.1016/0550-3213(85)90297-4.

[52] Martin Lüscher and Ulli Wolff. How to calculate the elastic scattering matrix in two- dimensional quantum field theories by numerical simulation. *Nucl. Phys.*, B339:222–252, 1990. doi: 10.1016/0550-3213(90)90540-T.

[53] J. Aubert et al. Observation of a narrow meson decaying to $D_s^+\pi^0$ at a mass of 2.32 GeV/c^2. *Phys. Rev. Lett.*, 90:242001, 2003.

[54] D. Besson et al. Observation of a Narrow Resonance of Mass 2.46 GeV/c^2 Decaying to $D_s^* + \pi^0$ and Confirmation of the $D_s^*(2317)$ State. *Phys. Rev.*, D68:032002, 2003.

[55] Feng-Kun Guo and Ulf-G. Meissner. Light quark mass dependence in heavy quarkonium physics. *Phys. Rev. Lett.*, 109:062001, 2012. doi: 10.1103/PhysRevLett.109.062001.

[56] Daniel Mohler and R. M. Woloshyn. D and D_s meson spectroscopy. *Phys. Rev.*, D84:054505, 2011. doi: 10.1103/PhysRevD.84.054505.

[57] Gunnar Bali, Sara Collins, and Paula Perez-Rubio. Charmed hadron spectroscopy on the lattice for $N_f = 2 + 1$ flavours. *J. Phys. Conf. Ser.*, 426: 012017, 2013. doi: 10.1088/1742-6596/426/1/012017.

[58] Krzysztof Cichy, Martin Kalinowski, and Marc Wagner. The continuum limit of the D meson, D_s meson and charmonium spectrum from $N_f = 2 + 1 + 1$ twisted mass lattice QCD. 2016.

[59] Graham Moir, Michael Peardon, Sinéad M. Ryan, Christopher E. Thomas, and David J. Wilson. Coupled-Channel $D\pi$, $D\eta$ and $D_s\bar{K}$ Scattering from Lattice QCD. *JHEP*, 10:011, 2016. doi: 10.1007/JHEP10(2016)011.

[60] Daniel Mohler, Sasa Prelovsek, and R. M. Woloshyn. $D\pi$ scattering and D meson resonances from lattice QCD. *Phys. Rev.*, D87(3):034501, 2013. doi: 10.1103/PhysRevD.87.034501.

[61] Daniel Mohler, C. B. Lang, Luka Leskovec, Sasa Prelovsek, and R. M. Woloshyn. $D_{s0}^*(2317)$ Meson and D-Meson-Kaon Scattering from Lattice QCD. *Phys. Rev. Lett.*, 111(22):222001, 2013. doi: 10.1103/PhysRevLett.111.222001.

[62] David J. Wilson, Raul A. Briceño, Jozef J. Dudek, Robert G. Edwards, and Christopher E. Thomas. Coupled $\pi\pi, K\bar{K}$ scattering in P-wave and the ρ resonance from lattice QCD. *Phys. Rev.*, D92(9):094502, 2015. doi: 10.1103/PhysRevD.92.094502.

[63] M. Tanabashi *et al.* Review of Particle Physics. *Phys. Rev. D*, 98:030001, 2018.

[64] Jozef J. Dudek, Robert G. Edwards, and Christopher E. Thomas. Energy dependence of the ρ resonance in $\pi\pi$ elastic scattering from lattice QCD. *Phys. Rev.*, D87(3):034505, 2013. doi: 10.1103/PhysRevD.87.034505,10.1103/PhysRevD.90.099902. [Erratum: Phys. Rev.D90,no.9,099902(2014)].

[65] K. A. Olive et al. Review of Particle Physics. *Chin. Phys.*, C38:090001 and 2015 update, 2014. doi: 10.1088/1674-1137/38/9/090001.

[66] F. E. Close and E. S. Swanson. Dynamics and decay of heavy-light hadrons. *Phys. Rev.*, D72:094004, 2005. doi: 10.1103/PhysRevD.72.094004.

[67] Jozef J. Dudek. The lightest hybrid meson supermultiplet in QCD. *Phys. Rev.*, D84:074023, 2011. doi: 10.1103/PhysRevD.84.074023.

[68] Jozef J. Dudek, Robert G. Edwards, Peng Guo, and Christopher E. Thomas. Toward the excited isoscalar meson spectrum from lattice QCD. *Phys. Rev.*, D88(9):094505, 2013. doi: 10.1103/PhysRevD.88.094505.

[69] Michal Broz. Charmonium photoproduction in ultra-peripheral p-Pb and Pb-Pb collisions at the LHC with the ALICE experiment. In *Proceedings, 2nd Conference on Large Hadron Collider Physics Conference (LHCP 2014): New York, USA, June 2-7, 2014*, 2014. URL https://inspirehep.net/record/1318482/files/arXiv:1409.6169.pdf.

[70] Christian J. Shultz, Jozef J. Dudek, and Robert G. Edwards. Excited meson radiative transitions from lattice QCD using variationally optimized operators. *Phys. Rev.*, D91(11):114501, 2015. doi: 10.1103/PhysRevD.91.114501.

[71] Cian O'Hara, Sinéad M. Ryan, Graham Moir, and Christopher E. Thomas. Towards Radiative Transitions in Charmonium. *PoS*, Lattice2016:120, 2016.

[72] Jozef J. Dudek, Robert G. Edwards, and David G. Richards. Radiative transitions in charmonium from lattice QCD. *Phys. Rev.*, D73:074507, 2006. doi: 10.1103/PhysRevD.73.074507.

[73] Jozef J. Dudek, Robert Edwards, and Christopher E. Thomas. Exotic and excited-state radiative transitions in charmonium from lattice QCD. *Phys. Rev.*, D79:094504, 2009. doi: 10.1103/PhysRevD.79.094504.

[74] Christopher E. Thomas, Robert G. Edwards, and Jozef J. Dudek. Helicity operators for mesons in flight on the lattice. *Phys.Rev.*, D85:014507, 2012. doi: 10.1103/PhysRevD.85.014507,10.1103/PhysRevD.85.039901.

[75] R. E. Mitchell *et al.* J/ψ and $\psi(2s)$ radiative transitions to η_c. *Phys. Rev. Lett.*, 102:011801, Jan 2009. doi: 10.1103/PhysRevLett.102.011801. URL https://link.aps.org/doi/10.1103/PhysRevLett.102.011801.

[76] V. V. Anashin et al. Measurement of $J/\psi \to \gamma\eta_c$ decay rate and η_c parameters at KEDR. *Phys. Lett.*, B738:391–396, 2014. doi: 10.1016/j.physletb.2014.09.064.

[77] Ying Chen et al. Radiative transitions in charmonium from $N_f = 2$ twisted mass lattice QCD. *Phys. Rev.*, D84:034503, 2011. doi: 10.1103/PhysRevD.84.034503.

[78] Damir Becirevic and Francesco Sanfilippo. Lattice QCD study of the radiative decays $J/\psi \to \eta_c\gamma$ and $h_c \to \eta_c\gamma$. *JHEP*, 01:028, 2013. doi: 10.1007/JHEP01(2013)028.

[79] G. C. Donald, C. T. H. Davies, R. J. Dowdall, E. Follana, K. Hornbostel, J. Koponen, G. P. Lepage, and C. McNeile. Precision tests of the J/ψ from full lattice QCD: mass, leptonic width and radiative decay rate to η_c. *Phys. Rev.*, D86:094501, 2012. doi: 10.1103/PhysRevD.86.094501.

[80] D. M. Asner et al. Physics at BES-III. *Int. J. Mod. Phys.*, A24:S1–794, 2009.

[81] L. Levkova and C. DeTar. Charm annihilation effects on the hyperfine splitting in charmonium. *Phys. Rev.*, D83:074504, 2011. doi: 10.1103/PhysRevD.83.074504.